UNIVERSITÀ DEGLI STUDI DI PADOVA

Dipartimento di Fisica e Astronomia "Galileo Galilei"

Master Degree in Astrophysics and Cosmology

Master Thesis

DYNAMICAL MODELLING OF THE COUNTERROTATING STELLAR COMPONENTS IN THE S0 GALAXY NGC 1366

Supervisor

Prof. Enrico Maria Corsini

Co-Supervisors

Prof. Luca Ciotti

Dr. Leonardo De Deo

Student

Mattia Merola

Academic Year 2023/2024

Abstract

In this work we study the highly-inclined S0 galaxy NGC 1366 in the Fornax cluster, which is known to host a stellar component that is kinematically decoupled from the main body of the galaxy. According to a parametric spectroscopic decomposition of the spectrum obtained along the galaxy major axis, the counter-rotating stellar component is younger, has nearly the same metallicity, and has a lower α-element overabundance than the co-rotating component. We build a two-integrals exploratory dynamical models of NGC 1366 using an original code dedicated to the solution of the Jeans equations for axisymmetric multicomponent systems, and allowing for an easy treatment of counter-rotation. The models include only a Sérsic bulge and a Freeman disk and use constant Satoh parameters. We consider a non-rotating galaxy model, a non-rotating bulge model, as well as the case of maximally, mildly, and moderately counter-rotating models. Our results show that each counter-rotating model only partially reproduces the observed kinematics. We expect to improve the modelling by adding a DM halo and considering a space-dependent Satoh parameter. NGC 1366 can serve as a case study to be applied to other counter-rotating galaxies for understanding their structure and constraining their formation mechanisms.

Contents

List of Figures

List of Tables

Chapter 1

Introduction

In this chapter we introduce and explain the phenomenon of counter-rotation. In Section 1.1 we explore the different types of counter-rotation. In Section 1.2 we focus on the tools used to detect counter-rotation. In Section 1.3 we examine the environment and morphological features of counter-rotating galaxies. In Section 1.4 we present the statistical data on counter-rotating galaxies. In Section 1.5 we examine the different scenarios that could explain their formation. Finally, in Section 1.6 we discuss the different stellar populations found in counter-rotating components.

1.1 The counter-rotation phenomenon

Counter-rotating galaxies are characterized by the presence of two components that are observed to rotate in opposite directions one with respect to the other. These galaxies were initially predicted theoretically, but their astrophysical significance was not recognized until the kinematics of the ionized gas and stellar components of the SB0 galaxy NGC 4564 was measured. The gas was found to have velocity similar in magnitude but opposite in direction to that of the stars (Galletta 1987). The detection of counter-rotation in elliptical galaxies dates back to the same period, with the observation of NGC 5898 by Bertola & Bettoni (1988). However, the word "counter-rotation", which remains in use today, was first introduced by Franx & Illingworth (1988), who detected a massive and rapidly counter-rotating stellar core in the radio elliptical galaxy IC 1459. Since then, what was once considered a rare phenomenon has been found to be quite common across dozens of galaxies along all the Hubble sequence, from ellipticals to irregulars.

Previous reviews about counter-rotation were written by Rubin (1994b), Galletta (1996), and Bertola & Corsini (1999). A more recent overview of the topic is offered by Corsini (2014).

Counter-rotation in galaxies can be classified based on the nature of the rotational motion of their components. In particular, we talk about:

- *intrinsic counter-rotation* if two kinematically decoupled components rotate in opposite directions, with their rotation axes aligned. This means that their angular momentum vectors are antiparallel;
- *apparent counter-rotation* if the two kinematically decoupled components rotate around skewed, non-aligned axes and the line of sight (LOS) lies in between them. This means that the projections of their angular momentum vectors onto the sky plane are antiparallel.

Observationally, the intrinsic or apparent nature of counter-rotation may be addressed in not edge-on galaxies by analyzing their full velocity field as mapped with multi-slit or integral-field

spectroscopy.

We can identify various types of counter-rotation, depending on the specific components involved:

1. *gas-versus-gas counter-rotation*: this occurs when two gaseous disks rotate in opposite directions. A notable example is the S0 galaxy NGC 7332, where two ionized-gas disks counter-rotate. The gas is distributed asymmetrically and displays non-circular motions, indicating that it has not reached equilibrium; these observations strongly support the occurrence of an accretion process in this galaxy (Fisher et al. 1994);

2. *gas-versus-stars counter-rotation* (or *gaseous counter-rotation*): this occurs when the gaseous disk counter-rotates with respect to the stellar body of the galaxy. An example is the SB0/SBa galaxy NGC 4546, where the ionized, molecular, and atomic gas rotate at a similar speed, but with opposite direction with respect to the stars (Galletta 1987; Bettoni et al. 1991; Sage & Galletta 1994);

3. *stars-versus-stars counter-rotation* (or *stellar counter-rotation*): this occurs when two stellar components counter-rotate. Usually, the more massive component is considered as the reference (prograde) one. There can be many types of stellar counter-rotating components: two stellar disks (e.g. NGC 4550; Rubin et al. 1992; Johnston et al. 2013 among others, and NGC 1366; Morelli et al. 2008, 2017), the bulge (e.g. NGC 524; Katkov et al. 2011a), a secondary bar (e.g NGC 2950; Corsini et al. 2003; Katkov et al. 2011b), or even a portion of a bar (e.g. Bettoni 1989; Bettoni & Galletta 1997).

Furthermore, counter-rotation in disk galaxies can be observed in:

- the *inner regions* of the galaxy. An example is the Sa galaxy NGC 3593, which consists of a small bulge, a primary stellar disk containing about 80% of the stars, and a secondary less massive counter-rotating stellar disk, which is the result of an external gas acquisition (Bertola et al. 1996). This secondary disk is younger and dominates the kinematics within the inner 500 pc and corotates with the disk of ionized and molecular gas (Corsini et al. 1998; Pizzella et al. 1999; Coccato et al. 2013).

- the *outer regions* of the galaxy. For instance, the Sab galaxy NGC 4826 (M64) contains two counter-rotating nested, almost coplanar disks of ionized, molecular and neutral gas extending out $\sim$1 and $\sim$11 kpc, respectively. The inner disk contains stars and gas that orbit in a single direction, whereas in the narrow transition region and beyond, stars continue to orbit prograde, but the gas velocities reverse from prograde to retrograde (Braun et al. 1992; Braun et al. 1994; Walterbos et al. 1994; Rubin 1994a).

- *overall the galaxy.* For example, the Sa galaxy NGC 3626 was the first spiral galaxy where the gaseous component was observed to counter-rotate at all radii with respect to the stars (Ciri et al. 1995; García-Burillo et al. 1998; Haynes et al. 2000; Sil'chenko et al. 2010).

1.2 Detection of counter-rotation

Detecting gas-versus-stars counter-rotation is relatively straightforward from an observational standpoint, since the spectral lines of interest are different for the two components. In particular, while for the ionized gas we refer to emission lines such as [N II] ($\lambda\lambda$6583 Å), Hα ($\lambda\lambda$6563 Å) and [S II] ($\lambda\lambda$6716, 6731 Å), for the stellar components we study absorption lines as Hβ ($\lambda\lambda$4861 Å) and the Mg triplet ($\lambda\lambda$5164, 5173, 5184 Å) (Pizzella et al. 2004). Counter-rotation

may be addressed by looking at the opposite orientation of the ionized gas emission lines and stellar absorption lines in 2D optical spectra (see for example Figure 1 in Galletta 1987), or in position-velocity diagrams (see for example Figure 1 in Bureau & Chung 2006). These standard techniques allow us to measure differences in the rotational velocities of few km s^{-1} in the gaseous and stellar kinematics.

On the other hand, the detection of a stars-versus-stars counter-rotation is much more difficult, because the diagnosis is based on the same absorption lines. X-shaped appearance of the absorption lines arises from the prograde and retrograde stellar disks (Figure 1.1a). However, this feature is only observed when the two components are photometrically similar to each other. Another possible signature for the presence of such a pattern can be a bimodal line-of-sight velocity distribution (LOSVD), with each peak representing one of the counter-rotating components (Figure 1.1b). However, its detection depends on many variables, including the galaxy properties and instrumentation setup of the spectroscopic observations. Counter-rotating stellar disks are most easily detected in the outer regions of galaxies, where the effects of seeing, bulge, and bar contamination are minimal. In these areas, the velocity separation between the counter-rotating components is maximal. Usually, the LOSVD is parametrized with the Gauss-Hermite series (Gerhard 1993; van der Marel & Franx 1993). Anyway, the LOSVD is poorly reproduced by this expansion when the galaxy hosts a secondary kinematic component (Fabricius et al. 2012; Katkov et al. 2013), as in the case of strong counter-rotation. However, the use of Gauss-Hermite parametric solutions provides a practical approach to detecting large counter-rotating stellar disks. This method can also help identify faint counter-rotating components, thereby improving the statistics of stellar counter-rotation. In addition, noise and aliasing features in the LOSVD can mimic what could be interpreted as a counter-rotating component (Rubino et al. 2021). Therefore, the recovery and decomposition of parametric LOSVDs must be performed with caution. Another significant indicator of the presence of a counter-rotating component is the presence of two off-center, symmetric peaks in the stellar velocity dispersion, commonly known as the "2σ feature" (Krajnović et al. 2011). The combination of the 2σ feature and zero velocity rotation along the galaxy major axis is a strong indicator of counter-rotation. These kinematic features typically occur within the radial range where the two counter-rotating components have the same luminosity and their LOSVDs are unresolved (see Figure 2.4 and its discussion). When the 2σ peak is difficult to detect due to the low signal-to-noise (S/N) ratio of the data, the large-scale pattern in the map of the third Gauss-Hermite coefficient h_3 can be used as a diagnostic for strong and weak counter-rotation (Rubino et al. 2021; Figure 1.1c). However, this analysis focused solely on pure disk structures, suggesting that the large-scale feature observed in the h_3 map could be misleading if other structural components are present. In certain notable cases of counter-rotating disk galaxies, the central and outer regions of a galaxy rotate in opposite directions, creating an S-shaped rotation curve along the major axis (Bertola et al. 1996; Gasymov & Katkov 2022). However, we usually consider the 2σ feature to be the most important kinematic diagnostic for counter-rotating galaxies, since it also appears for galaxy models with a regular rotation and no evidence for velocity decay or reversal (Rubino et al. 2021). Figure 1.1 illustrates some of these observational characteristics that are used to identify the presence of a counter-rotating component.

Spectroscopic decomposition alone is not sufficient to fully disentangle a counter-rotating galaxy. Complete kinematic decoupling requires both spectroscopic and photometric decomposition. From the surface-brightness radial profile of the galaxy we can assess the weight of each counter-rotating component in the spectra. By using different stellar templates (e.g. Thomas et al. 2003; Maraston 2005), characterized by different values of age, metallicity and enhancement of α elements, weighted by the surface brightness of the components, we can reproduce the observed spectrum and recover both the kinematic and stellar properties of the

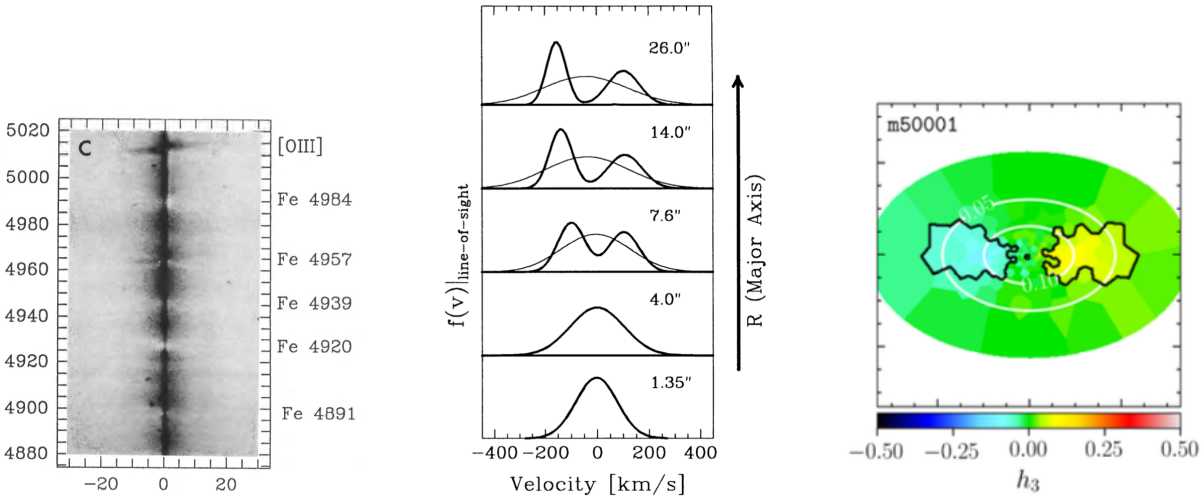

(a) X-shaped absorption lines. (b) Bimodal LOSVD. (c) h_3 large-scale pattern.

Figure 1.1: These figures report some examples of the observational evidences that indicate the presence of counter-rotating components. Panel (a): Part of a 200-inch Palomar spectrum obtained along the major axis of NGC 4550. The spatial scale and wavelenght dispersion are 0.82 arcsec pixel^{-1} and 0.56 Å pixel^{-1}, respectively; the integration time is 2000 s. It shows the [O III] emission and several blueward absorption lines. Here, we can clearly see the X-shaped appearance of the absorption lines due to the superposition of the prograde and retrograde stellar disks. Image taken from Rubin et al. (1992). Panel (b): LOSVD along the major axis of NGC 4550 at various distances from the center. The thin line indicates the best Gaussian fit, while the thick line represents the double Gaussian fit. The LOSVDs are offset by arbitrary amounts. Inside 5 arcsec the LOSVD is indistinguishable from a simple Gaussian. At larger radii we can see a rapid transition to a bimodal distribution, with almost no overlap of the two components in the velocity space. Each of the two parts of the LOSVD represents one of the counter-rotating, co-spatial disks. Image taken from Rix et al. (1992). Panel (c): Stellar kinematics map of h_3 of the LOSVD of a simulated counter-rotating galaxy (see Section 3.3 of Rubino et al. 2021 for details). Here, $S/N = 20$ pixel^{-1}. The solid contours correspond to $|h_3|$ = 0.05. The h_3 pattern clearly indicates the presence of a counter-rotating stellar disk. Image taken from Rubino et al. (2021).

two components. However, this approach was feasible for only a few galaxies. In fact, it not only requires high-resolution spectroscopy, but also needs the two components to have distinct spatial scales. Without this distinction, it becomes difficult, if not impossible, to separate their contributions at a given radius. This is the reason why we want to complete the kinematic decomposition with a dynamical model.

1.3 Environment and morphology of counter-rotating galaxies

Bettoni et al. (2001) presented a statistical study of the environment of 49 galaxies hosting a gas or stellar counter-rotating disk, using a control sample of 43 galaxies without counter-rotation. They took into account the presence of possible nearby companions (up to an apparent magnitude of 22 mag arcsec^{-2}), size and concentration. They found that there was no significant difference between the counter-rotating and control samples. In fact, the morphology of most galaxies hosting counter-rotating components appears undisturbed, with no evidence of recent

interaction with small satellites or companions of comparable size. However, this is a matter of debate. Indeed, there is evidence that all types of kinematically misaligned galaxies in the sample presented by Jin et al. (2016) tend to live in low density areas, suggesting that a dense environment would suppress the external process of gas acquisition and formation of such galaxies. Furthermore, as observed by Beom et al. (2022) in a study of 523 edge-on galaxies from the final Mapping Nearby Galaxies at APO (MaNGA) Integral Field Units (IFU) sample (Bundy et al. 2015), gaseous counter-rotators are often found in small and loose groups. These galaxies exhibit low gas and dust content, weak emission lines, and low star formation rates suggesting that the formation of counter-rotators might be an effective way to quench star formation in galaxies. These results lead to the conclusion that the formation mechanism of these objects does not seem to be related to the current galaxy density of their environment. Therefore, the retrograde gas infall must be continuous and non-traumatic, major mergers must have occurred very early in their lives, and minor mergers could have occurred more recently without leaving any trace. However, the remnants of merger events, such as collisional debris and tidal tails, are generally faint and transient structures. Observing such a structure can be quite difficult because it requires deep optical imaging. These structures have a surface brightness of 25 B-mag arcsec^{-2} when they are young, and below 27 B-mag arcsec^{-2} as they age. They disappear after a time varying from a few hundred Myr to a few Gyr. Numerical simulations can help to constrain the epoch and the mechanism of the second event (Corsini et al. 2002; Duc et al. 2011). Counter-rotation in low-mass galaxies is associated with gas loss events that are either internally driven (e.g., due to feedback), externally driven (e.g., due to gas stripping from the environment), or a combination of both. As a result, galaxies that exhibit counter-rotation today may contain evidence of a past violent feedback episode or a complex environmental history (Starkenburg et al. 2019).

Moving now to morphology, to date no counter-rotating components have been detected in late-type spiral galaxies. Three of the few spirals with counter-rotating gaseous and/or stellar disks (NGC 3593, NGC 3626, and NGC 4138) are all early-type spirals (S0/a–Sa) with smooth arms. In these galaxies, the spiral pattern is either entirely shaped or heavily influenced by dust lanes. The suppression of arms in counter-rotating spirals was identified in high-resolution N-body simulations run by D'Onghia et al. (2013). These simulations show that mass concentrations (density inhomogeneities) with properties (mass and lifetime) similar to those of giant molecular clouds can induce the development of spiral arms through a process known as swing amplification. Moreover, a survey carried by Corsini et al. (2003), which selected a sample of early S0/a and Sa spirals with a spiral pattern traced by dust lanes, revealed the presence of kinematically decoupled gas components, but no new case of counter-rotation.

Previous 2D N-body simulations of disk galaxies with a significant fraction of counter-rotating stars predicted the formation of a stationary and persisting one-arm leading spiral wave (with respect to the corotating stars) due to the two-stream disk instability (Lovelace et al. 1997; Comins et al. 1997). However, identifying this one-armed spiral pattern in counter-rotating spirals has proved challenging because the spirals studied so far have intermediate-to-high inclinations, making detection difficult. Additionally, kinematic data for low-inclination, one-armed systems are currently lacking.

1.4 Statistics of counter-rotation

Using existing data on ionized-gas and stellar kinematics measured along (at least) the major axis of S0 galaxies, Pizzella et al. (2004) identified a kinematically-decoupled gaseous component in 17 out of 53 galaxies. This corresponds to 32^{+19}_{-8}% (at 95% confidence level). This is consistent with previous statistics by Bertola et al. (1992) (20%), Kuijken et al. (1996) (24±8%) and

Kannappan & Fabricant (2001) ($24\%^{+8}_{-6}$). These findings support the idea that acquisition events in S0 galaxies are not a characteristic of a few peculiar objects, but are, instead, a widespread phenomenon which affects a very large fraction of S0 galaxies with gas, as it does for ellipticals (Bertola et al. 1992). This scenario is also supported by the results of Davis et al. (2011), who used integral-field spectroscopy and radio observations. They found that the gas is kinematically misaligned with the stars in 36% (40/111) of rapidly rotating early-type galaxies. Furthermore, the ionized, molecular and atomic gas phases were always kinematically aligned with each other in galaxies where gas was detected, even when misaligned with the stars. This suggests a common origin for these gas phases, highlighting the importance of external acquisition events.

On the other hand, the situation is quite different for spiral galaxies. Pizzella et al. (2004) found that <12% and <8% (at 95% confidence level) of a sample of 50 S0/a-Scd galaxies host a counter-rotating gaseous and stellar disk, respectively. Similar statistics are observed by Kannappan & Fabricant (2001), who found that no more than 8% of Sa-Sbc spirals in a sample of 38 are bulk counter-rotators.

More recently, a statistical analysis of the frequency of counter-rotating stellar disks has been performed by Bevacqua et al. (2022). They presented the integral-field kinematics and stellar population properties of 64 galaxies with counter-rotating stellar disks selected from about 4000 galaxies in the MaNGA survey, based on evidence of counter-rotation or 2σ peaks in the kinematic maps. The frequency of counter-rotating stellar disks was found to be <5% for ellipticals, <3% for lenticulars, and <1% for spirals (at 95% confidence level). There is a decrease from early to late morphological types of the Hubble sequence.

Some other studies, as the one carried out by Jin et al. (2016), pointed out the relation between the fraction of kinematically misaligned galaxies and the physical parameters, such as stellar mass $M_\star$, star formation rate (SFR), and specific star formation rate (sSFR). This fraction peaks at a stellar mass of around $\log(M_\star/\mathrm{M}_\odot) \approx 10.5$ and decreases as SFR and sSFR increase.

1.5 Formation scenarios

Simulations and observations show that there are different formation channels that can explain the presence of a counter-rotating gaseous or stellar component inside the galaxy:

1. *Acquisition of external gas with different angular momentum.* Gas accretion from the external environment can be either episodic or prolonged. Once accreted, the material enters a retrograde orbit within the galaxy without drastically disturbing the stability of the existing disk (Thakar & Ryden 1996). As shown by Lovelace & Chou (1996), a counter-rotating disk will only be observed if the mass of the newly added gas exceeds that of the old, pre-existing disk. Therefore, the formation of counter-rotating gaseous disks is favored in gas-poor systems, like S0 galaxies, whereas their formation is hindered in gas-rich systems, like spirals (Bevacqua et al. 2022). This also explains why the mass of counter-rotating gas in most S0 galaxies is small compared to that of the stellar counter-rotating components (Kuijken et al. 1996). In addition, the accretion of counter-rotating gas from an existing co-rotating disk may be a transient stage in the formation of counter-rotating galaxies. In this framework, a counter-rotating stellar disk is the end result of star formation in a counter-rotating gas disk. Bao et al. (2022) presented a scheme of four formation scenarios for counter-rotating stellar disks in nearby galaxies with regularly rotating ionized-gas disks. The scheme is reported in Figure 1.2. The key factors in the formation of counter-rotating stellar disks are the abundance of pre-existing gas in the progenitor and the efficiency of angular momentum consumption. This scheme gives rise

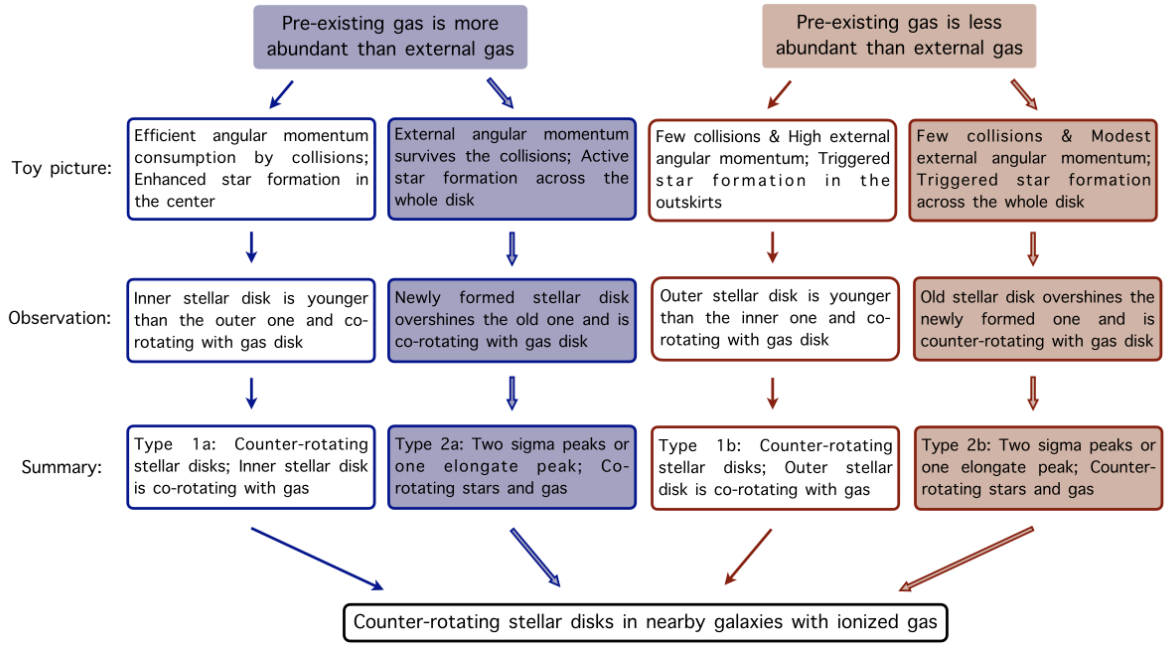

Figure 1.2: Scheme of the formation scenarios of counter-rotating stellar disks in nearby galaxies with regularly rotating ionized gas disks. Image taken from Bao et al. (2022).

to four scenarios: Type 1a, 1b, 2a, and 2b. In Type 1a, collisions between preexisting and external gas effectively consume angular momentum, leading to gas inflow and triggering star formation in the central region. Additionally, Type 1a has a slightly younger stellar population in the central region compared to Type 1b. In Type 2a, part of the angular momentum of the external gas survives the gas-gas collisions, allowing newly formed stars to spread across the entire disk and outshine the older stars. Conversely, in the Type 1b and 2b scenarios, the preexisting gas is less abundant than the accreted gas. As a result, star formation in Type 1b occurs in the outskirts, producing a younger outer disk that corotates with the gas. In Type 2b, the newly formed stars also spread across the whole disk, but star formation is less active than in Type 2a.

Angular momentum loss is not only an important property in itself, but also the primary driver for subsequent processes. In fact, in the internal-origin scenarios, if pre-existing corotating gas is present, the formation of a counter-rotating gaseous disk can lead to angular momentum loss in the gas through hydrodynamic friction, resulting in a centrally concentrated gas distribution (Beom et al. 2022). Gas infall removes pre-existing gas, which then mixes with the infalling material. This mixture forms a counter-rotating gaseous disk, where about 90% of counter-rotating stars are formed in situ. In the early stages of infall, the gas can appear in extended structures, sometimes resembling nearly polar ring-like components in certain galaxies (Corsini et al. 2002; Khoperskov et al. 2021). This concentration can trigger central star formation and, in the presence of a nuclear black hole, can potentially fuel an active galactic nucleus (AGN). Therefore, gaseous counter-rotating galaxies may be also interesting as a possible evolutionary stage in the transition to quiescent galaxies (Khoperskov et al. 2021; Beom et al. 2022).

Another mechanism that can lead to the acquisition of small amounts of external gas is the merging of the galaxy with a gas-rich dwarf companion. To produce counter-rotation of stars or gas within a merger remnant, the primary galaxy must have a retrograde spin. The

spin of the companion mainly influences the radial extent of the accreted gas. Additionally, having a significant amount of gas in the primary galaxy can prevent counter-rotating gas from forming, though counter-rotating stars can still emerge (Bassett et al. 2017). However, the minor merging mechanism seems to produce non-massive counter-rotating disks (Thakar & Ryden 1996). This is the case of NGC 4138, studied by Thakar et al. (1997) and Thakar & Ryden (1998).

2. *Merging of two galaxies.* Puerari & Pfenniger (2001) studied the case of major mergers between progenitors of comparable mass. They found that, while in general this scenario can be ruled out because it tends to produce ellipticals (see also Hernquist & Barnes 1991), for a narrow range of initial conditions major mergers can still be viable alternatives for the formation of counter-rotating systems. The scenario succeeds in producing a remarkably axisymmetric disk hosting strongly counter-rotating stellar components of similar size and mass. Moreover, if the merging of the two progenitors is coplanar, then the net result is a greater heating of the prograde stellar disk than of the retrograde one. Furthermore, the gas ends up aligned with the total angular momentum, which is dominated by the orbital angular momentum, and thus with the prograde stellar disk, as observed in NGC 4550 (Crocker et al. 2009). More recently, Zeng et al. (2021) has shown that major mergers with a spiral in-falling orbit mostly lead to disk galaxies.

3. *Hierarchical clustering.* Cosmological simulations performed by Algorry et al. (2014) revealed another viable external formation process. The simulated disk galaxy features two overlapping stellar components with opposite spins: an inner, counterrotating bar-like structure composed mostly of older stars, and an extended, rotationally supported disk of younger stars. These opposite-spin components are formed from material accreted from two distinct filamentary structures. Therefore, the counterrotating stellar disk components may arise naturally in hierarchically clustering scenarios even in the absence of merging, and most stars in the galaxy are formed in situ.

4. *Dissolution of an internal pre-existing component.* While the previous two scenarios involve the acquisition of an external component (external-origin scenario), this one justifies the presence of a counter-rotating stellar component by the dissolution of an internal component (internal-origin scenario), as a bar or stellar halo. It was first proposed by Evans & Collett (1994) in the study of NGC 4550 and is based on the migration of stars from box orbits to tube orbits, escaping the potential well and crossing the orbit separatrix. In non-rotating disks, looking at box orbits, the number of orbits with clockwise azimuthal motion is equal to the number of orbits with counter-clockwise azimuthal motion. Thus, half of the stars in box orbits are scattered on clockwise orbits, while half are scattered on counter-clockwise orbits. This is a natural mechanism for forming two identical counter-rotating stellar disks, characterized by the same age and same scale length.

   Some other internal-origin scenarios include stars trapped at the Binney resonance (Tremaine & Yu 2000) and the increase in the number of retrograde stars due to the exchange of angular momentum with the bar (Pfenniger & Friedli 1991).

5. *Counter-rotation in barred galaxies.* Analyzing 14 barred galaxies, Bettoni & Galletta (1997) found that these galaxies host quasi-circular orbits, with deviations from circular velocities lower than 20%. Therefore, counter-rotation observed in these types of galaxies can be the net result of internal dynamical processes (Wozniak & Pfenniger 1997). This counter-rotating material could lead to the formation of a secondary bar that rotates in the opposite direction to the main bar (Sellwood & Merritt 1994). Observationally, the

formation of secondary bars might be better understood by examining the occurrence of counter-rotating secondary bars. The widely accepted theory is a mechanism, applicable to AGNs and nuclear starburst galaxies, which brings in gas from large to small scales by successive dynamical instabilities (Shlosman et al. 1989). However, a retrograde bar is unlikely to form within a prograde disk. Numerical simulations suggest that two counter-rotating nested bars, formed within overlapping counter-rotating stellar disks, are stable and long-lived (Friedli 1996). This raises the possibility that secondary bars could originate from inner stellar disks, similar to those found in the nuclei of several disk galaxies (Pizzella et al. 2003; Ledo et al. 2010; Corsini et al. 2016). So far, counter-rotating nuclear disks have been detected only in elliptical galaxies (e.g. Morelli et al. 2004).

1.6 Stellar population of counter-rotating components

The age, metallicity, and enhancement of α elements that characterize the counter-rotating stellar disk depend strongly on the formation mechanism. In fact, gas acquisition and subsequent star formation would necessarily lead to a younger counter-rotating stellar population, which can also be characterized by different values of metallicity and α-enhancement. The same is true for the major merger scenario, although in this case the age of the counter-rotating galactic disk is not forced to be younger than the pre-existing component, but depends on the properties of the progenitor, as it does for metallicity and α-enhancement. On the other hand, the internal-origin scenario necessarily implies that both the co-rotating and counter-rotating stellar disks have the same age, metallicity, and α-enhancement. Therefore, the age difference between the prograde and retrograde stellar populations can be used to discriminate between competing scenarios for the origin of the counter-rotation.

To disentangle the stellar populations, it is necessary to perform a spectroscopic decomposition that isolates the contributions of the counter-rotating stellar components within the observed galaxy spectrum. This analysis was applied to some counter-rotating stellar disk galaxies, as NGC 3593 (Coccato et al. 2013), NGC 4550 (Johnston et al. 2013; Coccato et al. 2013), NGC 5719 (Coccato et al. 2011), NGC 1366 (Morelli et al. 2017), and SDSS J074834.64+444117.8 (Bao et al. 2024). These findings rule out an internal origin of the secondary stellar component, and favor a scenario in which gas accreted from the surrounding environment on retrograde orbits, leading to rapid in-situ star formation that progressed from the outer regions inwards. This is consistent with the statistics discussed in Section 1.4. For a counter-rotating stellar disk to form from gas accretion, any existing gas in the progenitor galaxy must first be cleared away. As a result, gas-poor galaxies, like ellipticals, are more likely to host counter-rotating disks compared to gas-rich galaxies, like spirals. This also explains why no late-type spirals have been observed with counter-rotating stellar disks, as they typically contain more gas than early spirals (Bevacqua et al. 2022).

The Sab spiral galaxy NGC 5719, studied by Coccato et al. (2011), is a particularly intriguing case. This galaxy is currently interacting with its Sbc companion, NGC 5713. By simultaneously measuring the kinematics and properties of the two stellar components, they were able to observe not only the capture of gas in retrograde orbits, but also the subsequent formation of new stars, thereby providing evidence of young counter-rotating stars (see Figure 2 in Corsini 2014 for an explanation and visual representation of the process). NGC 5719 is the first known interacting disk galaxy where counter-rotation has been detected.

1.7 Aim and summary of the thesis

This thesis is focused on the highly-inclined S0 galaxy NGC 1366 in the Fornax cluster, which is known to host a stellar component that is kinematically decoupled from the main body of the galaxy (Morelli et al. 2008). According to a parametric spectroscopic decomposition of the spectrum obtained along the galaxy major axis, the counter-rotating stellar component is younger, has nearly the same metallicity, and has a lower overabundance than the co-rotating component (Morelli et al. 2017). The aim of this thesis is building two-integrals exploratory dynamical models of NGC 1366 using an original numerical code dedicated to the solution of the Jeans equations (JEs) in axisymmetric multicomponent systems. The application to NGC 1366 represents a pilot project to fine tune dynamical modelling to dissect counter-rotating disk galaxies, derive the stellar population properties of their kinematically-decoupled components, and finally constrain their formation mechanism.

The thesis is organised as follows:

- In Chapter 1 we introduce and explain the phenomenon of counter-rotation. In Section 1.1 we explore the different types of counter-rotation. In Section 1.2 we focus on the tools used to detect counter-rotation. In Section 1.3 we examine the environment and morphological features of counter-rotating galaxies. In Section 1.4 we present the statistical data on counter-rotating galaxies. In Section 1.5 we examine the different scenarios that could explain their formation. In Section 1.6 we discuss the different stellar populations found in counter-rotating components.

- In Chapter 2 we focus on the galaxy NGC 1366, for which we already have a kinematic decomposition. In Section 2.1 we provide the general information about the galaxy. In Section 2.2 we detail the photometric and spectroscopic observations along with the data reduction process. In Section 2.3 we present the photometric decomposition of NGC 1366 and derive its photometric parameters. In Section 2.4 we explore the kinematic properties of NGC 1366. In Section 2.5 we discuss the kinematic parameters and line strength indices, calculate the mass-to-light ratio for each component, and determine the luminosities and masses of the individual components as well as of the entire galaxy.

- In Chapter 3 we present the theoretical background for the construction of the dynamical model of NGC 1366. In Section 3.1 we discuss how to recover the luminosity volume density profile from the surface brightness profile for both the bulge and disk. In Section 3.2 we introduce the first and second JEs, for which we adopt the solution for the axisymmetric mass distribution. In Section 3.3 we present the solution for the forces in the JEs, using the Chandrasekhar formula. In Section 3.4 we provide a solution of the first and second JEs, also presenting the Satoh decomposition method. In Section 3.5 we combine the values of the fields obtained from the JEs, weighting them both by mass and luminosity, and examining how to retrieve physical units.

- In Chapter 4 we present and describe the numerical code used to model NGC 1366 and its results. In Section 4.1 we present the software used in our code and our initial assumptions. In Section 4.2 we reproduce the luminosity surface density of the galaxy. In Section 4.3 we solve the first JE, obtaining σ_z. In Section 4.4 we solve the second JE, obtaining $\sqrt{\Delta_\sigma}$ and $\sqrt{\overline{v_\varphi^2}}$. Then, we obtain $\overline{v_\varphi}$ and σ_φ for five pairs of the Satoh parameters. In Section 4.5 we compare models and integral-field spectroscopic observations. In Section 4.6 we compare models and long-slit spectroscopic observations.

- In Chapter 5 we summarize the results of our work, and discuss its possible future developments. In Section 5.1 we summarize the conclusions drawn from the comparison between observations and models, along with suggestions for possible improvements. In Section 5.2 we outline prospective directions for extending this work.

Chapter 2

Observational data and properties of NGC 1366

In this chapter we focus on the galaxy NGC 1366, for which we already have a kinematic decomposition. In Section 2.1 we provide the general information about the galaxy. In Section 2.2 we detail the photometric and spectroscopic observations along with the data reduction process. In Section 2.3 we present the photometric decomposition of NGC 1366 and derive its photometric parameters. In Section 2.4 we explore the kinematic properties of NGC 1366. Finally, in Section 2.5 we discuss the kinematic parameters and line strength indices, calculate the mass-to-light ratio for each component, and determine the luminosities and masses of the individual components as well as of the entire galaxy.

2.1 General properties

NGC 1366 is a bright and spindle galaxy located in the Fornax cluster. The equatorial coordinates (J2000) of NGC 1366 are (RA, δ) =($3^{\rm h}$ $33^{\rm m}$ $53.3^{\rm s}$, -31° $11'$ $36''$) (de Vaucouleurs et al. 1991, hereafter RC3). The position angle of the major axis is PA = 2° (RC3). The redshift-independent distance of the galaxy is D = (17.64±1.62) Mpc[1]. It is classified as $S0^0$ by RC3 and as $S0_1(7)$/E7 by Sandage & Bedke (1994) because it has a highly inclined thin disk. Although NGC 1366 belongs to the LGG 96 group (Garcia 1993), it has no nearby bright companion and shows an undisturbed morphology. Its apparent total magnitude is B_T = 11.97 mag (RC3). The apparent isophotal diameters measured at a surface brightness level of μ_B = 25 mag arcsec^{-2} are 2.1 × 0.9 arcmin, corresponding to 10.8 × 4.6 kpc. Its total B magnitude corrected for extinction and inclination is $M_{B_T,0} = -18.48$ mag, obtained rescaling $B_{T,0}$ from RC3 to the adopted distance. The surface brightness distribution is well fitted by a Sérsic bulge and an exponential disk with a bulge-to-total luminosity ratio B/T = 0.2 (Morelli et al. 2008). These authors detected a kinematically decoupled stellar component that is younger than the host bulge. Furthermore, Morelli et al. (2017) succeeded in separating the two counter-rotating components and properly measuring the properties of their stellar populations. The analysis of the kinematics of the stars and ionized gas and of the stellar populations is consistent with the formation of the counter-rotating component from external gas that is still accreting onto the galaxy. An image of NGC 1366 is shown in Figure 2.1.

The choice of this galaxy NGC 1366 is also related to its simplicity since it is edge on: the flattening parameters of bulge and disk obtained from observations correspond to the intrinsic

[1]From Nasa Extragalactic Database (NED).

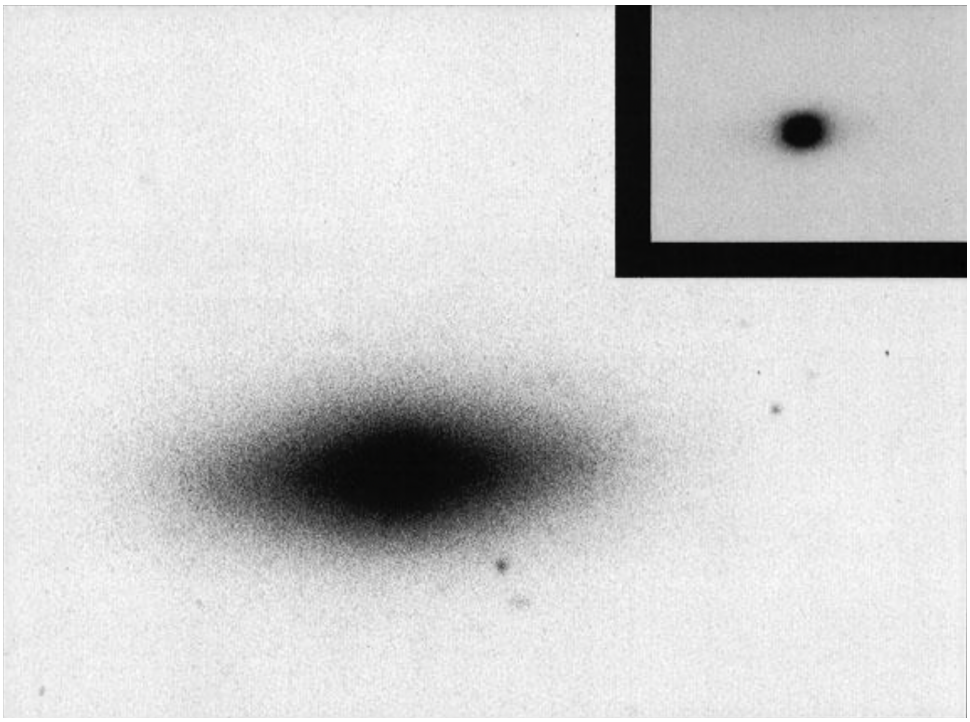

Figure 2.1: Image of NGC 1366. This photographic image was obtained with the du Pont telescope using the 103aO filter. It has a field of view (FOV) of 5.2×3.8 arcmin^2 and is oriented with north to the right and east to the top. Image taken from Sandage & Bedke (1994).

parameters. This simplifies our calculation because we do not have to take into account for viewing angle corrections, so we will not have any geometrical difficulty in our work.

2.2 Observations and data reduction

This section provides the details of the photometric and spectroscopic observations, as well as the data reduction process, performed by Morelli et al. (2008, 2017).

2.2.1 Broad-band imaging

The photometric observations of NGC 1366 took place at the European Southern Observatory (ESO) in La Silla (Chile). They were carried out by Morelli et al. (2008) on 2002 December 11.

NGC 1366 was imaged at the ESO 3.6-m Telescope with the ESO Faint Object Spectrograph and Camera 2 (EFOSC2). The detector was the No. 40 Loral/Lesser CCD with 2048×2048 pixel of 15×15 μm^2. A 2×2 pixel binning was adopted giving an effective scale of 0.314 arcsec pixel^{-1} with a FOV of 5.3×8.6 arcmin^2. The gain was set to 1.3 e$^-$ ADU^{-1} and readout noise to 9 e$^-$.

The No. 642 Bessel R-band filter was used for the observations. It is centered at 6431 Å and has a full width at half-maximum (FWHM) of 1654 Å. Two 60-s images were taken with an offset of few pixels, which were used to clean cosmic rays and bad pixels. To perform the flux calibration, several fields of standard stars at different airmasses were observed each night. For each field different exposures ranging from 5 to 15 s were taken, so to have good S/N and well-sampled point spread function (PSF) for all the standard stars. The typical value of the seeing FWHM during the galaxy exposures was 1.0 arcsec as measured by fitting a 2D Gaussian

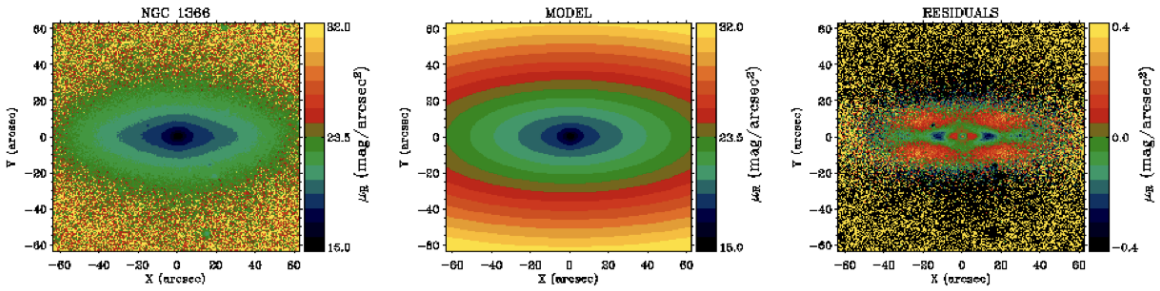

Figure 2.2: Map of the observed (left panel), modelled (central panel) and residual (observed−modelled) surface brightness distribution (right panel) of NGC 1366. The image was rotated to have the galaxy major axis parallel to rows. The surface brightness range is indicated at the right-hand side of the panel. Image taken from Morelli et al. (2008).

to the field stars.

The reduction of the photometric observations was described in Morelli et al. (2008). The reduction procedure of the images was carried on using standard IRAF[2] tasks. A bias frame, consisting of 10 exposures for each night, was subtracted. The sky background level was removed by fitting a Legendre polynomial to the source-free regions in the images. No trace of scattered light was detected in the images, and the adopted polinomial degree was either 0 or 1. Cosmic rays and bad pixels were removed by combining the different exposures using field stars as a reference and applying a sigma clipping rejection algorithm. Remaining cosmic rays and bad pixels were corrected by manually editing the final combined image.

The photometric calibration constant includes only the correction for atmospheric extinction, which is taken from the differential aerosol extinction for ESO (Burki et al. 1995). No correction was applied for galactic extinction, and no color term was considered.

After masking foreground stars and residuals bad columns, isophote-fitting with ellipses was carried out using the IRAF task ELLIPSE. At first, the ellipses centers were allowed to vary. No variation of the ellipses centers was found. The final ellipse fits were done at fixed ellipse centers. Figure 2.2 shows the observed, modelled and residual (observed−modelled) surface brightness distribution maps derived for NGC 1366 by Morelli et al. (2008).

2.2.2 Long-slit and integral-field spectroscopy

The spectroscopic observations of NGC 1366 took place with the 3.6-m ESO telescope and EFOSC2 spectrograph. They were carried out by Morelli et al. (2008) on 2002 December 11.

The grism No. 9 with 600 grooves mm^{-1} was used in combination with the 1.0 arcsec × 5.0 arcmin slit. The detector was the No. 40 Loral/Lesser CCD with 2048 × 2048 pixel of 15 × 15 μm^2. A 2 × 2 pixel binning was adopted. The wavelength range between 4700 and 6770 Å was covered with a reciprocal dispersion of 1.98 Å $pixel^{-1}$ after pixel binning. In this way, an adequate oversampling of the instrumental broadening function was guaranteed. By measuring the width of the emission lines of a comparison spectrum after the wavelength calibration, the instrumental dispersion could be calculated, and was found to be 5.10 Å (FWHM). This corresponds to $\sigma_{inst} \sim 110$ km s^{-1} at 5735 Å. The spatial scale was 0.314 arcsec $pixel^{-1}$ after pixel binning.

[2]Image Reduction and Analysis Facility (IRAF) is distributed by the National Optical Astronomy Observatory (NOAO), which is operated by the Association of Universities for Research in Astronomy (AURA), Inc. under cooperative agreement with the National Science Foundation.

Two 45-min spectra were obtained. At the beginning of each exposure, the slit was positioned on the galaxy nucleus using the guiding camera. Then, according to the position angle, it was aligned along the galaxy major axis. During the three observing runs several giant stars were selected from Worthey et al. (1994). Their spectra were used as templates to measure stellar kinematics and line-strength indices. In addition, some spectrophotometric standard stars were measured prior to the line index measurements in order to flux-calibrate the galaxy and line-strength standard stars. During the galaxy exposures, the value of the seeing FWHM ranged between 0.5 and 1.3 arcsec as measured by fitting a 2D Gaussian to the guide star.

The reduction of the spectroscopic observations was described in Morelli et al. (2008). All spectra were bias subtracted, flat-field corrected, cleaned of cosmic rays, and wavelength calibrated using standard IRAF routines. In order to check the CCD status, the bias level was determined from the bias frames obtained during the observing nights. Flat-field correction was carried out using both quartz lamp and twilight sky spectra to correct for pixel-to-pixel sensitivity variations and large-scale illumination patterns caused by slit vignetting. The sky spectra were normalized and divided into all the observed spectra. Cosmic rays were identified by comparing the counts in each pixel with the local mean and standard deviation as obtained from Poisson statistics taking into account detector gain and readout noise. They were then corrected by interpolation. The residual cosmic rays were corrected by manually editing the spectra. The wavelength solution obtained from the corresponding arc lamp spectrum was used to rebin each spectrum. To check if the wavelength rebinning was done properly, difference between the measured and predicted wavelengths were computed for the brightest night-sky emission lines in the observed spectral range (Osterbrock et al. 1996). The resulting accuracy in the wavelength calibration came out to be better than 5 km s^{-1}. All spectra were corrected for CCD misalignments. The spectra obtained in the same run were co-added using the centre of the stellar continuum as reference. In this way it was possible to improve the S/N of the resulting 2D spectrum. In such a spectrum, the contribution of the sky was determined by interpolating a straight line along the outermost 20 arcsec at the two edges of the slit, where the galaxy light was negligible. After that, the sky contribution was subtracted. A sky subtraction better than 1% was achieved. For each kinematic template star and flux standard star, a 1D spectrum was obtained. The spectra of the kinematical templates were deredshifted to laboratory wavelengths.

The integral-field spectroscopic observations of NGC 1366 were carried out with the MUSE (Multi Unit Spectroscopic Explorer) instrument of the ESO. They were carried out by Morelli et al. (in prep.) between 2019 August 9 and August 30.

MUSE was configured in wide field mode to guarantee a FOV of 1×1 arcmin^2, with a spatial sampling of 0.2 arcsec pixel^{-1}. The MUSE spectroscopic range covers 4800 to 9300 Å with a spectral sampling of 1.25 Å pixel^{-1} and an average nominal spectral resolution with a FWHM = 2.51 Å (Bacon et al. 2010). A central pointing on the galaxy centre was performed, followed by two off-set pointings along the major axis at a distance of 20 arcsec eastward and westward from the nucleus of the galaxy. Each of these four pointings had a duration of ∼35 min. Each pointing was oriented along the disk PA. The observing nights were clear. The FWHM seeing was mostly < 1.4 arcsec.

The reduction of the integral-field spectroscopic observations was done as in Cuomo et al. (2019). The data reduction was performed using the MUSE pipeline (version 2.8.4, Weilbacher et al. 2020) under the EXOREFLEX environment (Freudling et al. 2013). The steps included bias and overscan subtraction, lamp flatfielding to correct the pixel-to-pixel response variation of the detectors and illumination edge effects between the detectors, wavelength calibration, determination of the line spread function, sky flatfielding to correct the large-scale illumination variation of the detector, sky subtraction, flux calibration with correction for atmospheric transmission and differential refraction. Twilight flatfield exposures were combined following

the same observing pattern of the on-target and on-sky exposure. In this way a master twilight datacube was produced to determine the effective spectral resolution and its variation across the FOV. An instrumental FWHM = 2.80 Å ($\sigma_{\rm instr}$ = 69 km s^{-1}) was found, with a negligible variation over the FOV and in the wavelength range between 4800 and 5600 Å. With this analysis, it was possible to measure the stellar kinematics. The sky contribution was estimated by fitting the sky continuum and emission lines on the on-sky exposures. The resulting sky model spectrum was then subtracted from each spaxel of the on-target and on-sky exposures. A combined datacube on the galaxy was produced aligning the sky-subtracted on-target exposures using the common bright sources in the FOV as reference. The residual sky contamination of the resulting sky-subtracted datacube was further cleaned using the Zurich Atmospheric Purge (ZAP) algorithm (Soto et al. 2016).

2.3 Photometric properties

The photometric decomposition of NGC 1366 was carried out by Morelli et al. (2008). This study aimed at investigating the stellar population of bulges in 14 S0 and spiral galaxies across various clusters and groups. They conducted a 2D photometric decomposition of the R-band surface-brightness distribution of the sample galaxies.

The surface brightness distribution of each galaxy was modeled as the sum of two components: a bulge, described by a Sérsic law, and a disk, represented by a type I Freeman law. To model the bulge isophotes, ellipses centered at (x_0, y_0) were used, with a fixed position angle $\mathrm{PA_b}$ and a constant axial ratio $q_{\rm b}$. Similarly, the disk isophotes were represented by ellipses centered at (x_0, y_0), with a constant position angle $\mathrm{PA_d}$ and a fixed axial ratio $q_{\rm d}$. In Morelli et al. (2008) Cartesian coordinates (x, y, z) were used, so that the origin corresponded to the position of the galaxy surface brightness peak, the x-axis was parallel to the direction of right ascension and pointing west, the y-axis was parallel to the direction of declination and pointing north, and the z-axis was along the line of sight and pointing towards the observer. In this way, the plane of the sky was confined to the (x, y) plane and the radii r for the two profiles were written as:

$$r_{\rm b} = \sqrt{[-(x-x_0)\sin\mathrm{PA_b} + (y-y_0)\cos\mathrm{PA_b}]^2 + \frac{[-(x-x_0)\cos\mathrm{PA_b} + (y-y_0)\sin\mathrm{PA_b}]^2}{q_{\rm b}^2}} \quad , \tag{2.1}$$

$$r_{\rm d} = \sqrt{[-(x-x_0)\sin\mathrm{PA_d} + (y-y_0)\cos\mathrm{PA_d}]^2 + \frac{[-(x-x_0)\cos\mathrm{PA_d} + (y-y_0)\sin\mathrm{PA_d}]^2}{q_{\rm d}^2}} \quad . \tag{2.2}$$

Nevertheless, in the following we will consider Cartesian coordinates rotated by an angle $\mathrm{PA_i}$ with respect to the previous choice, where $i = \{\mathrm{b}, \mathrm{d}\}$ depending on the component we are considering, so that the axis lies along the major and minor axes of the galaxy, and translated by (x_0, y_0), so that the origin is placed at $(0, 0)$.

The functional form used in Morelli et al. (2008) to describe the bulge profile is:

$$I_{\rm b}(l_{\rm b}) = I_{\rm e} 10^{-b_n\left[(l_{\rm b})^{\frac{1}{n}}-1\right]} \quad , \qquad \text{where} \quad l_{\rm b} = \frac{r_{\rm b}}{r_{\rm e}} = \frac{\sqrt{R^2 + \frac{z^2}{q_{\rm b}^2}}}{r_{\rm e}} \quad . \tag{2.3}$$

$r_{\rm e}$ is the effective radius, $I_{\rm e}$ is the surface brightness measured at $r_{\rm e}$, $q_{\rm b}$ is the flattening and b_n is a constant obtained from the condition $L(r_{\rm e}) = \frac{L_{tot}}{2}$. The subscript b stands for "bulge". A relatively simple expression can be found for b_n from Caon et al. (1993):

$$b_n = 0.868n - 0.142 \quad . \tag{2.4}$$

In our code we use a different (analogous) expression for the Sérsic bulge, which has e as the base of the exponent instead of 10 (Sérsic 1963):

$$I_{\rm b}(l_{\rm b}) = I_0 e^{-b_n (l_{\rm b})^{\frac{1}{n}}} \quad , \quad \text{where} \quad l_{\rm b} = \frac{r_{\rm b}}{r_{\rm e}} = \frac{\sqrt{R^2 + \frac{z^2}{q_{\rm b}^2}}}{r_{\rm e}} \quad . \tag{2.5}$$

In this case, I_0 is the central surface brightness. The expression for b_n can be obtained by standard asymptotic analysis (Ciotti & Bertin 1999):

$$b_n = 2n - \frac{1}{3} + \frac{4}{405n} + ... \quad . \tag{2.6}$$

It is important to note that, while Equation (2.5) is expressed in terms of I_0 (central surface brightness), Equation (2.3) is written in terms of $I_{\rm e}$ (effective surface brightness). However, the transition from one formula to the other is straightforward. By dividing Equation (2.5) by the same equation evaluated at $r_{\rm e}$, and then dividing the results, we can obtain the desired relationship:

$$\frac{I_{\rm b}(l_{\rm b})}{I_{\rm e}} = \frac{I_0 e^{-b_n (l_{\rm b})^{\frac{1}{n}}}}{I_0 e^{-b_n}} = e^{-b_n \left[(l_{\rm b})^{\frac{1}{n}} - 1 \right]} \tag{2.7}$$

$$\implies I_{\rm b}(l_{\rm b}) = I_{\rm e} e^{-b_n \left[(l_{\rm b})^{\frac{1}{n}} - 1 \right]} \quad . \tag{2.8}$$

The two expressions for b_n given by Equation (2.4) and Equation (2.6) are coherent with each other. In fact, we can easily get that $b_{n,\rm Ciotti} = \log_{\rm e} 10 \, b_{n,\rm Caon}$, where the factor $\log_{\rm e} 10$ is the one that results from changing the base of the exponential from base 10 to base e. Having established the analogy between these equations, from now on we will use Equation (2.5) to describe the surface brightness distribution of the bulge.

On the other hand, the equation used to describe the disk is that of a first-type exponential disk with no break at any radius (Freeman 1970):

$$I_{\rm d}(l_{\rm d}) = I_0 e^{-l_{\rm d}} \quad , \quad \text{where} \quad l_{\rm d} = \frac{r_{\rm d}}{h} = \frac{\sqrt{R^2 + \frac{z^2}{q_{\rm d}^2}}}{h} \quad . \tag{2.9}$$

I_0 is the central surface brightness, h is the scale length and $q_{\rm d}$ is the flattening. The subscript d stands for "disk". We have used $l_{\rm d}$ and $l_{\rm b}$ to distinguish between the two profiles. Equation (2.9) is very similar to Equation (2.5) with $n = 1$, but without the presence of the constant b_n. In fact, b_n is "contained" within h. Nevertheless, we can go back to the Sérsic profile and write

$$I_{\rm d}(l_{\rm d}) = I_0 e^{-b_1 \, l_{\rm d}} \quad , \quad \text{where} \quad l_{\rm d} = \frac{r_{\rm d}}{h_{\rm e}} = \frac{\sqrt{R^2 + \frac{z^2}{q_{\rm d}^2}}}{h_{\rm e}} \quad , \tag{2.10}$$

where b_1 is obtained from Equation (2.6) with $n = 1$, and $h_{\rm e} = h \, b_1$. This last expression for the disk is the one we use in our code.

To derive the photometric parameters of the bulge ($I_{\rm e}$, $r_{\rm e}$, n, $\rm PA_b$ and $q_{\rm b}$) and disk (I_0, h, $\rm PA_d$ and $q_{\rm d}$) and the position of the center of NGC 1366 (x_0, y_0), Morelli et al. (2008) fitted iteratively $I_m(x, y) = I_{\rm b}(x, y) + I_{\rm d}(x, y)$ to the pixels of the galaxy image using a non-linear least-squares minimization based on the Levenberg–Marquardt method by Moré et al. (1980). The photometric decomposition technique adopted was the one developed in GASP2D (GAlaxy Surface Photometry 2 Dimensional Decomposition) by Méndez-Abreu et al. (2008). The actual

computation has been done using the MPFIT algorithm implemented under the IDL[3] environment. Each image pixel was weighted according to the variance of its total observed photon counts due to the contribution of both the galaxy and sky. Furthermore, it was determined assuming photon noise limitation and accounting for detector readout noise. Seeing effects were accounted for by convolving the model image with a circular Gaussian PSF with the FWHM measured from the stars in the galaxy image. The convolution was performed as a product in Fourier domain before the least-squares minimization. The values obtained by performing a standard photometric decomposition with a parametric technique similar to that adopted by Kormendy (1977) were adopted as initial trial for least-square minimization.

The fitting of the ellipse-averaged surface brightness profile of NGC 1366 was done in two steps: first the light contributions of the bulge and the disk were considered separately, and then simultaneously. Initially, an exponential law was fitted to the surface brightness profile of the galaxy at large radii. In fact, in this region the galaxy is dominated by the light contribution of the disk. In this way, I_0 and h were derived. After that, the exponential profile was extrapolated to small radii, and was subtracted from the galaxy surface brightness profile. In this way, a first estimate of the light distribution of the bulge was estimated. A Sérsic profile was then fitted by assuming that the bulge shape parameter n varies from 0.5 to 6 in increments of 0.5, and deriving the corresponding values of I_e and r_e. Finally, for each set of I_e, r_e, n, I_0 and h, both bulge and disk were fitted simultaneously to the galaxy surface brightness profile. Those giving the best fit were assumed as the trial values for the 2D fit, where all the parameters were allowed to vary.

The trial values of PA_b and q_b were obtained by interpolating at r_e the ellipse-averaged position angle and ellipticity profiles, respectively. The coordinates of the image pixel where the maximum galaxy surface brightness was measured were assumed as the trial values of the coordinates (x_0, y_0) of the galaxy center. The result of the photometric decomposition of the surface brightness distribution of NGC 1366 is shown in Figure 2.3. The errors associated to each photometric parameter were obtained through a series of Monte Carlo simulations, as described in Morelli et al. (2008).

The values of the structural parameters of the bulge obtained by Morelli et al. (2008) are listed in Table 2.1.

Table 2.1: Bulge photometric parameters of NGC 1366.

Parameter	Value
μ_e	(18.00 ± 0.04) mag arcsec^{-2}
r_e	(2.59 ± 0.07) arcsec
n	(1.50 ± 0.03)
q_b	(0.80 ± 0.01)
PA_b	$(5.38 \pm 2.40)^\circ$

Note: values taken from Table 2 of Morelli et al. (2008).

The values of the structural parameters of the disk obtained by Morelli et al. (2008) are listed in Table 2.2.

We now have to perform unit conversions to transform measurements from observed (magnitude and arcsecond) to astrophysical (solar luminosity and kiloparsec) units.

[3]Interactive Data Language (IDL) Environment System Variables is a proprietary programming language distributed by NV5 Geospatial, which was originally developed by Research Systems Inc. (RSI).

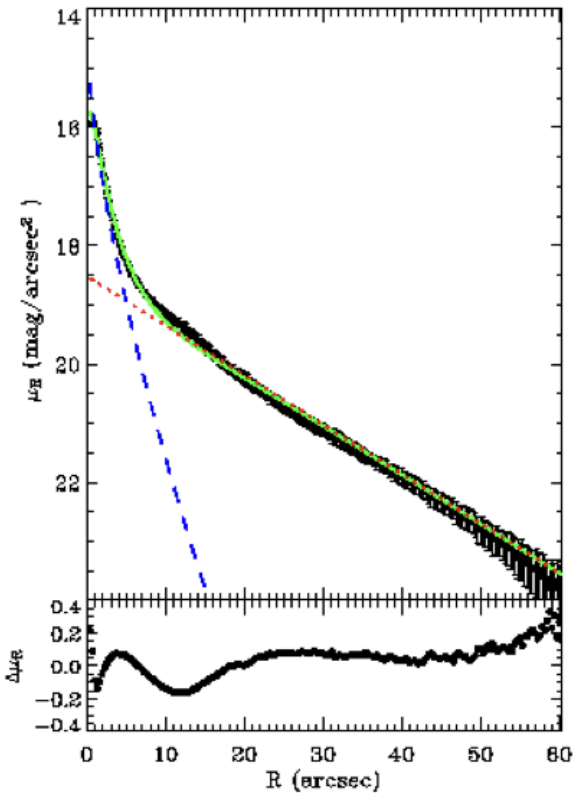

Figure 2.3: Ellipse-averaged radial profile of the surface brightness of NGC 1366. Upper panel: the total observed light profile (black filled circles [●]) is well reproduced by the sum (green solid line [—]) of an exponential disk with no break at any radius (red dotted line [· ·]) and a Sérsic bulge (blue dashed line (- -)). Lower panel: difference between the ellipse-averaged radial surface-brightness profiles extracted from the observed and modeled images. Image taken from Morelli et al. (2008).

Considering that from Morelli et al. (2008) the structural parameters of the galaxy were derived from R-band images, the equation that allows us to convert the surface brightnesses μ (mag arcsec^{-2}) of Tables 2.1 and 2.2 to I ($L_\odot$ pc^{-2}) of Equations (2.5) and (2.10) is:

$$\begin{aligned} & \mu = -2.5 \log I + \mu_{R,\odot} \\ \Longrightarrow \quad & I = 10^{-0.4(\mu-\mu_{R,\odot})}\ L_\odot\ \mathrm{pc}^{-2} = 10^{-0.4(\mu-26.03)}\ L_\odot\ \mathrm{pc}^{-2} = \\ & = 10^{-0.4(\mu-26.03)} \cdot 10^{-4}\ L_\odot\ \mathrm{kpc}^{-2} \quad , \end{aligned} \tag{2.11}$$

where $\mu_{R,\odot}$ is the surface brightness of the Sun in the R band, which can be obtained from:

$$\mu_{R,\odot} = M_{R,\odot} + 5\ \log(206265) - 5 = 4.46 + 5\ \log(206265) - 5 = 26.03\ \mathrm{mag\ arcsec}^{-2} \quad , \tag{2.12}$$

where $M_{R,\odot} = 4.46$ mag[4] As far as the length conversion concerns, we need to find the scale of the system. From the adopted distance we have:

$$s = \frac{17.6 \cdot 10^6\ \mathrm{pc}}{206265\ \mathrm{arcsec}} = 85.33\ \mathrm{pc\ arcsec}^{-1} = 8.53\,10^{-2}\ \mathrm{kpc\ arcsec}^{-1} \quad . \tag{2.13}$$

[4]From https://mips.as.arizona.edu/~cnaw/sun_2006.html; the procedure follows Fukugita et al. (1995), using filter curves from a variety of sources, many of which are referenced therein.

Table 2.2: Disk photometric parameters of NGC 1366.

Parameter	Value
μ_0	(19.07 ± 0.03) mag arcsec^{-2}
h	(12.81 ± 0.32) arcsec
q_d	(0.41 ± 0.01)
$\mathrm{PA_d}$	$(2.08 \pm 2.32)^\circ$

Note: values taken from Table 2 of Morelli et al. (2008).

To convert a length from arcseconds to kiloparsecs, we only need to multiply the arcsecond measurement by the system scale factor:

$$L(\mathrm{kpc}) = l(\mathrm{arcsec}) \cdot s(\mathrm{kpc\ arcsec}^{-1}) \quad . \tag{2.14}$$

The results are collected in Table 2.3.

Table 2.3: Conversion of the structural parameters of NGC 1366 from magnitudes and arcseconds to solar luminosity units and kiloparsecs.

Measured value (in "observational units")	Adopted value (in "astrophysical units")
Bulge	
$\mu_\mathrm{e} = (18.00 \pm 0.04)$ mag arcsec^{-2}	$I_\mathrm{e} = 1.632 \cdot 10^9$ L$\odot$ kpc^{-2}
$r_\mathrm{e} = (2.59 \pm 0.07)$ arcsec	$r_\mathrm{e} = 2.21 \cdot 10^{-1}$ kpc
$n = (1.50 \pm 0.03)$	$n = 1.50$
$q_\mathrm{b} = (0.80 \pm 0.01)$	$q_\mathrm{b} = 0.80$
$\mathrm{PA_b} = (5.38 \pm 2.40)^\circ$	$\mathrm{PA_b} = (5.38 \pm 2.40)^\circ$
Disk	
$\mu_0 = (19.07 \pm 0.03)$ mag arcsec^{-2}	$I_0 = 6.093 \cdot 10^8$ L$\odot$ kpc^{-2}
$h = (12.81 \pm 0.32)$ arcsec	$h = 1.096$ kpc
$q_\mathrm{d} = (0.41 \pm 0.01)$	$q_\mathrm{d} = 0.41$
$\mathrm{PA_d} = (2.08 \pm 2.32)^\circ$	$\mathrm{PA_d} = (2.08 \pm 2.32)^\circ$

2.4 Kinematic properties

Stellar and gas kinematics of NGC 1366 was measured along both the major (PA = 2°) and minor (PA = 92°) axes of NGC 1366 by Morelli et al. (2017). It was derived with a single-component and a two-component analysis, as done in Pizzella et al. (2014).

Spectra were firstly measured without separating the two counter-rotating components. Penalized PiXel Fitting (PPXF, Cappellari & Emsellem 2004) and Gas AND Absorption Line Fitting (GANDALF, Sarzi et al. 2006) IDL codes were used, with the ELODIE library of stellar spectra from Prugniel & Soubiran (2001). Furthermore, a Gaussian LOSVD was adopted to obtain the velocity curve and velocity dispersion radial profile along the observed axes. Measured velocities were subtracted of systemic velocity. No correction was applied for slit orientation and galaxy inclination, while the measured velocity dispersion was corrected for the instrumental velocity dispersion.

Figure 2.4 reports the peculiar stellar kinematics measured along the major axis of NGC 1366. The velocity curve is symmetric around the center for the innermost $|r| \leq 11$ arcsec. In addition

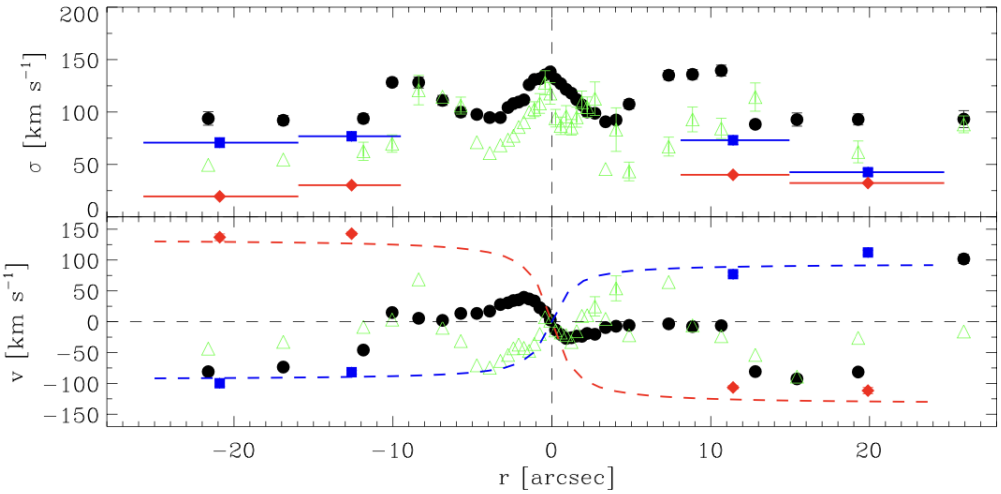

Figure 2.4: Velocity and velocity dispersion profiles along the major axis of NGC 1366 from long-slit spectroscopy. Upper panel: LOS velocity dispersion profile. Red filled diamonds [◆], blue filled squares [■] and black filled circles [●] represent the counter-rotating, corotating, and total stellar components, respectively, while green open triangles [△] represent the gaseous component. Error bars smaller than symbols are not shown. Lower panel: LOS velocity profile. The symbols and their meaning are the same as those in the upper panel. The blue [- -] and red [- -] dashed lines are a tentative indication of the velocity rotation curves for the counter-rotating and corotating component, respectively. Image taken from Morelli et al. (2017).

to the first peak located at $|r| \simeq 2$ arcsec reaching $|v| \simeq 50$ km s^{-1}, a second double peak appears at $|r| \simeq 11$ arcsec. For $6 \lesssim |r| \lesssim 11$ arcsec, $|v| \simeq 0$ km s^{-1}. Moreover, at $|r| \gtrsim 11$ arcsec, both a shift in v and a decrease in σ are measured on both sides of the galaxy. This is due to the fact that the absorption lines of the two stellar populations are so clearly separated that the PPXF-GANDALF procedure could only fit one of the components. The v measured at large negative and positive radii refer to the counter-rotating and corotating components, respectively. Focusing now on σ, as we can see from the top panel of Figure 2.4, there is a central, symmetric maximum $\sigma \simeq 150$ km s^{-1}. Then σ decreases to $\simeq 150$ km s^{-1} going outward, and increases again to $\sigma \simeq 140$ km s^{-1} at $|r| \simeq 9$ arcsec. Then, for $|r| \gtrsim 15$ arcsec, σ settles down to $\simeq 100$ km s^{-1}. Putting everything together, at $|r| \simeq 10$ arcsec a zero LOS velocity is paired with two off-center and symmetric peaks in σ of the stellar component measured along the galaxy major axis. As discussed in detail in Section 1.2, such a feature is indicative of two counter-rotating components.

On the other hand, Figure 2.5 shows the stellar kinematics measured along the minor axis of NGC 1366. No kinematic signature of stellar decoupling was found along this axis. The velocity curve is characterized by $|v| \simeq 0$ km s^{-1} at all radii. This implies that the kinematic and photometric minor axes coincide. Instead, the σ profile appeared radially symmetric, with a central peak which reaches $\sigma \simeq 150$ km s^{-1} and decreases radially in a monotonic way, setting to $\simeq 60$ km s^{-1} at $|r| \simeq 14$ arcsec.

Comparing the stellar and ionized-gas velocity curves, it appears that the gas is not associated with one of the two counter-rotating components. The gas actually rotates in the same direction as the stellar component and with a similar velocity amplitude at both small ($|r| \lesssim 1$ arcsec) and large radii ($|r| \gtrsim 11$ arcsec).

Another indication of the counter-rotating nature of NGC 1366 is shown in Figure 2.6, which

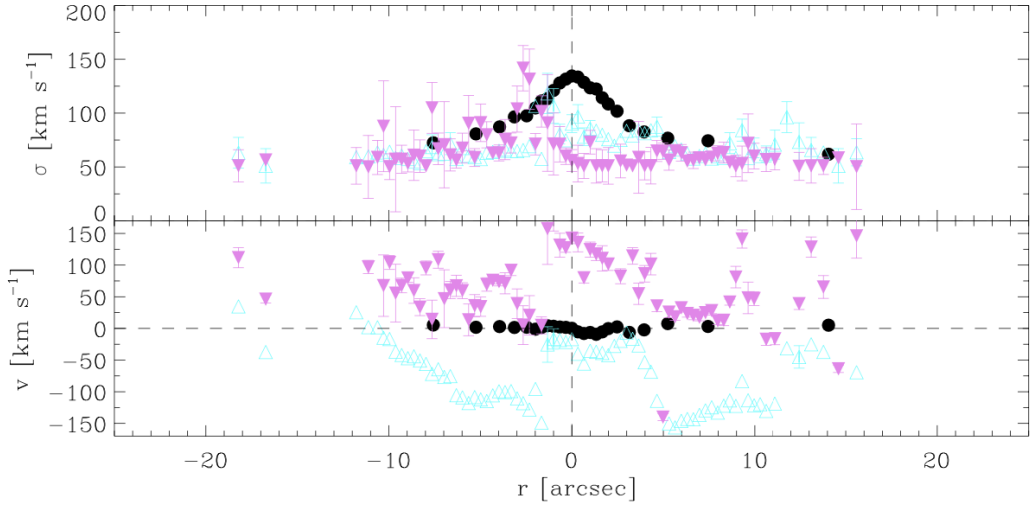

Figure 2.5: Velocity and velocity dispersion profiles along the minor axis of NGC 1366 from long-slit spectroscopy. Upper panel: LOS velocity dispersion profile. Black filled circles [●] represent the total stellar component, while violet filled triangles [▲] and cyan open triangles [△] represent the two ionized-gas components. Error bars smaller than symbols are not shown. Lower panel: LOS velocity profile. The symbols and their meaning are the same as those in the upper panel. Image taken from Morelli et al. (2017).

displays the LOS velocity, LOS velocity dispersion, h_3 and h_4 maps derived from integral-field spectroscopy. In the velocity field a distinct, inner stellar component is rotating in the opposite direction with respect to the main body of the galaxy. The velocity dispersion field reveals the characteristic 2σ feature associated with counter-rotating galaxies. Moreover, the large-scale pattern in the h_3 map is another indication of the presence of an inner, counter-rotating stellar component.

2.5 Stellar population properties

Line strength of the Lick indices were obtained by Morelli et al. (2008). Mg, Fe and Hβ line-strength indices (as defined in Faber et al. 1985 and Worthey et al. 1994) were measured from the flux-calibrated spectra following Mehlert et al. (2000). Spectra were rebinned in the dispersion direction as well as in the radial direction. The average iron index and magnesium-iron index were defined as $\langle \mathrm{Fe} \rangle = (\mathrm{Fe5270} + \mathrm{Fe5335})/2$ (Gorgas et al. 1990) and $[\mathrm{MgFe}]' = \sqrt{\mathrm{Mg}b(0.72 \times \mathrm{Fe5270} + 0.28 \times \mathrm{Fe5335})}$ (Thomas et al. 2003), respectively. In order to degrade spectra to the fixed spectral resolution of the Lick system (≈9 Å), they were convolved with a Gaussian with a proper σ. Since the seeing was the dominant effect during observations, no focus correction was applied. The errors on the indices were derived from photon statistics and CCD readout noise and calibrated using Monte Carlo simulations. The measurements were calibrated to the Lick system using the stars from Worthey et al. (1994) listed in Section 2.2.2. To address the problem of contamination of the Hβ index by the Hβ emission line, the GANDALF code was adopted to fit the galaxy spectra with synthetic population models, as done by Sarzi et al. (2006). The models were built with different templates from the stellar libraries by Bruzual & Charlot (2003) and Tremonti et al. (2004). The Salpeter initial mass function (Salpeter 1955) was adopted. Ages ranged between 1 Myr and 10 Gyr, and metallicities ranged between 1 and 2.5 $(\mathrm{Z/H})_\odot$. The spectral resolution of the stellar templates (FWHM ∼ 3 Å) was degraded to

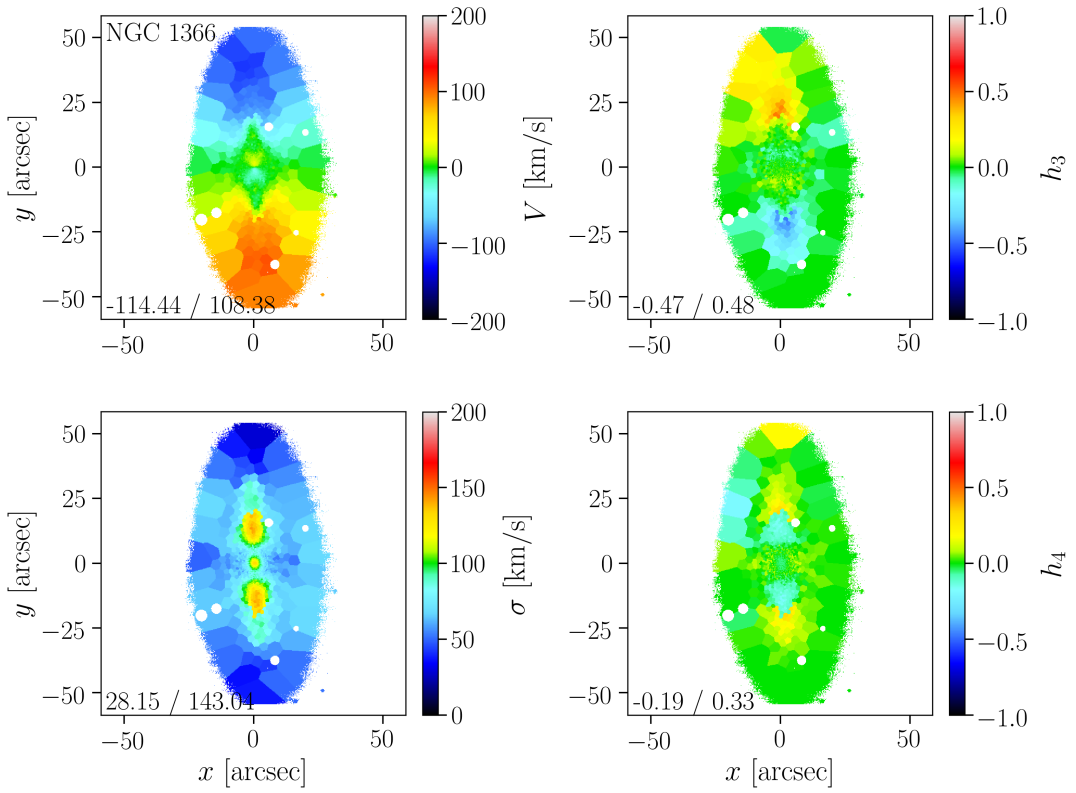

Figure 2.6: LOS velocity, LOS velocity dispersion, h_3 and h_4 maps of NGC 1366 from integral-field spectroscopy. The FOV is 1×1 arcmin^2 with north pointing up and east pointing left. Left panels (from top to bottom): LOS velocity and velocity dispersion maps. The colormaps give the velocity ranges. Right panels (from top to bottom): h_3 and h_4 maps. The colormaps give the intensity ranges. Image taken from Morelli et al. (in prep.).

match that of the spectra of NGC 1366. The observed spectra were fitted using emission lines in addition to the stellar templates. The equivalent width of Hβ emission line was ranging from $\sim$1 to $\sim$2 Å depending on the radius. The emission line was subtracted from the observed spectrum and the Hβ line-strength index was measured from the resulting Hβ absorption line. The measured values of Hβ, [MgFe]$'$, $\langle$Fe$\rangle$, Mg$_\mathrm{b}$ and Mg$_2$ for NGC 1366 are plotted in Figure 2.7. Their values are listed in Table B1 in Morelli et al. (2008).

Let us focus now on the mass-to-light ratios of the bulge $(M/L)_\mathrm{b}$ and disk $(M/L)_\mathrm{d}$. The bulge dominates the total luminosity for $|r| < 5$ arcsec (Figure 2.3), and the contribution of the disk is negligible for $|r| < 2$ arcsec. In this region, the Lick indices show minimal variation, allowing us to use the values for the bulge of NGC 1366 listed in Table 3 of Morelli et al. (2017). These values were calculated for $r < 0.3\,r_\mathrm{e} = 0.3 \times 2.59 = 0.8$ arcsec. From these values, the properties of the stellar populations (age, metallicity, α-element overabundance) were calculated using the models of Thomas et al. (2003), yielding an age of 5.1 Gyr, $[Z/\mathrm{H}] = 0.39$ dex, and $[\alpha/\mathrm{Fe}] = 0.11$ dex. Using these values, they adopted the models of Maraston (2005) for an age of 5.1 Gyr (actually 5.0 Gyr) and $[Z/\mathrm{H}] = 0.39$ dex (actually 0.35 dex) in the R-band (actually Johnson-Cousins). This gave a value for the mass-to-light ratio of $(M/L)_\mathrm{b} = 3.48\,\mathrm{M}_\odot/\mathrm{L}_\odot$.

Analyzing the disk is a bit more complex because it consists of two components with different mass-to-light ratios. To address this, we can use the diagnostics from Morelli et al. (2017). They discovered that the corotating and counter-rotating components contribute $(45 \pm 15)\%$ and $(55 \pm 15)\%$ of the stellar luminosity at all the measured radii. Then, the luminosity

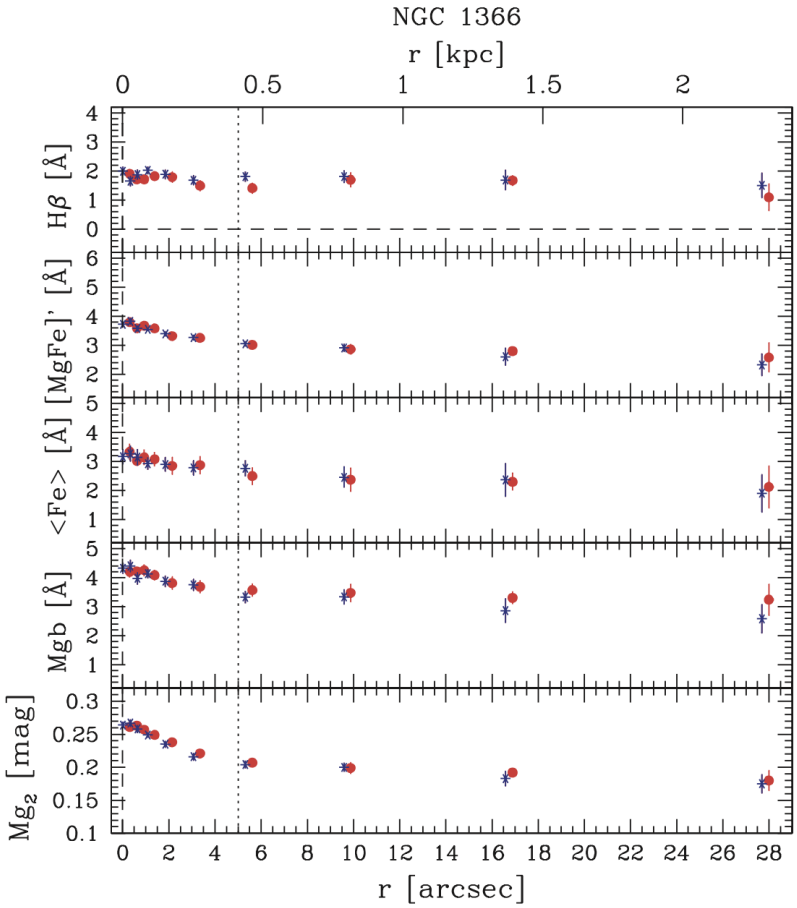

Figure 2.7: Line-strength indices of NGC 1366 measured along the major axis of the galaxy. From top to bottom: radial profiles of Hβ, [MgFe]$'$, $\langle$Fe$\rangle$, $\mathrm{Mg_b}$ and $\mathrm{Mg_2}$. As we can see, the curve is folded around the nucleus. Blue asterisks [$*$] and red dots [●] refer to the eastern and western side of the galaxy, respectively. The top panel shows the radial profile of the line-of-sight velocity (v) after the subtraction of the systemic velocity, while the bottom panel shows the velocity dispersion (σ). The vertical dashed line indicates the radius at which the surface brightness contributions of bulge and disk are the same. Image taken from Morelli et al. (2008).

fraction of each component was converted into mass fraction using the measured ages and metallicities and adopting the models by Maraston (2005). In this way, stellar mass-to-light ratios of $M/L = 3.02\,\mathrm{M_\odot/L_\odot}$ and $M/L = 1.63\,\mathrm{M_\odot/L_\odot}$ for the corotating and counter-rotating components were obtained, respectively. From these quantities, the stellar mass fractions of the corotating and counter-rotating components were found to be 60% and 40%, respectively. In Table 2.4 we report these results for summary objects.

Table 2.4: Other useful disk parameters of NGC 1366. The luminosity and mass-to-light ratios of each counter-rotating component are reported.

Parameter	Value
M/L (corotating component)	3.02 $M_\odot/L_\odot$
M/L (counter-rotating component)	1.63 $M_\odot/L_\odot$
$L/L_{\rm tot}$ (corotating component)	(0.45 ± 15)
$L/L_{\rm tot}$ (counter-rotating component)	(0.55 ± 15)
$M/M_{\rm tot}$ (corotating component)	60%
$M/M_{\rm tot}$ (counter-rotating component)	40%

Note: values taken from Morelli et al. (2008) and Morelli et al. (2017).

In our work, we treat the disk as a single entity, and we introduce the counter-rotation within the disk through the Satoh parameter (see Section 3.4.3). This means that, despite the presence of two counter-rotating disks characterized by two M/L ratios, for simplicity we consider a single M/L ratio for the entire disk. This allows us to simplify our problem without losing the physical behavior of the galaxy as a whole. Returning to the calculation of the mass-to-light ratio of the disk, we can use the total luminosity of the disk, given by Equation (A.4) (see Appendix A); then, from $L/L_{\rm tot,d}$ and $M/L_{\rm tot,d}$ for the two components, we can reconstruct the mass of each element. Then, by calculating the total mass, we can divide the disk luminosity by the disk mass, thus obtaining a mass-to-light ratio for the (fictitious, but representative) disk, which turns out to be $M/L = 2.26\,M_\odot/L_\odot$.

Finally, we can calculate the luminosities and masses of the individual components as well as the total luminosity of the galaxy.

By referring to Equation (A.5) and substituting the values provided in Table 2.3, we get:

$$L_{\rm b} = 9.16 \cdot 10^8 \quad L_\odot \qquad , \qquad L_{\rm d} = 1.88 \cdot 10^9 \quad L_\odot \qquad , \qquad L_{\rm tot} = 2.80 \cdot 10^9 \quad L_\odot \quad , \tag{2.15}$$

from which we get $L_{\rm b}/L_{\rm tot} = 0.32$.

Using the luminosities and the mass-to-light ratios, we get the mass of the individual components as well as the total stellar mass of the galaxy. Remembering that $(M/L)_{\rm b} = 3.48\ M_\odot/L_\odot$ and $(M/L)_{\rm d} = 2.26\ M_\odot/L_\odot$, we get:

$$M_{\rm b} = 3.19 \cdot 10^9 \quad M_\odot \qquad , \qquad M_{\rm d} = 4.25 \cdot 10^9 \quad M_\odot \qquad , \qquad M_{\rm tot} = 7.44 \cdot 10^9 \quad M_\odot \quad . \tag{2.16}$$

Now that we have presented and described the problem and all the data at our disposal, we proceed building the theoretical ground on which we construct our dynamical model.

Chapter 3

Dynamical model of NGC 1366

In this chapter we present the theoretical background for the construction of the dynamical model of NGC 1366. In Section 3.1 we discuss how to recover the luminosity volume density profile from the surface brightness profile for both the bulge and disk. In Section 3.2 we introduce the first and second Jeans equations (JEs), for which we adopt the solution for the axisymmetric mass distribution. In Section 3.3 we present the solution for the forces in the JEs, using the Chandrasekhar formula. In Section 3.4 we provide a solution of the first and second JEs, also presenting the Satoh decomposition method. In Section 3.5 we combine the values of the fields obtained from the JEs, weighting them both by mass and luminosity, and examining how to retrieve physical units.

3.1 Luminosity volume density

In the previous chapter we described the surface brightness distribution of the bulge and disk components of NGC 1366. Now we convert the luminosity surface density into mass volume density of each component; in particular, we find an expression for the mass volume density ρ for a spheroidal mass distribution.

We use cylindrical coordinates (R, φ, z), so that the origin corresponds to the center of the galaxy, the z coordinate lies along the symmetry axis of the system, the R coordinate lies in the equatorial plane of the galaxy, and φ is the angle formed between the intersection of the equatorial and sky planes (pointing eastward) and the projection of the vector radius onto the equatorial plane. Let us define $l = (\sqrt{R^2 + z^2/q_i^2})/r_{\rm e}$ as in Equations (2.5) and (2.10), where $i = \{\rm b,d\}$ depending on whether we consider the bulge or disk. Furthermore, let us assume that the system is seen edge on. Then, we recover the deprojected luminosity volume density j from the luminosity surface density I by the Abel integration (see Appendix B):

$$j(l) = -\frac{1}{\pi} \int_l^\infty \frac{\partial I}{\partial l'} \frac{dl'}{\sqrt{l'^2 - l^2}} \quad . \tag{3.1}$$

Since we have two different expressions for the surface brightness I of the bulge (Equation 2.5) and disk (Equation 2.10), this can be done independently for the two components. To convert the luminosity volume density j into the mass volume density ρ we assume that $\nu \propto j \propto \rho$, with ν representing the stellar number density. The proportionality constant between j and ν depends on the specific stellar population of the galaxy. We apply the mass-follows-light assumption, where the M/L for a given component is assumed to be constant throughout that component. This assumption is considered reliable, as we are assuming that each component consists of a

single stellar population. The expression for the mass volume density then becomes:

$$\rho(l) = j(l)\,\frac{M}{L} = -\frac{M}{L}\frac{1}{\pi}\int_l^\infty \frac{\partial I}{\partial l'}\frac{dl'}{\sqrt{l'^2 - l^2}} \quad . \tag{3.2}$$

This is true for each luminous component. Relying on the independence of the bulge and disk treatments, we will first consider the two components separately.

3.1.1 Bulge

The surface brightness profile of the Sérsic bulge in terms of I_0 is given by Equation (2.5). If we assume that the system is seen edge on, as in the case of NGC 1366, the isophotal flattening q coincides with the flattening of the luminosity surface density distribution, and we do not need to consider geometric corrections. From Equation (2.5) we can compute the total luminosity of the bulge by integrating I_b over the solid angle (see Appendix A). To proceed with the calculation, we normalize the expression for the luminosity surface density to $L_\mathrm{tot}/r_\mathrm{e}^2$. This simplification makes the process easier, and physical units will be restored when needed. Since $I_\mathrm{e} = I(r_\mathrm{e}) = I_0 e^{-b_n}$, we normalize and get:

$$I_\mathrm{norm,b} = \frac{r_\mathrm{e}^2}{L_\mathrm{tot}} I \overset{\text{Eqs. (A.5) and (2.5)}}{=} \frac{b_n^{2n}}{2\pi q n \Gamma(2n) e^{b_n} r_\mathrm{e}^2 I_\mathrm{e}}\, r_\mathrm{e}^2\, I_\mathrm{e} e^{b_n} e^{-b_n l^{1/n}} = \frac{b_n^{2n}}{2\pi q n \Gamma(2n)} e^{-b_n l^{1/n}} \quad , \tag{3.3}$$

and therefore:

$$\frac{\partial I_\mathrm{norm,b}}{\partial l} = -\frac{b_n^{2n+1}}{2\pi q n^2 \Gamma(2n)} l^{\frac{1-n}{n}} e^{-b_n l^{1/n}} \quad , \tag{3.4}$$

which translates into:

$$j_\mathrm{num,norm,b} \overset{\text{Eq. (3.1)}}{=} -\frac{1}{\pi}\int_l^\infty \frac{\partial I_\mathrm{norm,b}}{\partial l'}\frac{dl'}{\sqrt{l'^2 - l^2}} = \frac{b_n^{2n+1}}{2\pi^2 q n^2 \Gamma(2n)} \int_l^\infty l^{\frac{1-n}{n}} e^{-b_n l^{1/n}} \frac{dl'}{\sqrt{l'^2 - l^2}} \quad . \tag{3.5}$$

This integration has to be numerically computed and this means that it can be computationally quite expensive. To deal with this issue, we use an analytical approximation. It was proposed by Mellier & Mathez (1987) for the de Vaucoulers profile and generalized by Prugniel & Simien (1997) for a Sérsic profile and finally refined by Lima Neto et al. (1999) as it follows:

$$j_\mathrm{app,norm,b}(l, \beta, q, n) = \frac{b_n^{(3-\beta)\,n}}{4\pi q n \Gamma[(3-\beta)\,n]} l^{-\beta} \exp\left[-b_n\, l^{\frac{1}{n}}\right] \quad . \tag{3.6}$$

This formula is able to analytically reproduce the deprojected Sérsic profile with generic index n for the luminosity volume density of a spheroidal distribution. Equation (3.6) can be obtained by taking the asymptotic limit of the Abel integration of the Sérsic profile (Ciotti 1991). Of course, we get back the spherical case by substituting $q = 1$. The β index is obtained numerically, assuming that the total luminosity (or equivalently mass) is conserved. We express β as a function of n using the formula by Lima Neto et al. (1999):

$$\beta(n) = 1 - \frac{0.6097}{n} + \frac{0.05463}{n^2} \quad . \tag{3.7}$$

Multiplying $j_\mathrm{num,norm,b}$ and $j_\mathrm{app,norm,b}$ by $(M/L)_\mathrm{b}$, we recover the mass volume densities $\rho_\mathrm{num,norm,b}$ and $\rho_\mathrm{app,norm,b}$, respectively. We can compare $\rho_\mathrm{num,norm,b}$ and $\rho_\mathrm{app,norm,b}$ in Figure 3.1. The two lines are nearly superimposed for $l \gtrsim 0.1\, r_\mathrm{e}$, whereas inwards their difference increases. This is a consequence of the asymptotic limit nature of Equation (3.6). Anyway, since

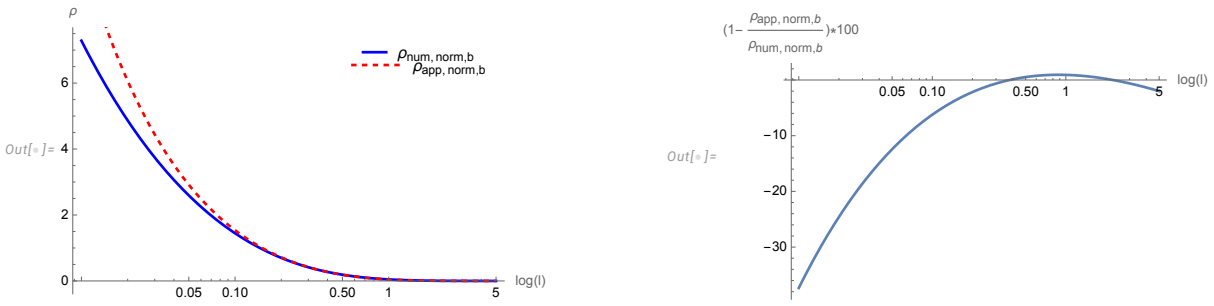

(a) (b)

Figure 3.1: Comparison between $\rho_{\mathrm{num,norm,b}}$ and $\rho_{\mathrm{app,norm,b}}$. Panel (a): agreement between $\rho_{\mathrm{num,norm,b}}$ obtained from Equation (3.5) (blue solid line [—]) and $\rho_{\mathrm{app,norm,b}}$ from Equation (3.6) (red dashed line [- -]). Along the x axis, the length is defined as in Equation (2.5), and it stands for the number of effective radii. Panel (b): percentage error of the difference between $\rho_{\mathrm{app,norm,b}}$ and $\rho_{\mathrm{num,norm,b}}$.

$0.1\,r_{\mathrm{e}}$ corresponds to some tens of pc, we can forget about this difference because it is of no importance for us. The percentage error between $\rho_{\mathrm{num,norm,b}}$ and $\rho_{\mathrm{app,norm,b}}$ is of the order of a few at large radii, and it decreases toward the inner regions for $l \lesssim 0.1\,r_{\mathrm{e}}$. Therefore, we use $j_{\mathrm{app,norm,b}}$ and $\rho_{\mathrm{app,norm,b}}$ in the subsequent calculations because they are more efficient and yield accurate results.

3.1.2 Disk

The surface brightness profile of the exponential disk in terms of I_0 is given by Equation (2.10). The total luminosity can be computed from Equation (A.4). As done for the bulge, we normalize the expression for the luminosity surface density to L_{tot}/h^2. So we can normalize obtaining:

$$I_{\mathrm{norm,d}} = \frac{h^2}{L_{\mathrm{tot}}} I \overset{\text{Eqs. (A.4) and (2.10)}}{=} \frac{b_1^2}{2\pi q h^2 I_0}\, h^2\, I_0 e^{-b_1 l} = \frac{b_1^2}{2\pi q} e^{-b_1 l} \quad , \tag{3.8}$$

and therefore:

$$\frac{\partial I_{\mathrm{norm,d}}}{\partial l} = -\frac{b_1^3}{2\pi q} e^{-b_1 l} \quad , \tag{3.9}$$

which translates into:

$$j_{\mathrm{num,norm,d}} \overset{\text{Eq. (3.1)}}{=} -\frac{1}{\pi}\int_l^\infty \frac{\partial I}{\partial l'}\frac{1}{\sqrt{l'^2 - l^2}} dl' = \frac{b_1^3}{2\pi q}\frac{1}{\pi}\int_l^\infty e^{-b_1 l'}\frac{dl'}{\sqrt{l'^2 - l^2}} \quad . \tag{3.10}$$

Now, in order to solve the Abel integral and find the expression for ρ_{d} we can follow three ways: we can compute it numerically from Equation (3.10); we can use the analytic approximate expression of Equation (3.6) with $n = 1$; or we can notice that the Abel integral of an exponential can be written in terms of a modified Bessel function of the second type. We will use the modified Bessel function approach. From Equation (3.10), doing the change of variables $l' = l\cosh(u)$ and $dl' = l\,\mathrm{senh}\,(u)\,du$, we get $l' = l \implies u = 0$ and $l' = \infty \implies u = \infty$, so it is:

$$\begin{aligned} j_{\mathrm{num,norm,d}} &= \frac{b_1^3}{2\pi^2 q}\int_0^\infty e^{-b_1 l\cosh(u)}\frac{l\,\mathrm{senh}\,(u)\,du}{l\sqrt{\cosh(u)^2 - 1}} = \\ &= \frac{b_1^3}{2\pi^2 q}\int_0^\infty e^{-b_1 l\cosh(u)} du = \frac{b_1^3}{2\pi^2 q} K_0(b_1 l) \quad ; \end{aligned} \tag{3.11}$$

in fact, $\int_0^\infty e^{-l\cosh(u)} du = K_0(l)$, where $K_0(l)$ is a modified Bessel function of the second type. The mass volume density $\rho_{\mathrm{num,norm,d}}$ is obtained multiplying Equation (3.11) by $(M/L)_{\mathrm{d}}$.

3.2 Jeans equations for an axisymmetric system

We now introduce the *Jeans equations* (JEs). For a complete overview on the topic see the books by Binney & Tremaine (1987, 2008) and Ciotti (2021) among the others. We will refer more closely to the last one for our discussion.

JEs are the set of equations derived taking the velocity moments of the *Collisionless Boltzmann Equation* (CBE). In principle JEs are represented by an infinite set of equations. However, we usually use only the zeroth and first order equations, which correspond to the first and second JE, respectively. Let us start writing the CBE for a stellar system. If we indicate with f the smooth phase-space distribution function (DF), then we can write the differential equation responsible for the evolution of the DF in the collisionless regime. In particular, we get (see Appendix C):

$$\frac{D\,f}{Dt} = \frac{\partial f}{\partial t} + \langle \vec{v}, \nabla_{\vec{x}} f \rangle - \langle \nabla_{\vec{x}} \Phi_{\text{tot}}, \nabla_{\vec{v}} f \rangle = 0 \quad . \tag{3.12}$$

where $\nabla_{\vec{x}}$ and $\nabla_{\vec{v}}$ are the gradient operators over space and velocity, respectively, $\langle \vec{a}, \vec{b} \rangle$ represents the inner product of the two vectors $\vec{a}$ and $\vec{b}$, and $\Phi_{\text{tot}} = \Phi + \Phi_{\text{ext}}$ is the total potential, with:

$$\Phi(\vec{x}, t) = -G \int_{\mathbb{R}^3} \frac{\rho(\vec{y}, t)}{\|x - y\|} d^3\vec{y} \quad , \tag{3.13}$$

$$\Phi_{\text{ext}}(\vec{x}, t) = -G \int_{\mathbb{R}^3} \frac{\rho_{\text{ext}}(\vec{y}, t)}{\|x - y\|} d^3\vec{y} \quad . \tag{3.14}$$

As an example, ρ could be the stellar mass volume density of a component of the galaxy, and ρ_{ext} can be the mass volume density of some other component such as a dark matter (DM) halo, or a gaseous component, or a central black hole. Equation (3.12) is very important for stellar dynamics, but it is not the one we are looking for. In fact, we need an equation, which explicitly depends on the observables of the system (e.g., velocity, velocity dispersion, number density of stars) in order to directly insert these quantities inside our equations and solve them. While the CBE is defined over the 6D phase space, the JE are defined over the 3D configuration space, and this allows us to create a more intuitive model based on observable quantities. First of all, we define some quantities that will be useful for our purposes. We consider a stellar system characterized by a phase-space DF which depends on position, velocity, and time, which we define as $f(\vec{x}, \vec{v}, t)$. Then, we introduce a microscopic function $F = F(\vec{x}, \vec{v}, t)$. Clearly, F can be whatsoever physical quantity expressed by some mathematical expression (e.g., position, velocity, kinetic energy). Let $\nu(\vec{x,t})$ be the number density of our stellar system at position $\vec{x}$ and at a time t. It is $\nu(\vec{x,t}) = \int_{\mathbb{R}^3} f(\vec{x}, \vec{v}, t) d^3\vec{v}$. As said before, for the mass-follows-light assumption we adopt $\rho = (M/L)\, j = \alpha\, \nu$, where α is a constant which depends on the stellar population. Then, we associate to F a macroscopic function $\overline{F}$:

$$\overline{F}(\vec{x}, t) \coloneqq \frac{1}{\nu(\vec{x}, t)} \int_{\mathbb{R}^3} F(\vec{x}, \vec{v}, t) f(\vec{x}, \vec{v}, t) d^3\vec{v} \quad . \tag{3.15}$$

For what concerns the JEs, F is chosen so that we get the *velocity moments*:

$$\overline{v_i}(\vec{x}, t) \coloneqq \frac{1}{\nu(\vec{x}, t)} \int_{\mathbb{R}^3} v_i f d^3\vec{v} \quad , \tag{3.16}$$

$$\overline{v_i v_j}(\vec{x}, t) \coloneqq \frac{1}{\nu(\vec{x}, t)} \int_{\mathbb{R}^3} v_i v_j f d^3\vec{v} \quad , \tag{3.17}$$

$$\sigma^2_{ij}(\vec{x}, t) = \sigma^2_{ji}(\vec{x}, t) \coloneqq \frac{1}{\nu(\vec{x,t})} \int_{\mathbb{R}^3} (v_i - \overline{v_i})(v_j - \overline{v_j}) f d^3\vec{v} = \overline{v_i v_j} - \overline{v_i}\,\overline{v_j} \quad . \tag{3.18}$$

We can demonstrate (see Appendix E) that the general differential equations to which F obeys is:

$$\frac{\partial\,\nu\overline{F}}{\partial t}+\frac{\partial\,\nu\overline{Fv_i}}{\partial x_i}=-\nu\frac{\partial\Phi_{\rm tot}}{\partial x_i}\overline{\frac{\partial\,F}{\partial v_i}}+\nu\,\overline{v_i\frac{\partial\,F}{\partial x_i}}+\nu\overline{\frac{\partial\,F}{\partial t}}\quad . \tag{3.19}$$

We then obtain the first and second JEs by putting firstly $F=1$ and then $F=v_j$ (Appendix E); therefore:

$$F=1\implies\qquad\text{First JE}\qquad\qquad\frac{\partial\,\nu}{\partial t}+\frac{\partial\,\nu\,\overline{v_i}}{\partial x_i}=\frac{D\,\nu}{Dt}+\nu\frac{\partial\overline{v_i}}{x_i}=0\quad , \tag{3.20}$$

$$F=v_j\implies\qquad\text{Second JE}\qquad\frac{\partial\,\nu\,\overline{v_j}}{\partial t}+\frac{\partial\,\nu\,\overline{v_jv_i}}{\partial x_i}=-\nu\overline{\frac{\partial\,v_j}{\partial t}}\quad(i=1,2,3)\quad . \tag{3.21}$$

Often the second JE is found in a different form. If we subtract Equation (3.20) multiplied by $\overline{v_j}$ from Equation (3.21) we find (Appendix E):

$$\text{Second JE}\qquad\frac{D\,\overline{v_i}}{Dt}=\frac{\partial\,\overline{v_i}}{\partial t}+\overline{v_j}\frac{\partial\,\overline{v_i}}{\partial x_j}=-\frac{\partial\,\Phi_{\rm tot}}{\partial x_i}-\frac{1}{\nu}\frac{\partial\,\nu\sigma_{ij}^2}{\partial x_j}\quad(i=1,2,3)\quad . \tag{3.22}$$

We now solve the previous equation in the case of an axisymmetric system. Let us introduce two integrals of motion that will be useful for our purposes. To do so, we can define a new gravitational potential, called *relative potential*:

$$\psi=-\Phi+\Phi_0\qquad,\qquad\text{where}\quad\Phi_0=const\quad, \tag{3.23}$$

and a new energy, called *relative energy*:

$$\mathcal{E}=-E+\Phi_0=-\frac{1}{2}\|v\|^2-\Phi+\Phi_0=-\frac{1}{2}\|v\|^2+\psi\quad . \tag{3.24}$$

Let $\vec{J}$ be the specific angular momentum of each star, which can be decomposed into its three components: J_x, J_y and J_z. We now consider an axysimmetric stellar system and cylindrical coordinates (R,φ,z). We study the case of a DF depending on the two classical integrals of motion related to the assumed symmetry. In fact, from the Jeans theorem, a DF is a steady state solution of the CBE if and only if is a function of integrals of motions (see Appendix D for the demonstration). We write $I_1\coloneqq\mathcal{E}$ and $I_2\coloneqq J_z$, so that our DF is in the form $f=f(\mathcal{E},J_z)$. This implies that the vertical velocity dispersion is equal to the vertical velocity dispersion, $\sigma_R^2=\sigma_z^2$ (isotropy), and so the velocity dispersion ellipsoid is rotationally symmetric in the plane (R,z) (meridional plane). Furthermore, we express the steady state JEs in cylindrical form (see Appendix F), so that:

$$\begin{cases}\frac{\partial}{\partial z}(\rho\sigma_z^2)=-\rho\frac{\partial\Phi_{\rm tot}}{\partial z}\\ \frac{\partial}{\partial R}(\rho\sigma_z^2)-\rho\frac{\Delta_\sigma}{R}=-\rho\frac{\partial\Phi_{\rm tot}}{\partial R}\quad ,\end{cases} \tag{3.25}$$

where Δ_σ is the difference between the mean square azimuthal velocity and square vertical velocity dispersion, $\Delta_\sigma\coloneqq\overline{v_\varphi^2}-\sigma_z^2=\overline{v_\varphi}^2+\sigma_\varphi^2-\sigma_z^2$. If we assign ρ and $\Phi_{\rm tot}$, we obtain the general solution of this system by integrating the first equation in z at fixed R:

$$\rho\sigma_z^2=\int_z^{z_t(R)}\rho\frac{\partial\Phi_{\rm tot}}{\partial z'}dz' \tag{3.26}$$

Moreover, substituting Equation (3.26) inside the second of Equation (3.25) and integrating by parts, we get:

$$
\begin{aligned}
\rho\frac{\Delta_\sigma}{R} &= \rho\frac{\partial\Phi_{\text{tot}}}{\partial R} + \frac{\partial}{\partial R}(\rho\sigma_z^2) = \\
&= \rho\frac{\partial\Phi_{\text{tot}}}{\partial R} + \frac{\partial}{\partial R}\int_z^{z_t(R)} \rho\frac{\partial\Phi_{\text{tot}}}{\partial z'}dz' = \\
&= \rho\frac{\partial\Phi_{\text{tot}}}{\partial R} + \int_z^{z_t(R)} \frac{\partial\rho}{\partial R}\frac{\partial\Phi_{\text{tot}}}{\partial z'}dz' + \int_z^{z_t(R)} \rho\frac{\partial^2\Phi_{\text{tot}}}{\partial R\,\partial z'}dz' = \\
&= \rho\frac{\partial\Phi_{\text{tot}}}{\partial R} + \int_z^{z_t(R)} \frac{\partial\rho}{\partial R}\frac{\partial\Phi_{\text{tot}}}{\partial z'}dz' + \left[\rho\frac{\partial\Phi_{\text{tot}}}{\partial R}\right]_z^{z_t(R)} - \int_z^{z_t(R)} \frac{\partial\rho}{\partial z'}\frac{\partial\Phi_{\text{tot}}}{\partial R}dz' = \\
&= \rho(z,R)\frac{\partial\Phi_{\text{tot}}(z,R)}{\partial R} + \rho(z_t(R),R)\frac{\partial\Phi_{\text{tot}}(z_t(R),R)}{\partial R} - \\
&\qquad - \rho(z,R)\frac{\partial\Phi_{\text{tot}}(z,R)}{\partial R} + \int_z^{z_t(R)} \left[\frac{\partial\rho}{\partial R}\frac{\partial\Phi_{\text{tot}}}{\partial z'} - \frac{\partial\rho}{\partial z'}\frac{\partial\Phi_{\text{tot}}}{\partial R}\right]dz' = \\
&= \rho(z_t(R),R)\frac{\partial\Phi_{\text{tot}}(z_t(R),R)}{\partial R} + \int_z^{z_t(R)} \left[\frac{\partial\rho}{\partial R}\frac{\partial\Phi_{\text{tot}}}{\partial z'} - \frac{\partial\rho}{\partial z'}\frac{\partial\Phi_{\text{tot}}}{\partial R}\right]dz' \quad . \qquad (3.27)
\end{aligned}
$$

3.3 Solution of the Jeans equations: forces and the Chandrasekhar formula

To solve the JEs, it is necessary to obtain an expression for the radial and vertical derivatives of the potential $\frac{\partial\Phi_{\text{tot}}}{\partial R}$ and $\frac{\partial\Phi_{\text{tot}}}{\partial z}$, respectively, which are also called *forces*. In general, for a disk galaxy there are three gravitational potentials (and consequently six forces) that we need to calculate:

- the force given by the gravitational potential of the *bulge*;
- the force given by the gravitational potential of the *disk*;
- the force given by the gravitational potential of the *DM halo*.

The first two potentials are homogeneous spheroidal potentials. This implies that we can avoid to go through the tedious calculation of elliptical integrals. In these cases, we directly apply the Chandrasekhar formula without the need for computing numerical derivatives. This approach allows us to work with integrals, which are more precise. On the other hand, the DM halo cannot always be reproduced by an homogeneous ellipsoid: it depends on the functional form with which we express the DM halo mass volume density. If this is not possible, in order to solve the JEs we have to compute numerical derivatives. Anyway, in our numerical code we would have no difficulty at all to add and implement another component to our system, as for example a super massive black hole residing in the center of the galaxy.

3.3.1 Bulge and disk

The Chadrasekhar formula gives us the gravitational field produced at $\vec{x}$ by a stellar mass density distribution described by an homogeneous ellipsoid. Following Ciotti (2021), we consider an

ellipsoid with semimajor axes a_1, a_2 and a_3, and we can define, adopting ellipsoidal coordinates:

$$\Delta(\tau) \coloneqq (a_1^2+\tau)(a_2^2+\tau)(a_3^2+\tau) \quad , \tag{3.28}$$

$$m_\tau^2(\vec{x},\tau) \coloneqq \sum_{i=1}^{3} \frac{x_i^2}{a_i^2+\tau} \quad . \tag{3.29}$$

From Equation (2.72) in Ciotti (2021) we get:

$$g_i(\vec{x}) = -\frac{\partial\Phi}{\partial x_j} = -2\pi G a_1 a_2 a_3 x_i \int_0^\infty \frac{\rho(m_\tau)}{(a_i^2+\tau)\sqrt{\Delta(\tau)}} d\tau \quad . \tag{3.30}$$

In our case, since we work in cylindrical coordinates (R,φ,z), we have $a_1 = a_2 = a_R = 1$ and $a_3 = a_z = q$. Therefore, after normalizing ($G = 1$), we obtain:

$$\frac{\partial\Phi}{\partial R}(R,z,q,n) = 2\pi q R \int_0^\infty \frac{\rho(m_\tau,q,n)}{(1+\tau)^2\sqrt{q^2+\tau}} d\tau = \begin{cases} 2\pi q_\mathrm{b} R \int_0^\infty \frac{\rho(m_{\tau,\mathrm{b}},q_\mathrm{b},n_\mathrm{b})}{(1+\tau)^2\sqrt{q_\mathrm{b}^2+\tau}} d\tau & \text{for the bulge} \\ 2\pi q_\mathrm{d} R \int_0^\infty \frac{\rho(m_{\tau,\mathrm{d}},q_\mathrm{d},n_\mathrm{d})}{(1+\tau)^2\sqrt{q_\mathrm{d}^2+\tau}} d\tau & \text{for the disk} \end{cases} , \tag{3.31}$$

and analogously:

$$\frac{\partial\Phi}{\partial z}(R,z,q,n) = 2\pi q z \int_0^\infty \frac{\rho(m_\tau,q,n)}{(1+\tau)(q^2+\tau)^{\frac{3}{2}}} d\tau = \begin{cases} 2\pi q_\mathrm{b} z \int_0^\infty \frac{\rho(m_{\tau,\mathrm{b}},q_\mathrm{b},n_\mathrm{b})}{(1+\tau)(q_\mathrm{b}^2+\tau)^{\frac{3}{2}}} d\tau & \text{for the bulge} \\ 2\pi q_\mathrm{d} z \int_0^\infty \frac{\rho(m_{\tau,\mathrm{d}},q_\mathrm{d},n_\mathrm{d})}{(1+\tau)(q_\mathrm{d}^2+\tau)^{\frac{3}{2}}} d\tau & \text{for the disk} \end{cases} . \tag{3.32}$$

These formulas will be used in the solution of the JEs for both the bulge and disk.

3.3.2 Dark matter halo

The expressions for the forces in the case of the DM halo component depend on how the halo mass distribution is expressed. We list below some choices that can be made:

- *Spherical DM halo.* In this case we use the Chandrasekhar formulas described in Section 3.3.1. An example is the Navarro–Frenk–White profile (Navarro et al. 1996):

$$\Phi_\mathrm{NFW}(r) = -\frac{4\pi G\rho_0 R_\mathrm{s}^3}{r} \ln\left(1+\frac{r}{R_\mathrm{s}}\right) \quad , \tag{3.33}$$

  where ρ_0 is the characteristic density, R_s is the scale radius, and r the radial distance from the center of the halo.

- *Ellipsoidal DM halo.* The procedure is analogous to that described in Section 3.3.1.

- *Binney logarithmic DM halo.* This has the form (Binney 1981):

$$\Phi_\mathrm{B}(R,z) = \frac{1}{2}v_0^2 \ln\left(r_\mathrm{c}^2 + R^2 + \frac{z^2}{q^2}\right) \quad , \tag{3.34}$$

  where v_0 is the asymptotic circular velocity, r_c is the core radius, q is the flattening of the halo and R and z are the canonical cylindrical coordinates. The advantage of this potential is that it is pretty easy to be treated, because its derivatives can be carried out analytically.

- *Other more complex DM potentials.* If the potentials are more complex, we have to compute their numerical derivatives. This makes the numerical code much more computationally expensive.

Mazzei et al. (2019) exploited smooth particle hydrodynamic simulations to explore galaxy evolution in low density environments for 11 early-type galaxies, including NGC 1366. Starting from a large grid of simulations of galaxy encounters and mergers, they were able to single out the simulations matching the global properties of the targets. The initial parameters of each simulation were tuned as described in Mazzei et al. (2014b,a, 2018). The initial total mass for the NGC 1366 simulation was set at $110 \cdot 10^{10}$ $M_\odot$, with a mass ratio of $10:1$ between the DM + gas halo and the rest of the system. Additionally, the gas fraction of the halo was set to be $f_{\rm gas} = 0.1$.

3.4 Solution of the Jeans equations: fields

Once we see how to treat the partial derivatives of the potential in the various cases and after obtaining the expressions for the forces in the case of an homogeneous ellipsoid, we continue with the solution of the JEs.

3.4.1 Solution of the first Jeans equation

In order to solve the first JE in the case of a homogeneous ellipsoidal system (i.e. bulge, disk, ellipsoidal or spherical DM halo), we use the solution of the first JE for an axysimmetric system in cylindrical coordinates, as given in Equation (3.26). If we consider $z_t(R) \to \infty$ since we want to examine the whole space, and express the term $\frac{\partial \Phi_{\rm tot}}{\partial z'}$ with the Chandrasekhar formula in Equation (3.32), we get:

$$\rho\sigma_z^2(R,z,q,n) = 2\pi q \int_0^\infty \int_z^\infty z'\,\rho(m,q,n)\frac{\rho(m_\tau,q,n)}{(1+\tau)(q^2+\tau)^{\frac{3}{2}}}\,d\tau dz' \quad , \tag{3.35}$$

from which, inverting, we obtain the vertical component of the velocity variance:

$$\sigma_z^2(R,z,q,n) = \frac{1}{\rho(m,q,n)} 2\pi q \int_0^\infty \int_z^\infty z'\,\rho(m,q,n)\frac{\rho(m_\tau,q,n)}{(1+\tau)(q^2+\tau)^{\frac{3}{2}}}\,d\tau dz' \quad . \tag{3.36}$$

3.4.2 Solution of the second Jeans equation

We now analyze the solution of the second JE in the case of a homogeneous ellipsoidal system (bulge, disk, ellipsoidal or spherical halo) for an axisymmetric system in cylindrical coordinates, given in Equation (3.27):

$$\begin{aligned}\rho\frac{\Delta_\sigma}{R} &= \rho\frac{\partial\Phi_{\rm tot}}{\partial R} + \frac{\partial}{\partial R}(\rho\sigma_z^2) = \\ &= \underbrace{\cancel{\rho(z_t(R),R)}\frac{\partial\Phi_{\rm tot}(\cancel{z_t(R),R})}{\partial R}}_{\text{well behaved system}} + \int_z^{z_t(R)}\left[\frac{\partial\rho}{\partial R}\frac{\partial\Phi_{\rm tot}}{\partial z'} - \frac{\partial\rho}{\partial z'}\frac{\partial\Phi_{\rm tot}}{\partial R}\right]dz' \quad .\end{aligned}$$

For a system with a mass volume density vanishing or truncated at the boundary (namely a "well behaved system"), the first term in the right hand side of the last line in the previous expression can be taken to be null. This leaves only the commutator. Since the commutator and radial derivative expressions are analogous, we can either use one or other. For the derivatives of the potential, we use the two Chandrasekhar formulas given in Equations (3.31) and (3.32).

3.4.3 Satoh decomposition

The second JE gives us an expression for $\Delta_\sigma = \overline{v_\varphi^2} - \sigma_z^2 = \overline{v_\varphi}^2 + \sigma_\varphi^2 - \sigma_z^2$. This variable contains the information about both square mean azimuthal velocity and azimuthal velocity dispersion. Therefore, we need a method to break the degeneracy between ordered and random motions along the azimuthal direction. To do so we use the *Satoh decomposition*. In fact, when $\Delta_\sigma \geq 0$ everywhere, we can relate the mean azimuthal velocity $\overline{v_\varphi}$ with Δ_σ using the empirical law by Satoh (1980):

$$\overline{v}_\varphi = k\sqrt{\Delta_\sigma} \qquad |k| \leq 1 \quad , \tag{3.37}$$

where k is a free parameter. From the definition of $\sigma_\varphi^2 = \overline{v_\varphi^2} - \overline{v_\varphi}^2$ and $\Delta_\sigma = \overline{v_\varphi^2} - \sigma_z^2$ we obtain the expression of the azimuthal velocity dispersion:

$$\sigma_\varphi^2 = \overline{v_\varphi^2} - \overline{v_\varphi}^2 = \Delta_\sigma + \sigma_z^2 - k^2\Delta_\sigma = (1-k^2)\Delta_\sigma + \sigma_z^2 = (1-k^2)\overline{v_\varphi^2} + k^2\sigma_z^2 \quad . \tag{3.38}$$

If $k^2 = 1$ we have an isotropic rotator ($\sigma_\varphi = \sigma_z = \sigma_R$), with flattening totally supported by rotation; instead, if $k = 0$, there is no net rotation ($v_\varphi = 0$), and the flattening is totally supported by azimuthal velocity anisotropy. The Satoh parameter k can also vary with R and z. In this case we talk about *generalized Satoh decomposition* $k(R, z)$ (Ciotti & Pellegrini 1996). The Satoh parameter k can be used to introduce counter-rotation within the galaxy. Counter-rotation can be treated even without summoning the generalized expression of the Satoh decomposition. In fact, in the case of $k = const$ in a multi-component system, counter-rotation can be introduced by assigning to each component a specific value of k. If we do that properly, we obtain a counter-streaming star motion. Anyway, the phenomenon of counter-rotation can be an intrinsic property of one component. For example, a disk can corotate until a certain radius, and then after that radius there could be an inversion of the stellar motion. This transition can be either smooth or rapid, or even more complicated. This case has to be treated with the generalized Satoh decomposition, making k to vary with the distance from the galactic center. This was performed for example in Negri et al. (2014), using the Jeans AxiSymmetric Models of galaxies IN Equilibrium code (JASMINE, Posacki et al. 2013), and in Caravita et al. (2021), using the Jeans AxiSymmetric Models of galaxies IN Equilibrium 2 code (JASMINE2, Caravita et al. 2021).

Moreover, the radial and vertical velocity dispersions σ_R and σ_z, which are equal by assumption, are independent from k. This implies that the only way to change those values is to modify the DM halo surrounding the galaxy.

In our code we analyze the following cases:

1. - non-rotating bulge ($k_\mathrm{b} = 0$);
   - non-rotating disk ($k_\mathrm{d} = 0$).

   in this case no component is rotating. We will refer to this as the *non-rotating galaxy model*.

2. - non-rotating bulge ($k_\mathrm{b} = 0$);
   - isotropic rotating disk ($k_\mathrm{d} = 1$).

   in this case we do not have counter-rotation. We will refer to this as the *non-rotating bulge model*.

3. - isotropic-counter-rotator bulge ($k_\mathrm{b} = -1$);
   - isotropic rotating disk ($k_\mathrm{d} = 1$).

   in this case we do have counter-rotation, but we are not considering the generalized Satoh decomposition. We will refer to this as the *maximally counter-rotating model*.

4.
   - $k_{\rm b} = -1/2$;
   - $k_{\rm d} = 1/2$.

   in this case we do have counter-rotation too, but we are not considering the generalized Satoh decomposition. We will refer to this as the *mildly counter-rotating model*.

5.
   - $k_{\rm b} = -3/4$;
   - $k_{\rm d} = 3/4$.

   in this case we do have counter-rotation too, but we are not considering the generalized Satoh decomposition. We will refer to this as the *moderately counter-rotating model*.

3.5 Dynamical and observed fields

In the previous sections we explored how to solve the JEs by determining the fields that characterize each component of the galaxy. We now aim to combine these fields in an appropriate way. We cannot simply average the fields of the two components, since each component is characterized by a different luminosity (or mass) volume density, which means that their contributions should be weighted accordingly. Therefore, we need to weight the fields (σ_z, $\overline{v_\varphi^2}$, $\overline{v_\varphi}$) of each component by its actual contribution. Two types of weights can be identified:

- *mass weight*. This weight corresponds to the dynamical field, which is involved in the dynamics of the system. In this case, we multiply each field by the mass volume density ρ of each component.
- *luminosity weight*. This weight corresponds to the field that we observe directly. In this case, we multiply each field by the luminosity volume density $j = \frac{\rho}{M/L}$ of each component.

In full generality, we consider models composed of N different stellar density distributions $\rho_{\star,i}(R,z)$ of mass $M_{\star,i}$ (Caravita et al. 2021). Then, indicating with $\sum_i$ the sums over the N stellar components, the total stellar density $\rho_\star$ and the total stellar mass $M_\star$ of the system are given respectively by:

$$\rho_\star = \sum_i \rho_{\star,i} \quad , \quad M_\star = \sum_i M_{\star,i} \quad . \tag{3.39}$$

3.5.1 Mass-weighted (dynamical) fields

With the help of the previously introduced concepts, we define the dynamical fields as (Caravita et al. 2021):

$$\begin{aligned} \sigma_{z\ ,\rm mw}^2 &= \frac{\sum_i \rho_{\star,i}\, \sigma_{{\rm z},i}^2}{\rho_\star} \quad , \quad \sigma_{\rm dyn}^2 = \frac{\sum_i \rho_{\star,i}\, \sigma_i^2}{\rho_\star} \quad , \quad \overline{v_\varphi^2}_{\ ,\rm mw} = \frac{\sum_i \rho_{\star,i}\, \overline{v_{\varphi,i}^2}}{\rho_\star} \\ \overline{v_\varphi}_{\ ,\rm mw} &= \frac{\sum_i \rho_{\star,i}\, \overline{v_\varphi}_{,i}}{\rho_\star} \quad , \quad \Delta_{\sigma\ ,\rm mw} = \frac{\sum_i \rho_{\star,i}\, \Delta_{\sigma,i}}{\rho_\star} \quad . \end{aligned} \tag{3.40}$$

Things work differently for σ_φ^2. Specifically, we cannot simply compute the weighted average of $\sigma_{\varphi,i}^2$ because, as seen from Equation (3.38), σ_φ^2 is derived from a combination of $\overline{v_\varphi^2}$ and $\overline{v_\varphi}^2$. Therefore, we have ($\sigma_{\varphi,i}^2 = \overline{v_{\varphi,i}^2} - \overline{v_\varphi}_{,i}^2$):

$$\sigma_{\varphi,\rm mw}^2 = \overline{v_\varphi^2}_{\ ,\rm mw} - \overline{v_\varphi}_{\ ,\rm mw}^2 \overset{\text{Eq. (3.42)}}{=} \frac{\sum_i \rho_{\star,i}\, \overline{v_{\varphi,i}^2}}{\sum_i \rho_{\star,i}} - \overline{v_\varphi}_{\ ,\rm mw}^2 = \frac{\sum_i \rho_{\star,i}\, (\sigma_{\varphi,i}^2 + \overline{v_\varphi}_{,i}^2)}{\rho_\star} - \overline{v_\varphi}_{\ ,\rm mw}^2 \quad . \tag{3.41}$$

3.5.2 Luminosity-weighted (observed) fields

Analogously, we define the observed fields as:

$$\sigma_z^2{}_{,\mathrm{lw}} = \frac{\sum_i \frac{\rho_{\star,i}}{M/L|_i}\,\sigma^2_{\mathrm{z},i}}{\sum_i \frac{\rho_{\star,i}}{M/L|_i}} \quad , \quad \sigma^2_{\mathrm{obs}} = \frac{\sum_i \frac{\rho_{\star,i}}{M/L|_i}\,\sigma^2_i}{\sum_i \frac{\rho_{\star,i}}{M/L|_i}} \quad , \quad \overline{v^2_\varphi}_{,\mathrm{lw}} = \frac{\sum_i \frac{\rho_{\star,i}}{M/L|_i}\,\overline{v^2_\varphi}_{,i}}{\sum_i \frac{\rho_{\star,i}}{M/L|_i}}$$
$$\overline{v_\varphi}_{,\mathrm{lw}} = \frac{\sum_i \frac{\rho_{\star,i}}{M/L|_i}\,\overline{v_\varphi}_{,i}}{\sum_i \frac{\rho_{\star,i}}{M/L|_i}} \quad , \quad \Delta_{\sigma\,,\mathrm{lw}} = \frac{\sum_i \frac{\rho_{\star,i}}{M/L|_i}\,\Delta_{\sigma,i}}{\sum_i \frac{\rho_{\star,i}}{M/L|_i}} \quad , \tag{3.42}$$

and:

$$\sigma^2_{\varphi,\mathrm{lw}} = \frac{\sum_i \frac{\rho_{\star,i}}{M/L|_i}\,(\sigma^2_{\varphi,i} + \overline{v_\varphi}^2_{,i})}{\sum_i \frac{\rho_{\star,i}}{M/L|_i}} - \overline{v_\varphi}^2_{,\mathrm{lw}} \quad . \tag{3.43}$$

3.5.3 Conversion to astrophysical units

In order to go back to astrophysical units we have to multiply the results by the proper combination of the scale values contained in Table 2.3. In particular we have:

$$\begin{aligned}
\text{density} \implies \rho_{\mathrm{phys}} &= \rho\,\frac{L_{\mathrm{tot}}}{r_{\mathrm{e}}^3} && \frac{\mathrm{M}_\odot}{\mathrm{kpc}^3} \quad , \\
\text{velocity dispersion} \implies \sigma^2_{z,\,\mathrm{phys}} &= \sigma_z^2\,\frac{G\,L_{\mathrm{tot}}}{r_{\mathrm{e}}} && (\mathrm{km/s})^2 \quad , \\
\implies \sigma^2_{\varphi,\,\mathrm{phys}} &= \sigma_\varphi^2\,\frac{G\,L_{\mathrm{tot}}}{r_{\mathrm{e}}} && (\mathrm{km/s})^2 \quad , \\
\implies \sigma^2_{\mathrm{phys}} &= \sigma^2\,\frac{G\,L_{\mathrm{tot}}}{r_{\mathrm{e}}} && (\mathrm{km/s})^2 \quad , \\
\text{mean square velocity} \implies \overline{v^2_{\varphi,\,\mathrm{phys}}} &= \overline{v^2_\varphi}\,\frac{G\,L_{\mathrm{tot}}}{r_{\mathrm{e}}} && (\mathrm{km/s})^2 \quad , \\
\text{velocity} \implies \overline{v_{\varphi,\,\mathrm{phys}}} &= \overline{v_\varphi}\,\sqrt{\frac{G\,L_{\mathrm{tot}}}{r_{\mathrm{e}}}} && \mathrm{km/s} \quad ,
\end{aligned} \tag{3.44}$$

where the gravitational constant is expressed in astrophysical units as $G = 4.301\ 10^{-3}$ km^2 pc M$_\odot^{-1}$ s^{-2}.

Chapter 4

Analysis and results for NGC 1366

In this chapter we present and describe the numerical code used to model NGC 1366 and its results. In Section 4.1 we present the software used in our code and our initial assumptions. In Section 4.2 we reproduce the luminosity surface density of the galaxy. In Section 4.3 we solve the first JE, obtaining σ_z. In Section 4.4 we solve the second JE, obtaining $\sqrt{\Delta_\sigma}$ and $\sqrt{\overline{v_\varphi^2}}$. Then, we obtain $\overline{v_\varphi}$ and σ_φ for five pairs of the Satoh parameters. In Section 4.5 we compare models and integral-field spectroscopic observations. In Section 4.6 we compare models and long-slit spectroscopic observations.

4.1 Numerical code and initial assumption

In this thesis we use `Wolfram Mathematica`[1] for the implementation of the numerical calculations. We choose this program among the others because of its versatile environment. Complex mathematical models can be efficiently implemented, allowing for both analytical and numerical approaches. Additionally, `Mathematica` produces high-quality plots, which are essential for presenting our results.

Regarding the numerical code, we consider NGC 1366 as a multicomponent system composed of a bulge, described by Equation (2.5), and a disk, described by Equation (2.10). In principle, incorporating a DM halo poses no issues. However, we opt not to include it in this analysis, as we want to begin with a more simplified model. Therefore, in the following the total mass volume density of the galaxy is given by:

$$\rho_{\rm tot} \coloneqq \rho_{\rm b} + \rho_{\rm d} \quad . \tag{4.1}$$

4.2 Luminosity surface density

Before solving the JEs, we reproduce the luminosity surface density of the galaxy to double check if the photometric decomposition and conversion procedure from observational to astrophysiclal units have been performed correctly. To do this, we find the luminosity volume density of each component, sum them, project the sum along the LOS, go back to the observational units, and finally compare the result with the observations. The luminosity volume density of the bulge is given by Equation (3.6) multiplied by the M/L of the bulge, while the luminosity volume density

[1] `Wolfram Mathematica` is a software system with built-in libraries for several areas of technical computing that allow machine learning, statistics, symbolic computation, data manipulation, network analysis, time series analysis, NLP, optimization, plotting functions and various types of data, implementation of algorithms, creation of user interfaces, and interfacing with programs written in other programming languages.

of the disk is given by Equation (3.11) multiplied by the M/L of the disk. To check if this has been done properly, we compare the values of the mass obtained from the luminosity from the 2D integration of the surface-brightness radial profile with the 3D integration of the luminosity volume density of each component. This value has to be multiplied by the corresponding value of M/L for bulge and disk to reproduce the effective mass of the component. Therefore, we get:

$$M_i(\text{from 2D integration}) = \int_0^{4\pi} I_i \, d\Omega \, (M/L)_i = \frac{2\pi q_i n_i}{b_{n_i}^{2n_i}} \Gamma(2n_i) I_{\mathrm{e},i} r_{\mathrm{e},i}^2 \, (M/L)_i \quad ,$$
$$M_i(\text{from 3D integration}) = \int_0^{\infty} \int_0^{\infty} 4\pi R \, \rho_{\mathrm{i}} \, dR \, dz \, (M/L)_i \quad , \tag{4.2}$$

where $i = \{\mathrm{b}, \mathrm{d}\}$ depending on whether we consider the bulge or disk, respectively. The results are consistent.

Figure 4.1 shows the luminosity volume density distribution of the bulge j_{b}, disk j_{d}, and galaxy j_{tot}. The units are in kpc and $\mathrm{L}_\odot$ kpc^{-3} for lengths and luminosity volume densities, respectively. All the three distributions have their maximum at the origin and decrease outwards. We choose to plot only the first quadrant because of the axisymmetric nature of our model. The luminosity volume density of the galaxy shows a peculiar disky shape (Figure 4.1c). In fact, the disk is responsible for the elongated shape along the R-axis, while the bulge is associated to the round shape along the z-axis.

Then, we project the luminosity volume density onto the sky plane. We indicate with $\vec{n}$ the LOS directed from the observer to the galaxy, and with l the integration path along the LOS. Then, the projection of the luminosity volume density along the LOS of each component $i = \{\mathrm{b,d}\}$ is given by (Caravita et al. 2021):

$$I_i = \int_{-\infty}^{\infty} j_i \, dl \quad . \tag{4.3}$$

Let us consider a Cartesian coordinates system as described in Section 2.3. In the case of an edge-on projection, the LOS is aligned with the x-axis so that $\vec{n} = -\vec{e}_x \implies dl = dx$. Furthermore, the projection plane coincides with the (y, z) plane, and $(\cos\varphi, \sin\varphi) = (x/R, y/R)$, where $R = \sqrt{x^2 + y^2}$. Therefore, changing variables from x to R, we have $dl = dx = d(\sqrt{R^2 - y^2}) = \frac{R}{\sqrt{R^2 - y^2}} dR$. Using the symmetry of the system with respect to the origin, we get:

$$I_i = 2 \int_0^{\infty} j_i \, \frac{R}{\sqrt{R^2 - y^2}} dR \quad . \tag{4.4}$$

Figure 4.2 shows the luminosity surface density distribution onto the sky plane for the bulge I_{b}, disk I_{d}, and galaxy I_{tot}. The units are in kpc and $\mathrm{L}_\odot$ kpc^{-2} for lengths and luminosity surface densities, respectively. The trends of the distributions are similar to those reported in Figure 4.1, with a maximum in the origin and decreasing outwards.

Finally, we move from astrophysical to observational units to compare our results with observations. We use Equation (2.14) to convert lengths from kpc to arcsec, and Equation (2.11) to convert luminosity surface densities into surface brightnesses from $\mathrm{L}_\odot$ kpc^{-2} to mag arcsec^{-2}. Furthermore, in order to compare model and observations in a more efficient way, we use a contour plot so that each region corresponds to a range of surface brightness (Figure 4.3a). Moreover, we extract the surface brightness profile along the major axis of the galaxy (Figure 4.3b).

We compare the photometric and kinematic data of NGC 1366 presented in Section 2.2 with the model predictions. We did not convolve the model for the PSF before comparing it to

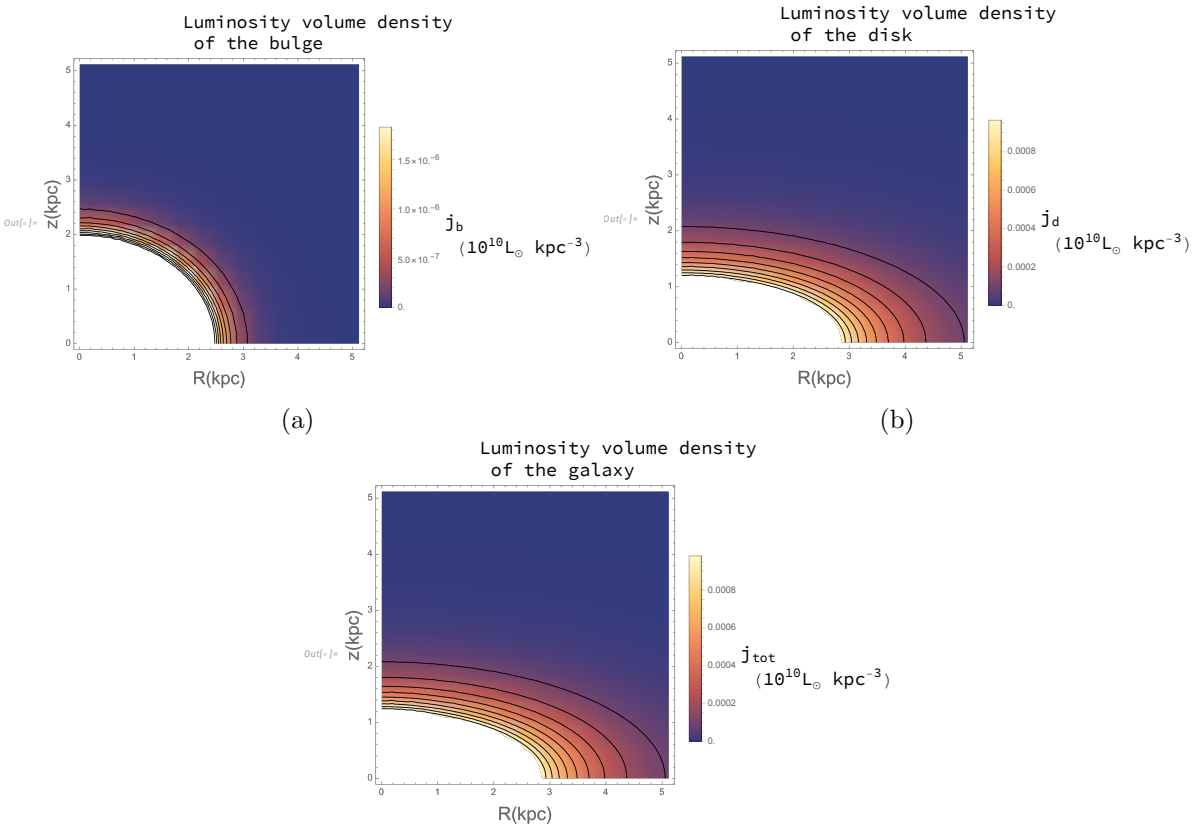

Figure 4.1: Luminosity volume density distribution of the bulge ($q_{\rm b} = 0.80$, Panel (a)), disk ($q_{\rm b} = 0.41$, Panel (b)), and galaxy (Panel (c)) for NGC 1366. Black solid lines [—] mark the curves of luminosity volume isodensity. They are spaced by $2 \cdot 10^3$ $L_\odot$ kpc^{-3} from 0 to $2 \cdot 10^4$ $L_\odot$ kpc^{-3} for the bulge, and by $1 \cdot 10^6$ $L_\odot$ kpc^{-3} from 0 to $1 \cdot 10^7$ $L_\odot$ kpc^{-3} for the disk and galaxy.

observations. We start with the surface brightness distribution of the galaxy. Comparing our modelled brightness distributions (Figure 4.3a) with the observed ones (left and middle panels of Figure 2.2), we see they are consistent with each other. The mag arcsec^{-2} range is almost the same between the two figures, going from a minimum of $\simeq 15$ mag arcsec^{-2} to a maximum of $\simeq 32$ mag arcsec^{-2}. Moreover, the shape of the isophotes is very similar becoming more and more elongated as we move outwards. As far as the surface-brightness radial profile along the major axis of the galaxy concerns and comparing the model (Figure 4.3b) with observations (Figure 2.3), we see that the curves are consistent with each other. The red dotted line has the zero point at $\simeq 17$ mag arcsec^{-2} in both the modelled and observed profiles. In contrast, the blue dotted line has the zero point at a slightly lower value in the model ($\simeq 14.75$ mag arcsec^{-2}) compared to observations ($\simeq 15.25$ mag arcsec^{-2}), which translates in a higher overall luminosity in the inner regions for the modelled profile. This is due to the fact that while the deprojected luminosity volume density of the disk is exactly reproduced by a Bessel function, as demonstrated in Equation (3.11), the deprojected luminosity volume density of the disk was described with the approximated formula in Equation (3.6), which is systematically higher than the numerical value of small radii.

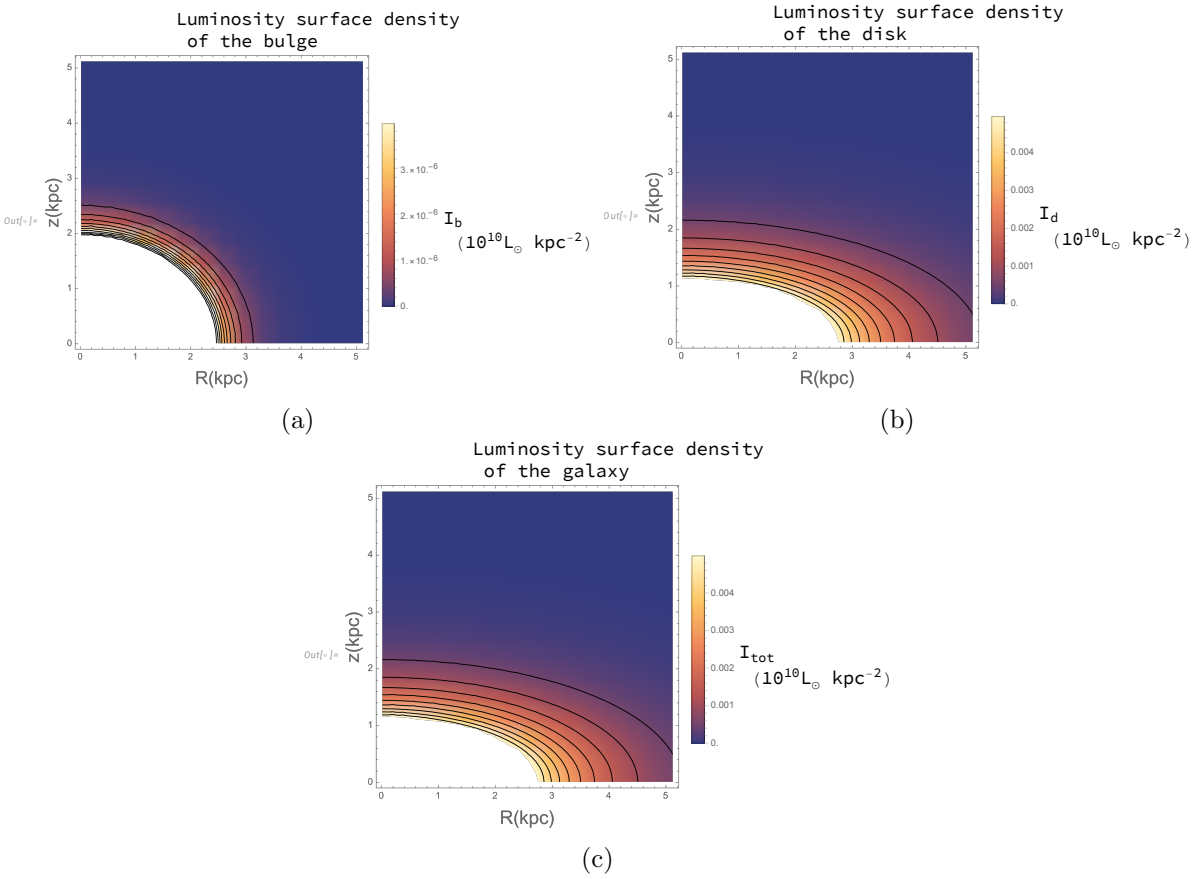

Figure 4.2: Luminosity surface density distribution of the bulge ($q_{\rm b} = 0.80$, Panel (a)), disk ($q_{\rm b} = 0.41$, Panel (b)), and galaxy (Panel (c)) for NGC 1366. Black solid lines [—] mark the curves of luminosity surface isodensity. They are spaced by $4 \cdot 10^3$ $L_\odot$ kpc^{-2} from 0 to $4 \cdot 10^4$ $L_\odot$ kpc^{-2} for the bulge, and by $5 \cdot 10^6$ $L_\odot$ kpc^{-2} from 0 to $5 \cdot 10^7$ $L_\odot$ kpc^{-2} for the disk and galaxy.

4.3 Solution of the first Jeans equation: calculation of σ_z

Now we move to the solution of the first JE. The square vertical velocity dispersion σ_z^2 of each component is expressed by Equation (3.36). Thus, $\sigma_{z,\rm b}^2$ and $\sigma_{z,\rm d}^2$ can be combined to obtain the total σ_z^2 of the galaxy. As shown in Section 3.5, we weight the velocity dispersion map both by luminosity to have $\sigma_{z\ ,\rm lw}^2$ and mass to have $\sigma_{z,\rm mw}^2$ expressed by Equations (3.42) and (3.40), respectively.

Figure 4.4 shows the result of our model giving the maps of $\sigma_{z,\rm b}$ and $\sigma_{z,\rm d}$ in the total potential, $\sigma_{z\ ,\rm lw}$ and $\sigma_{z,\rm mw}$ in astrophysical units, $\sigma_{z\ ,\rm lw}$ in observational units, and the difference $\sigma_{z\ ,\rm lw}^2 - \sigma_{z,\rm mw}^2$. In all the aforementioned maps there is a minimum at the origin. This central depression is a common feature of the $R^{1/m}$-law models, as demonstrated by Ciotti (1991): the central value of the velocity dispersion vanishes for any $m > 1$ and, as a consequence, near the center the velocity dispersion can only increase outwards. In addition, a so-called σ-drop due to the presence of young stars in a thin and kinematically cool disc can be observed (Portaluri et al. 2017). The maximum of σ_z is located in a sector which is almost circular for the bulge (Figure 4.4a) and it is elongated toward the z-axis for the disk (Figures 4.4b) and for the weighted fields (Figure 4.4c and 4.4d). The vertical elongation of $\sigma_{z,\rm d}$ is consistent with what has been shown in other disk models (De Deo et al. 2024). The intensity of the maximum ranges from $\simeq 90$ km s^{-1} for $\sigma_{z,\rm b}$ to $\simeq 150$ km s^{-1} for $\sigma_{z,\rm d}$ and it is located in a range between $\simeq 0.1$ kpc and

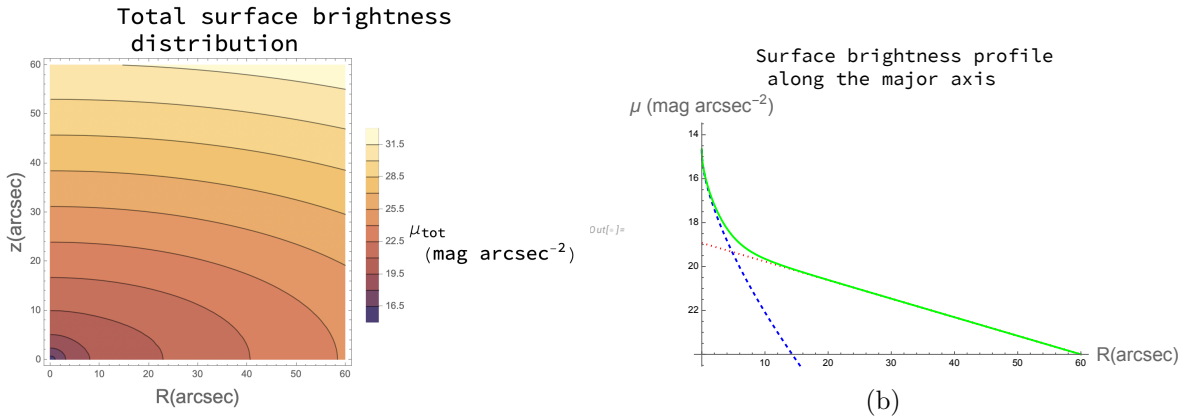

(a) (b)

Figure 4.3: Model surface brightness distribution (Panel (a)) and radial profile (Panel (b)) along the major axis of the galaxy. The blue dashed line [- -], red dotted line [· ·], and green solid line [—] correspond to contribution of the bulge, disk, and their sum, respectively.

$\simeq 0.15$ kpc from the center. Then, the value of σ_z decreases monotonically in the outskirts for all cases, consistently with Ciotti (1991). Figure 4.4e shows $\sigma_{z\ ,\mathrm{lw}}$ in arcsec instead of kpc. Furthermore, Figure 4.4f shows that the percentage difference between $\sigma_{z\ ,\mathrm{lw}}$ and $\sigma_{z,\mathrm{mw}}$ is quite small, reaching a maximum of $\simeq 3.5\%$ at a distance of 0.7 kpc from the center along the z-axis. This can be explained by the fact that, when performing the mass-weighting of the field, the density of each component is divided by its M/L. Since $(M/L)_\mathrm{d} > 1$ and $(M/L)_\mathrm{b} > 1$, the bulge and disk contributions to the mass-weighted mean is smaller than the contributions to the luminosity-weighted mean, so that $\sigma_{z\ ,\mathrm{lw}} > \sigma_{z,\mathrm{mw}}$ everywhere. Moreover, the figure shows a larger difference on the z-axis than on the R-axis. This is justified by the shape of the $\sigma_{z,\mathrm{d}}$ map, which clearly shows a more elongated figure in the vertical direction.

4.4 Solution of the second Jeans equation

Let us discuss the solution of the second JE. From Equation (3.27) Δ_σ, the difference between the mean square azimuthal velocity and the vertical velocity dispersion, is obtained for both the bulge and disk. $\Delta_{\sigma,\mathrm{b}}$ and $\Delta_{\sigma,\mathrm{d}}$ are then weighted by luminosity and mass, as shown in Section 3.5. In this way $\Delta_{\sigma\ ,\mathrm{lw}}$ and $\Delta_{\sigma,\mathrm{mw}}$ are obtained by Equations (3.42) and (3.40), respectively. The results are shown in Section 4.4.1. Then, the mean square azimuthal velocity $\overline{v_\varphi^2}$ of each component is obtained from $\Delta_\sigma = \overline{v_\varphi^2} - \sigma_z^2$. $\overline{v_{\varphi,\mathrm{b}}^2}$ and $\overline{v_{\varphi,\mathrm{d}}^2}$ are then combined to obtain $\overline{v_{\varphi\ ,\mathrm{lw}}^2}$ and $\overline{v_{\varphi,\mathrm{mw}}^2}$ by Equations (3.42) and (3.40), respectively. The results are shown in Section 4.4.2. Last but not least, we focus on the mean azimuthal velocity $\overline{v_\varphi}$ and azimuthal velocity dispersion σ_φ. As discussed in Section 3.4.2, in order to obtain $\overline{v_\varphi}$ and σ_φ we need a method to break the degeneracy between ordered and random motions. This method was discussed in Section 3.4.3. This procedure is performed for each component of the galaxy. Once the bulge and disk Satoh parameters are fixed, we proceed further. In our numerical code we analyze each of the pairs of Satoh parameters listed in Section 3.4.3. For each component, $\overline{v_\varphi}$ is obtained from Equation (3.37) and σ_φ from Equation (3.38). Finally, the fields of each component are combined to obtain the total field of the system, as shown in Section 3.5. Fields can be weighted both by luminosity and by mass. The expression of $\overline{v_{\varphi\ ,\mathrm{lw}}}$ is given by Equation (3.42), while $\overline{v_{\varphi,\mathrm{mw}}}$ is given by Equation (3.40). The results for each pair of the Satoh parameters are shown in Section 4.4.3.

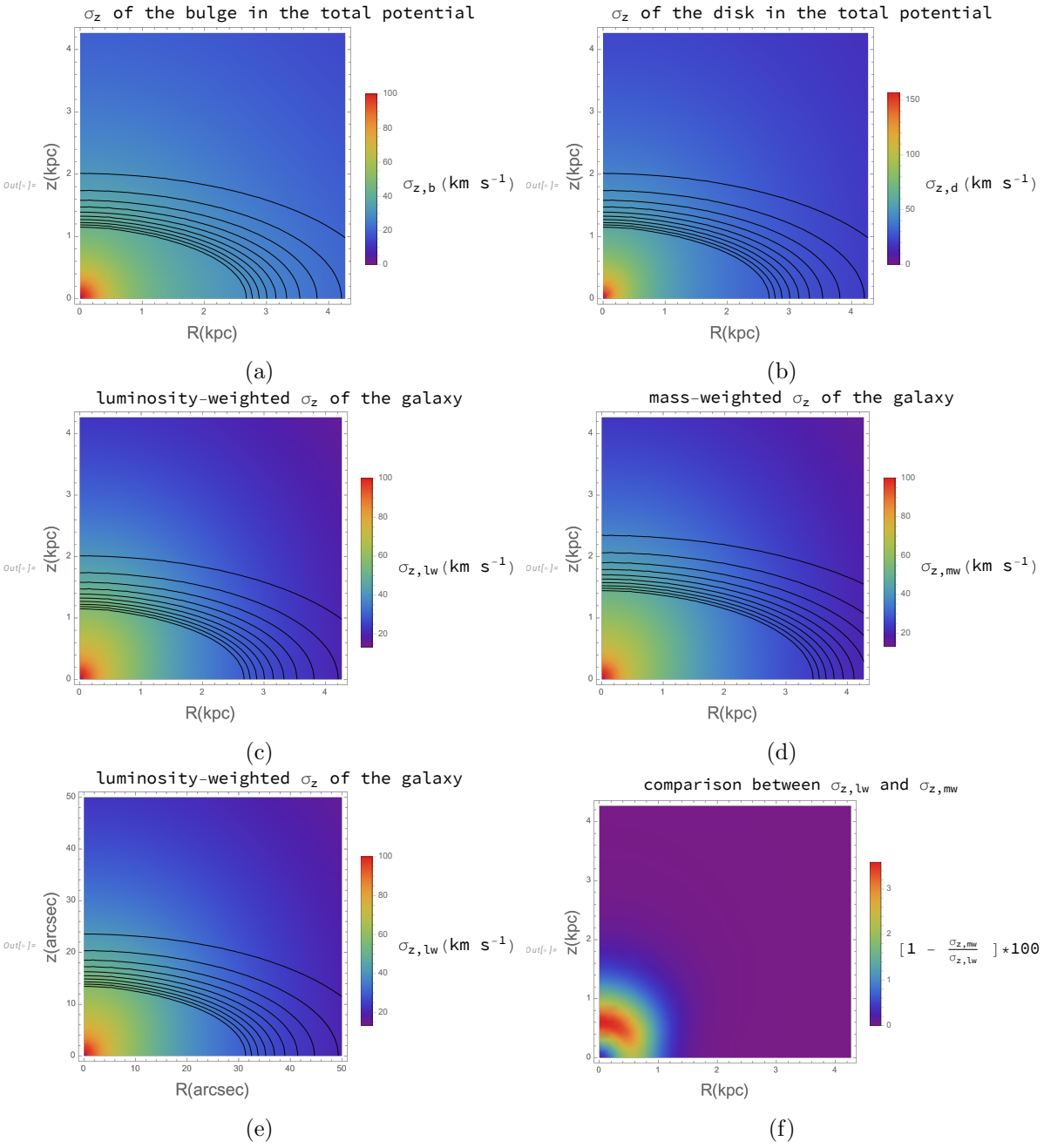

Figure 4.4: σ_z map of NGC 1366 from the first JE. Panel (a): σ_z map of the bulge in the total potential. Panel (b): σ_z map of the disk in the total potential. Panel (c): map of σ_z of the galaxy weighted by luminosity. Panel (d): map of σ_z of the galaxy weighted by mass. Panel (e): map of σ_z of the galaxy weighted by luminosity, where lengths are expressed in arcsec. Panel (f): map of the percentage difference between the luminosity-weighted and mass-weighted σ_z. Black solid lines [—] in Panels (a)-(b)-(d) and in Panels (c)-(e) mark the curve of mass and luminosity volume isodensity, respectively. They are spaced by $1.18 \cdot 10^6$ $L_\odot$ (or $M_\odot$) kpc^{-3} from 0 to $1.18 \cdot 10^7$ $L_\odot$ (or $M_\odot$) kpc^{-3}.

On the other hand, $\sigma^2_{\varphi,\mathrm{lw}}$ and $\sigma^2_{\varphi,\mathrm{mw}}$ are represented by Equations (3.43) and (3.41), respectively. The results for each pair of the Satoh parameters are presented in Section 4.4.4.

4.4.1 Calculation of $\sqrt{\Delta_\sigma}$

Figure 4.5 shows the results of our model for the square root of the difference between the mean square azimuthal velocity and the vertical velocity dispersion $\sqrt{\Delta_\sigma}$, giving the maps of $\sqrt{\Delta_{\sigma,\mathrm{b}}}$ and $\sqrt{\Delta_{\sigma,\mathrm{d}}}$ in the total potential, $\sqrt{\Delta_{\sigma\ ,\mathrm{lw}}}$ and $\sqrt{\Delta_{\sigma,\mathrm{mw}}}$ in astrophysical units, $\sqrt{\Delta_{\sigma\ ,\mathrm{lw}}}$ in observational units, and the difference $\sqrt{\Delta_{\sigma\ ,\mathrm{lw}}} - \sqrt{\Delta_{\sigma,\mathrm{mw}}}$. In all studied situations, $\sqrt{\Delta_\sigma} = 0$ km s^{-1} along the z-axis and the maximum lies along the R-axis. Concerning the bulge, the peak is located along the R-axis at $\simeq 0.3$ kpc and reaches $\simeq 60$ km s^{-1}. Its distribution has a roundish shape (Figure 4.5a). On the other hand, the peak for the disk is placed at $\simeq 0.6$ kpc, reaches $\simeq 100$ km s^{-1}, and is more smeared and elongated towards the R-axis (Figure 4.5b). Going to the luminosity and mass weights (Figure 4.5c and 4.5d, respectively), the overall shape is reminiscent of the previous ones, but with a more elongated maximum toward the R-axis, and a general increase of the values of $\sqrt{\Delta_\sigma}$ at large R and small z. Figure 4.5e shows $\sqrt{\Delta_{\sigma\ ,\mathrm{lw}}}$ in arcsec instead of kpc. Finally, Figure 4.5f shows the percentage difference between the luminosity- and the mass-weighted field. Once again $\sqrt{\Delta_{\sigma\ ,\mathrm{lw}}} > \sqrt{\Delta_{\sigma,\mathrm{mw}}}$ everywhere. The position of the peak at $\simeq 0.6$ kpc is justified by the shape of the disk maximum, as discussed for Figure 4.4f. The percentage difference is very small, ranging from 0 to $\simeq 5.5\%$.

4.4.2 Calculation of $\sqrt{\overline{v_\varphi^2}}$

Figure 4.6 shows the results of our model for the square root of the mean square azimuthal velocity $\sqrt{\overline{v_\varphi^2}}$, giving the maps of $\sqrt{\overline{v_{\varphi,\mathrm{b}}^2}}$ and $\sqrt{\overline{v_{\varphi,\mathrm{d}}^2}}$ in the total potential, $\sqrt{\overline{v_\varphi^2}_{\ ,\mathrm{lw}}}$ and $\sqrt{\overline{v_{\varphi,\mathrm{mw}}^2}}$ in astrophysical units, $\sqrt{\overline{v_\varphi^2}_{\ ,\mathrm{lw}}}$ in observational units, and the difference $\sqrt{\overline{v_\varphi^2}_{\ ,\mathrm{lw}}} - \sqrt{\overline{v_{\varphi,\mathrm{mw}}^2}}$. Both the bulge (Figure 4.6a) and disk (Figure 4.6b) show an off-centered peak near the origin, and spread mostly along the R-axis. The maximum value of $\sqrt{\overline{v_\varphi^2}}$ for the bulge ($\simeq 110$ km s^{-1}) is smaller than that of the disk ($\simeq 160$ km s^{-1}). They are located both at $\simeq 0.2$ kpc. The horizontal elongation is greater than the vertical elongation in both cases, but especially for the disk component. The combination of the fields of the components gives rise to two maxima for both the luminosity- (Figure 4.6c) and mass-weighted (Figure 4.6d) fields. These peaks are not well-separated, and they blend with each other. However, they are located at a distance of $\simeq 0.2$ kpc and $\simeq 1$ kpc from the center along the R-axis. Figure 4.6e shows $\sqrt{\overline{v_\varphi^2}_{\ ,\mathrm{lw}}}$ in arcsec instead of kpc. Finally, Figure 4.6f shows the percentage difference between the luminosity- and mass-weighted field. $\sqrt{\overline{v_\varphi^2}_{\ ,\mathrm{lw}}} > \sqrt{\overline{v_{\varphi,\mathrm{mw}}^2}}$ everywhere. Once again the position of the peak at $\simeq 0.6$ kpc is justified by the shape of the disk maximum, as discussed for Figure 4.4f. The percentage difference is very small, ranging from 0 to $\simeq 4\%$.

4.4.3 Calculation of $\overline{v_\varphi}$

In the following we consider our five different models characterized by five different pairs of Satoh parameters, as defined in Section 3.4.3: the non-rotating galaxy model ($k_\mathrm{b} = 0$, $k_\mathrm{d} = 0$), non-rotating bulge model ($k_\mathrm{b} = 0$, $k_\mathrm{d} = 1$), maximally counter-rotating model ($k_\mathrm{b} = -1$, $k_\mathrm{d} = 1$), mildly counter-rotating model ($k_\mathrm{b} = -1/2$, $k_\mathrm{d} = 1/2$), and moderately counter-rotating model ($k_\mathrm{b} = -3/4$, $k_\mathrm{d} = 3/4$).

Figure 4.7 shows the results for the non-rotating galaxy model. For both the luminosity- (Figure 4.7a) and mass-weighted (Figure 4.7b) fields, it is $\overline{v_\varphi} = 0$ km s^{-1} everywhere, as it is expected since we did not impose any rotation to our system. The same is true for both the bulge and disk, separately.

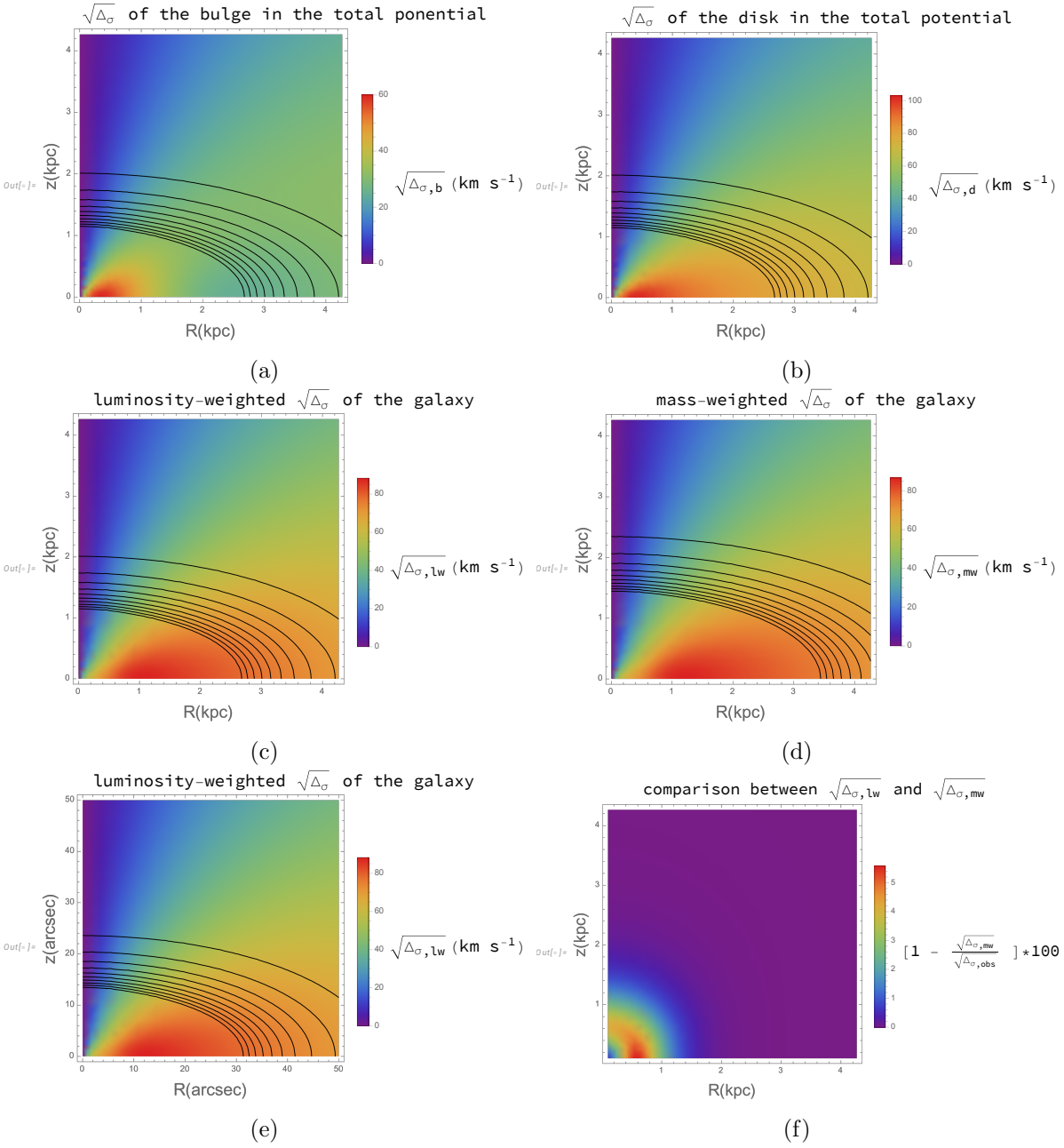

Figure 4.5: $\sqrt{\Delta_\sigma}$ map of NGC 1366 from the second JE. Panel (a): $\sqrt{\Delta_\sigma}$ map of the bulge in the total potential. Panel (b): $\sqrt{\Delta_\sigma}$ map of the disk in the total potential. Panel (c): map of $\sqrt{\Delta_\sigma}$ of the galaxy weighted by luminosity. Panel (d): map of $\sqrt{\Delta_\sigma}$ of the galaxy weighted by mass. Panel (e): map of $\sqrt{\Delta_\sigma}$ of the galaxy weighted by luminosity, where lengths are expressed in arcsec. Panel (f): map of the percentage difference between the luminosity-weighted and mass-weighted $\sqrt{\Delta_\sigma}$. Black solid lines [—] in Panels (a)-(b)-(d) and in Panels (c)-(e) mark the curve of mass and luminosity volume isodensity, respectively. They are spaced by $1.18 \cdot 10^6$ $L_\odot$ (or $M_\odot$) kpc^{-3} from 0 to $1.18 \cdot 10^7$ $L_\odot$ (or $M_\odot$) kpc^{-3}.

Figure 4.8 shows the results for the non-rotating bulge model. Since the bulge does not rotate ($k_\mathrm{b} = 0$), it is $\overline{v_\varphi}_{,\mathrm{b}} = 0$ km s^{-1} everywhere (Figure 4.8a). On the other hand, the map of $\overline{v_\varphi}_{,\mathrm{d}}$ (Figure 4.8b) is exactly the same as that of $\Delta_{\sigma,\mathrm{d}}$ shown in Figure 4.5b. In fact, from

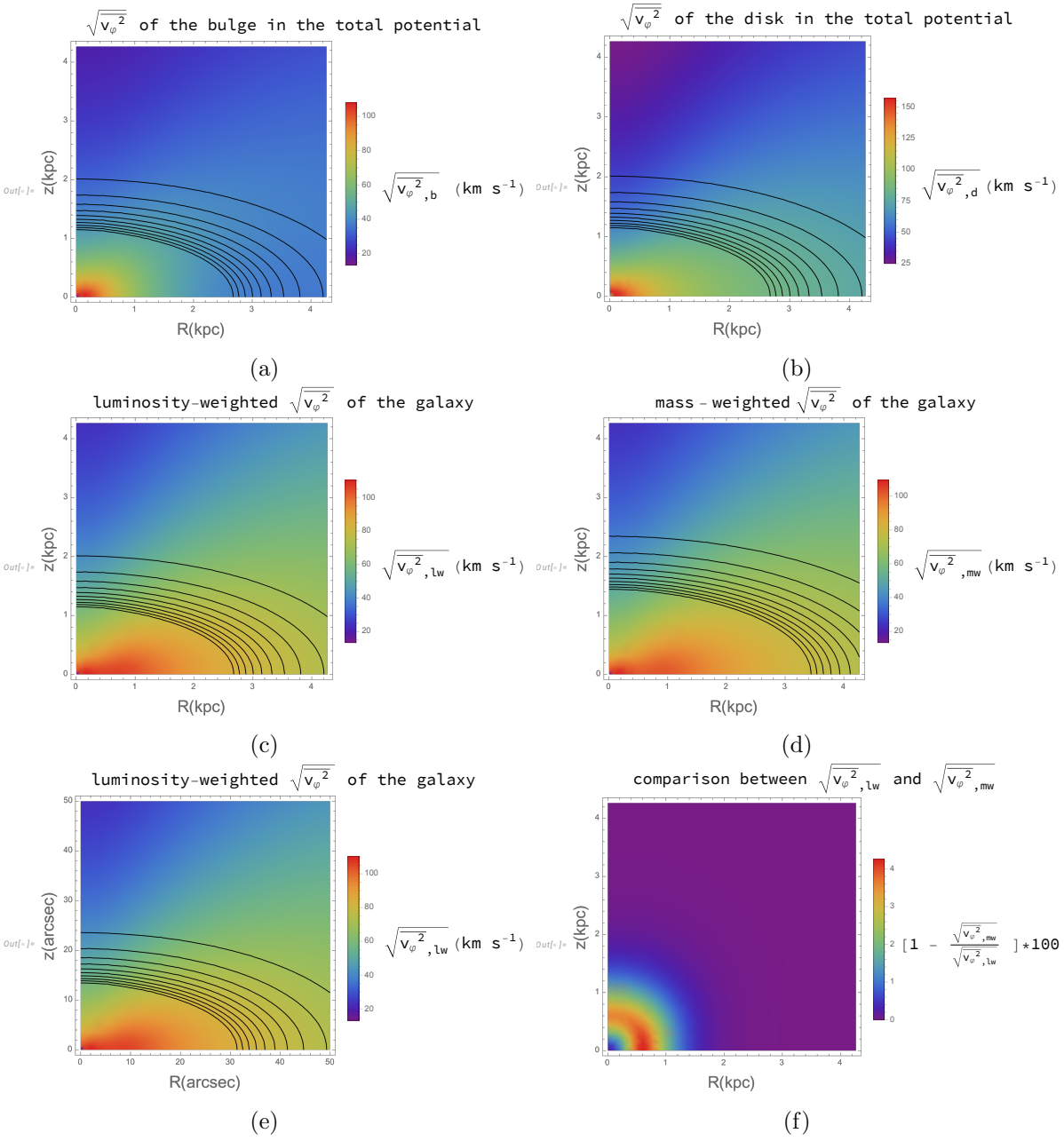

Figure 4.6: As in Figure 4.5 but for $\sqrt{\overline{v_\varphi^2}}$.

Equation (3.37) it is $\overline{v_\varphi}_{,\mathrm{d}} = \Delta_{\sigma,\mathrm{d}}$ since $k_\mathrm{d} = 1$. Therefore, the disk shows no rotation along the z-axis and a maximum rotation at $R \simeq 0.6$ kpc along the R-axis, where it reaches a value of $\simeq 100$ km s^{-1}. The combination of the field components shows a sort of vertical region of radius 0.3 kpc and parallel to the z-axis, where there is no or little rotation. The value of $\overline{v_\varphi}$ increases for large R and small z, with a maximum of $\simeq 80$ km s^{-1} at $R \simeq 1.5$ kpc. The luminosity- (Figure 4.8c) and mass-weighted $\overline{v_\varphi}$ (Figure 4.8d) show a very similar behaviour. Figure 4.8e shows $\overline{v_\varphi}_{,\mathrm{lw}}$ in arcsec instead of kpc for a better comparison with observations.

Figures 4.9, 4.10, and 4.11 show the results for the maximally counter-rotating, mildly counter-rotating, and moderately counter-rotating models, respectively. For all the single components case, the shapes resemble the Δ_σ simulations (Figure 4.5a and 4.5b), but the values are rescaled

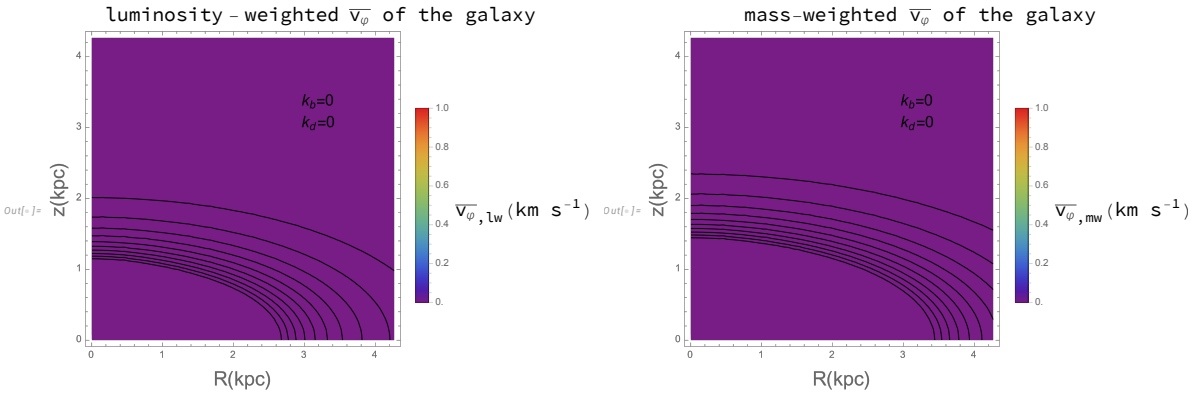

(a) (b)

Figure 4.7: $\overline{v_\varphi}$ map of NGC 1366 from the second JE for the non-rotating galaxy model ($k_\mathrm{b} = 0$, $k_\mathrm{d} = 0$). Panel (a): map of $\overline{v_\varphi}$ of the galaxy weighted by luminosity. Panel (b): map of $\overline{v_\varphi}$ of the galaxy weighted by mass. Black solid lines [—] mark the curve of luminosity (or mass) volume isodensity. They are spaced by $1.18 \cdot 10^6$ $\mathrm{L}_\odot$ (or $\mathrm{M}_\odot$) kpc^{-3} from 0 to $1.18 \cdot 10^7$ $\mathrm{L}_\odot$ (or $\mathrm{M}_\odot$) kpc^{-3}.

and signs are changed based on the value of k. For $k = 1$ the values range is exactly the same, as shown when dealing with the non-rotating bulge model; for $k = 1/2$ the values are halved; for $k = 3/4$ the values are three-quartered; if there is the minus sign, all values are inverted. Nevertheless, a difference arises when we combine these different maps, because in this case the two components are counter-rotating. We get the presence of a negative and a positive peak located along the R-axis at $\simeq 0.2$ kpc and at $\simeq 1.5$ kpc, respectively, for both the luminosity- and mass-weighted fields of the maximally counter-rotating (Figures 4.9c and 4.9d), mildly counter-rotating (Figures 4.10c and 4.10d), and moderately counter-rotating (Figures 4.11c and 4.11d) models. In all these cases, there is no rotation along the z-axis. The maximum velocity excursion is -50 km s^{-1} $\lesssim \overline{v_\varphi}_{,\mathrm{lw}} \simeq \overline{v_\varphi}_{,\mathrm{mw}} \lesssim 75$ km s^{-1} for the maximally counter-rotating model. The range is then halved for the mildly counter-rotating case, and three-quartered for the moderately counter-rotating case. Finally, Figures 4.9e, 4.10e and 4.11e show $\overline{v_\varphi}_{,\mathrm{lw}}$ in arcsec instead of kpc for the maximally, mildly, and moderately counter-rotating models, respectively. These plots can help to make comparison between the observed and modeled values.

4.4.4 Calculation of σ_φ

Figure 4.12 shows the result for σ_φ in the non-rotating galaxy model. The plots for $\sigma_{\varphi,\mathrm{lw}}$ (Figure 4.12a) and $\sigma_{\varphi,\mathrm{mw}}$ (Figure 4.12b) are exactly the same as those for $\sqrt{\overline{v_\varphi^2}_{,\mathrm{lw}}}$ (Figure 4.6c) and $\sqrt{\overline{v_{\varphi,\mathrm{mw}}^2}}$ (Figure 4.6d), respectively. In fact, if we refer to Equation (3.38), $k = 0 \implies \sigma_\varphi = \overline{v_\varphi^2}$. Therefore, all the considerations made when discussing Figure 4.6 are true also for this case, as the presence of the two peaks lying along the R-axis at $R \simeq 0.2$ kpc and $R \simeq 1$ kpc which blend one another. Furthermore, the image shows a central σ-drop, which is a common feature of the σ profiles (Ciotti 1991; Portaluri et al. 2017). Figure 4.12 reports just the luminosity- and the mass-weighted fields, since for $\sigma_{\varphi,\mathrm{b}}$, $\sigma_{\varphi,\mathrm{d}}$, and $\sigma_{\varphi,\mathrm{lw}}$ in observational units we can refer to Figure 4.6a, 4.6b, and 4.6e, respectively. We can apply the same considerations made earlier when discussing about $\sqrt{\overline{v_\varphi^2}}$.

Figure 4.13 shows the result for σ_φ in the non-rotating bulge model. $\sigma_{\varphi,\mathrm{b}}$ and $\sigma_{\varphi,\mathrm{d}}$ are shown in Figures 4.8a and 4.8b, respectively. $\sigma_{\varphi,\mathrm{b}} = 0$ km s^{-1} in the center; then, it increases outwards,

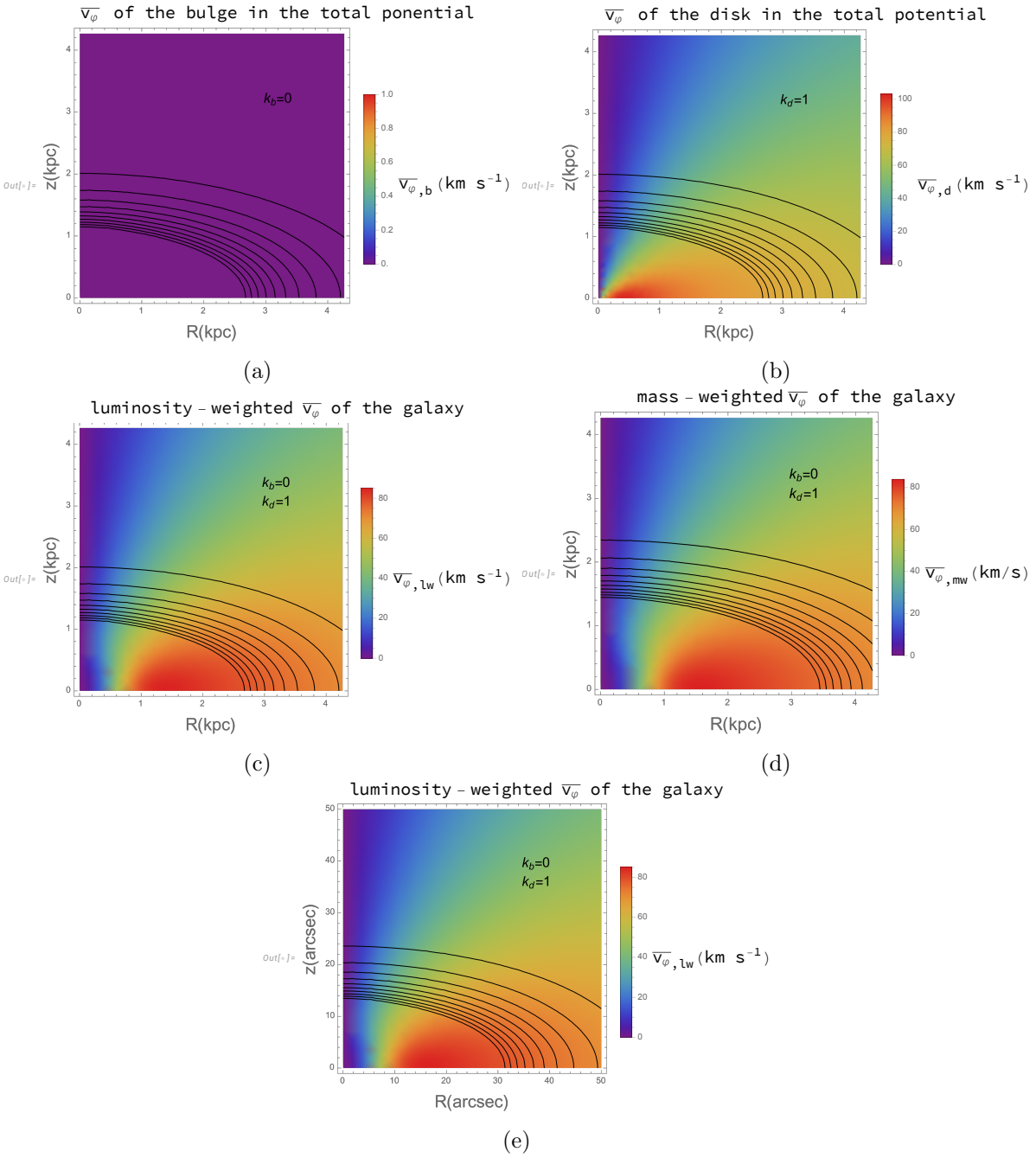

Figure 4.8: $\overline{v_\varphi}$ map of NGC 1366 from the second JE for the non-rotating bulge model ($k_\mathrm{b} = 0$, $k_\mathrm{d} = 1$). Panel (a): $\overline{v_\varphi}$ map of the bulge in the total potential. Panel (b): $\overline{v_\varphi}$ map of the disk in the total potential. Panel (c): map of $\overline{v_\varphi}$ of the galaxy weighted by luminosity. Panel (d): map of $\overline{v_\varphi}$ of the galaxy weighted by mass. Panel (e): map of $\overline{v_\varphi}$ of the galaxy weighted by luminosity, where lengths are expressed in arcsec. Black solid lines [—] in Panels (a)-(b)-(d) and in Panels (c)-(e) mark the curve of mass and luminosity volume isodensity, respectively. They are spaced by $1.18 \cdot 10^6$ $\mathrm{L}_\odot$ (or $\mathrm{M}_\odot$) kpc^{-3} from 0 to $1.18 \cdot 10^7$ $\mathrm{L}_\odot$ (or $\mathrm{M}_\odot$) kpc^{-3}.

reaching a peak at $\lesssim 0.4$ kpc and it decreases monotonically in the outskirts. The peak is not symmetric with respect to the origin, but is more extended toward the R-axis. The maximum value is $\sigma_{\varphi,\mathrm{b}} \simeq 110$ km s^{-1}. Since $k_\mathrm{b} = 0$, this plot is similar to the one for $\sqrt{\overline{v^2_{\varphi,\mathrm{b}}}}$ shown in

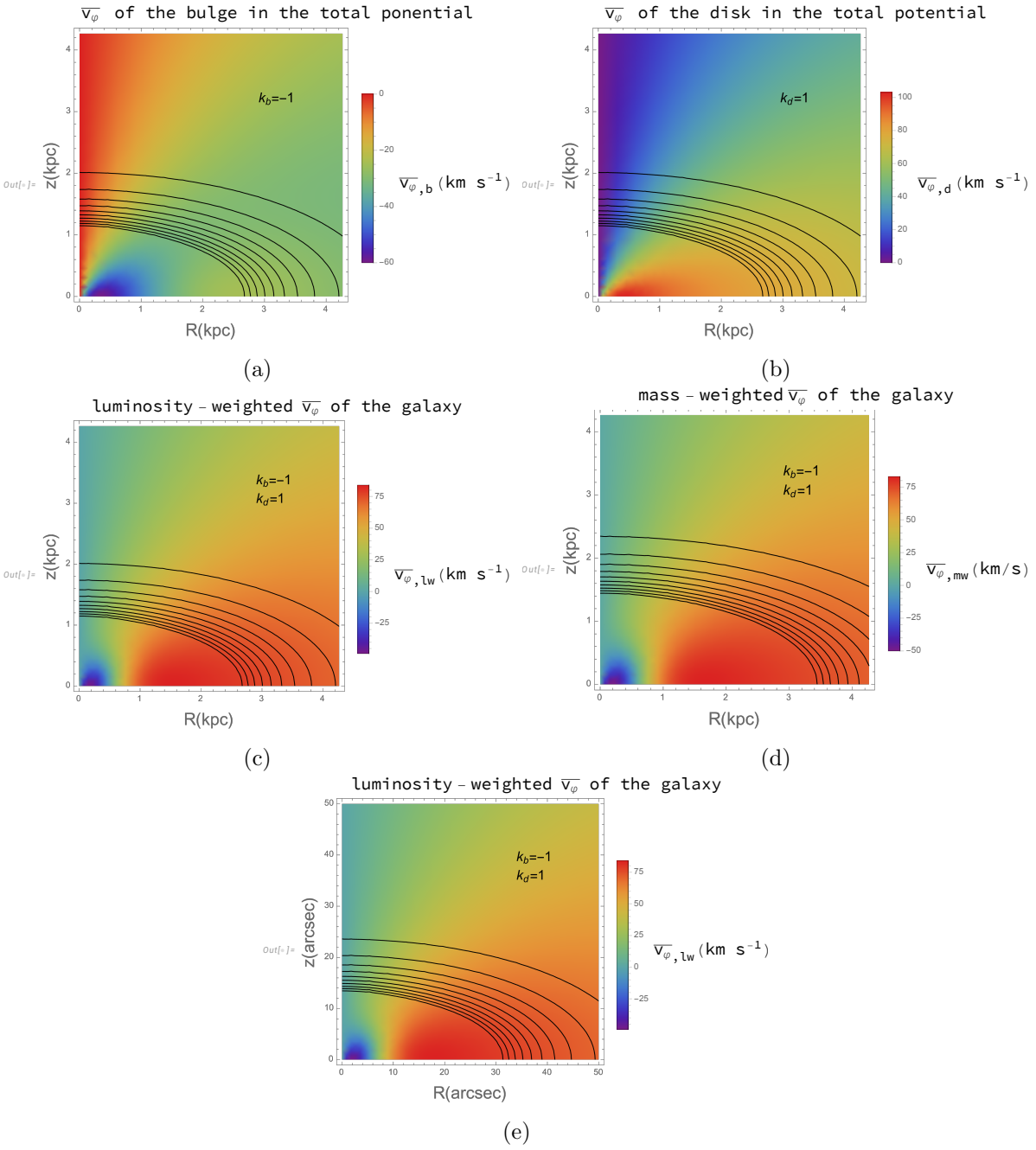

Figure 4.9: As in figure 4.8 but for the maximally counter-rotating model ($k_\mathrm{b} = -1$, $k_\mathrm{d} = 1$).

Figure 4.6a. The disk has a similar behaviour with a central σ-drop, a maximum in a sector at $\simeq 0.2$ kpc from the center, and a dip in the outskirts. In this case the maximum is more elongated in the z direction and reaches $\sigma_{\varphi,\mathrm{d}} \simeq 160$ km s^{-1}. Moreover, the points located at high R and z are characterized by smaller value of $\sigma_{\varphi,\mathrm{d}}$ with respect to the bulge model. Figure 4.8b, which shows $\sigma_{\varphi,\mathrm{d}}$ with $k_\mathrm{d} = 1$, is the same as Figure 4.4b, which shows $\sigma_{z,\mathrm{d}}$. In fact, $k = 1 \implies \sigma_\varphi = \sigma_z$ from Equation (3.38). The luminosity- and mass- weighted fields are shown in Figures 4.13c and 4.13d, respectively. A central σ depression is present in both cases. Moreover, a maximum region of irregular shape is concentrated along the R-axis at $\simeq 0.3$ kpc. It goes up to a value of $\sigma_{\varphi,\mathrm{lw}} \simeq \sigma_{\varphi,\mathrm{mw}} \simeq 110$ km s^{-1}. Large R and z are characterized by low

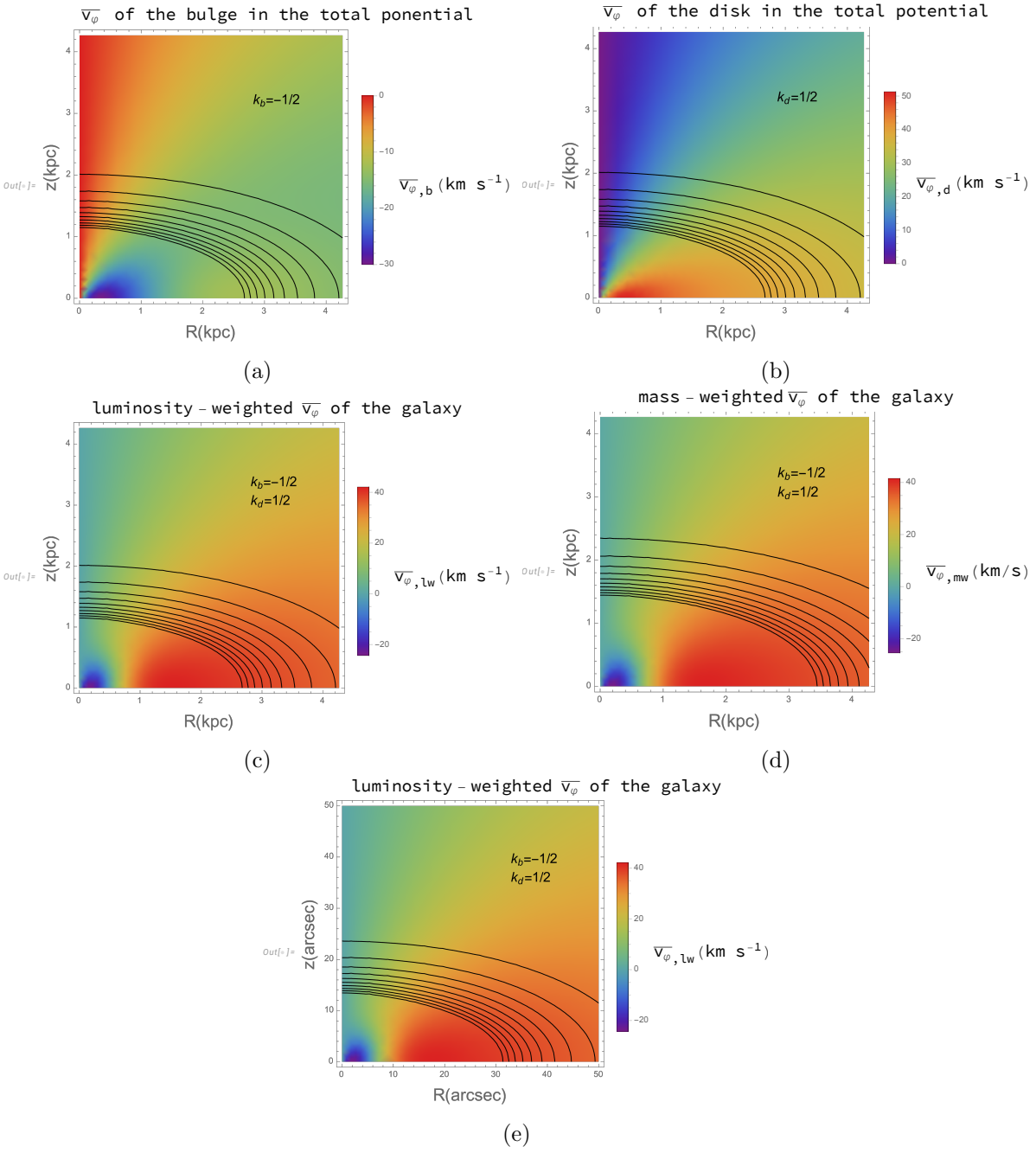

Figure 4.10: As in Figure 4.8 but for the mildly counter-rotating model ($k_\mathrm{b} = -1/2$, $k_\mathrm{d} = 1/2$).

values of $\sigma_{\varphi,\mathrm{lw}}$ and $\sigma_{\varphi,\mathrm{mw}}$. While the combination of $\overline{v_\varphi}_{,\mathrm{b}}$ and $\overline{v_\varphi}_{,\mathrm{d}}$ is a fairly straightforward weighted average and we can intuitively figure out the final result, this is not so intuitive in the case of σ_φ, as the fields combine in a less linear way (Equations 3.43 and 3.41). Figure 4.13e shows $\sigma_{\varphi,\mathrm{lw}}$ for the non-rotating bulge model in arcsec instead of kpc for better comparison with observations.

Figure 4.14 shows the result for σ_φ for the maximally counter-rotating model. This is the first case of σ_φ where counter-rotation is present. Since $k_{\mathrm{b/d}} = |1|$, it is $\sigma_{\varphi,\mathrm{b}} = \sigma_{z,\mathrm{b}}$ and $\sigma_{\varphi,\mathrm{d}} = \sigma_{z,\mathrm{d}}$, which are shown in Figures 4.4a and 4.4b, respectively. Therefore, the considerations made in Section 4.3 can be extended to this case. Things change when $\sigma_{\varphi,\mathrm{b}}$ and $\sigma_{\varphi,\mathrm{d}}$ are combined. $\sigma_{\varphi,\mathrm{lw}}$

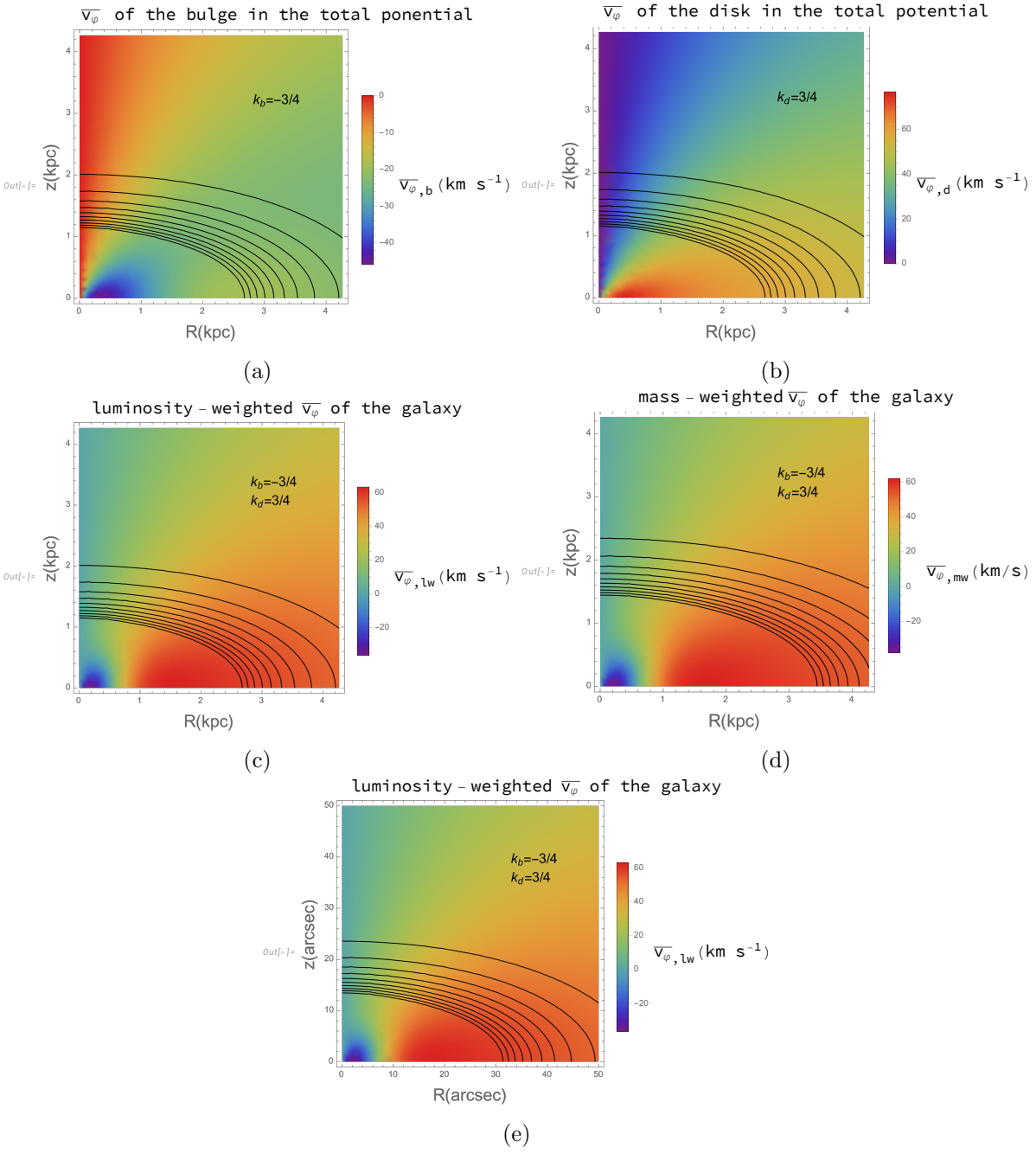

Figure 4.11: As in Figure 4.8 but for the moderately counter-rotating model ($k_\mathrm{b} = -3/4$, $k_\mathrm{d} = 3/4$).

and $\sigma_{\varphi,\mathrm{mw}}$ are shown in Figures 4.14c and 4.14d, respectively. Two maxima are present, both surrounding the R-axis. They are located at $R \simeq 0.2$ kpc and $R \simeq 0.5$ kpc. Their boundaries are not well defined, and the two mix in some places. The maximum vertical elongation of the peak is $z \simeq 0.5$ kpc. $\sigma_{\varphi,\mathrm{lw}}$ and $\sigma_{\varphi,\mathrm{mw}}$ show a similar behaviour, but are characterized by slightly different values of σ_φ, which ranges from 0 to $\simeq 105$ km s^{-1} for the bulge and from 0 to $\simeq 100$ km s^{-1} for the disk. Figure 4.14e shows $\sigma_{\varphi,\mathrm{lw}}$ for the maximally counter-rotating model in arcsec instead of kpc for better comparison with observations.

Figure 4.15 shows the result for σ_φ for the mildly counter-rotating model. This is the first case

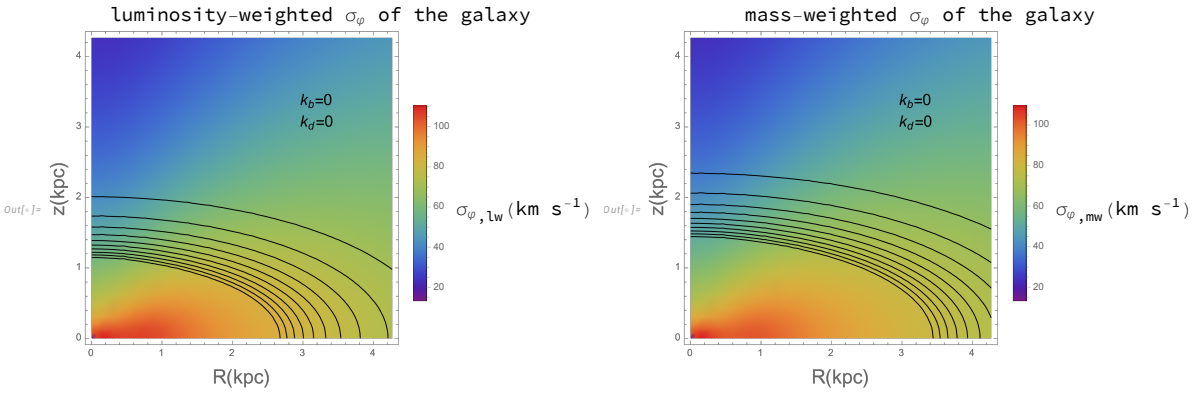

(a) (b)

Figure 4.12: σ_φ map of NGC 1366 from the second JE for the non-rotating galaxy model ($k_\mathrm{b} = 0$, $k_\mathrm{d} = 0$). Panel (a): map of σ_φ of the galaxy weighted by luminosity. Panel (b): map of σ_φ of the galaxy weighted by mass. Black solid lines [—] mark the curve of luminosity (or mass) volume isodensity. They are spaced by $1.18 \cdot 10^6$ $\mathrm{L}_\odot$ (or $\mathrm{M}_\odot$) kpc^{-3} from 0 to $1.18 \cdot 10^7$ $\mathrm{L}_\odot$ (or $\mathrm{M}_\odot$) kpc^{-3}.

in which σ_φ is a non-trivial combination of $\overline{v_\varphi^2}$ and σ_z. Figures 4.15a and 4.15b show $\sigma_{\varphi,\mathrm{b}}$ and $\sigma_{\varphi,\mathrm{d}}$, respectively. Both maps show the characteristic central σ-drop. Then, a maximum is displayed in an almost circular sector at $\simeq 0.2$ kpc from the center. The width of the bulge maximum is slightly wider than disk maximum. Furthermore, $\sigma_{\varphi,\mathrm{b}} \lesssim 105$ km s^{-1} while $\sigma_{\varphi,\mathrm{b}} \lesssim 160$ km s^{-1}. $\sigma_{\varphi,\mathrm{lw}}$ (Figure 4.15c) and $\sigma_{\varphi,\mathrm{mw}}$ (Figure 4.15d) are lower in a region which surrounds the R-axis, and which extends widely toward the R direction. Two peaks are present and are located at $R \simeq 0.2$ kpc and $R \simeq 0.6$ kpc. It is $\sigma_{\varphi,\mathrm{lw}} \simeq \sigma_{\varphi,\mathrm{lw}} \lesssim 105$ km s^{-1}. The outskirts are characterized by larger values of $\sigma_{\varphi,\mathrm{lw}}$ and $\sigma_{\varphi,\mathrm{mw}}$ with respect to the maximally counter-rotating model. Moreover, the region of the maxima is more extended and the boundaries of the peaks are less pronounced with respect to the maximally counter-rotating model. Figure 4.15e shows $\sigma_{\varphi,\mathrm{lw}}$ for the mildly counter-rotating model in arcsec instead of kpc for better comparison with observations.

Figure 4.16 shows the result for σ_φ in the moderately counter-rotating model. $\sigma_{\varphi,\mathrm{b}}$ and $\sigma_{\varphi,\mathrm{d}}$ are shown in Figures 4.11a and 4.11b, respectively, and $\sigma_{\varphi,\mathrm{lw}}$ and $\sigma_{\varphi,\mathrm{mw}}$ are shown in Figures 4.11c and 4.11d, respectively. This model is in between the maximally and mildly counter-rotating models: the boundaries of the maxima are more blended with respect to the maximally counter-rotating model, but less pronounced than the mildly counter-rotating model. Moreover, both the σ_φ peak values and σ_φ values far away from the origin are in between the two previously analyzed models. Finally, Figure 4.16e shows $\sigma_{\varphi,\mathrm{lw}}$ for the moderately counter-rotating model in arcsec instead of kpc for better comparison with observations.

4.5 Comparison between models and integral-field spectroscopic observations

We now proceed with a comparison between the observed and modeled fields. While the observed profiles show v and σ along the LOS, our models compute $\overline{v_\varphi}$ and σ_φ, meaning the azimuthal components of the fields. For the velocity, this does not represent a limitation. In fact, since the galaxy is seen edge on and since we assume that $\overline{v_R} = \overline{v_z} = 0$ km s^{-1}, we right away get that $\overline{v_\varphi} = v_\mathrm{LOS}$. For the velocity dispersion, the case is different. In this case, $\sigma_R = \sigma_z$ is not

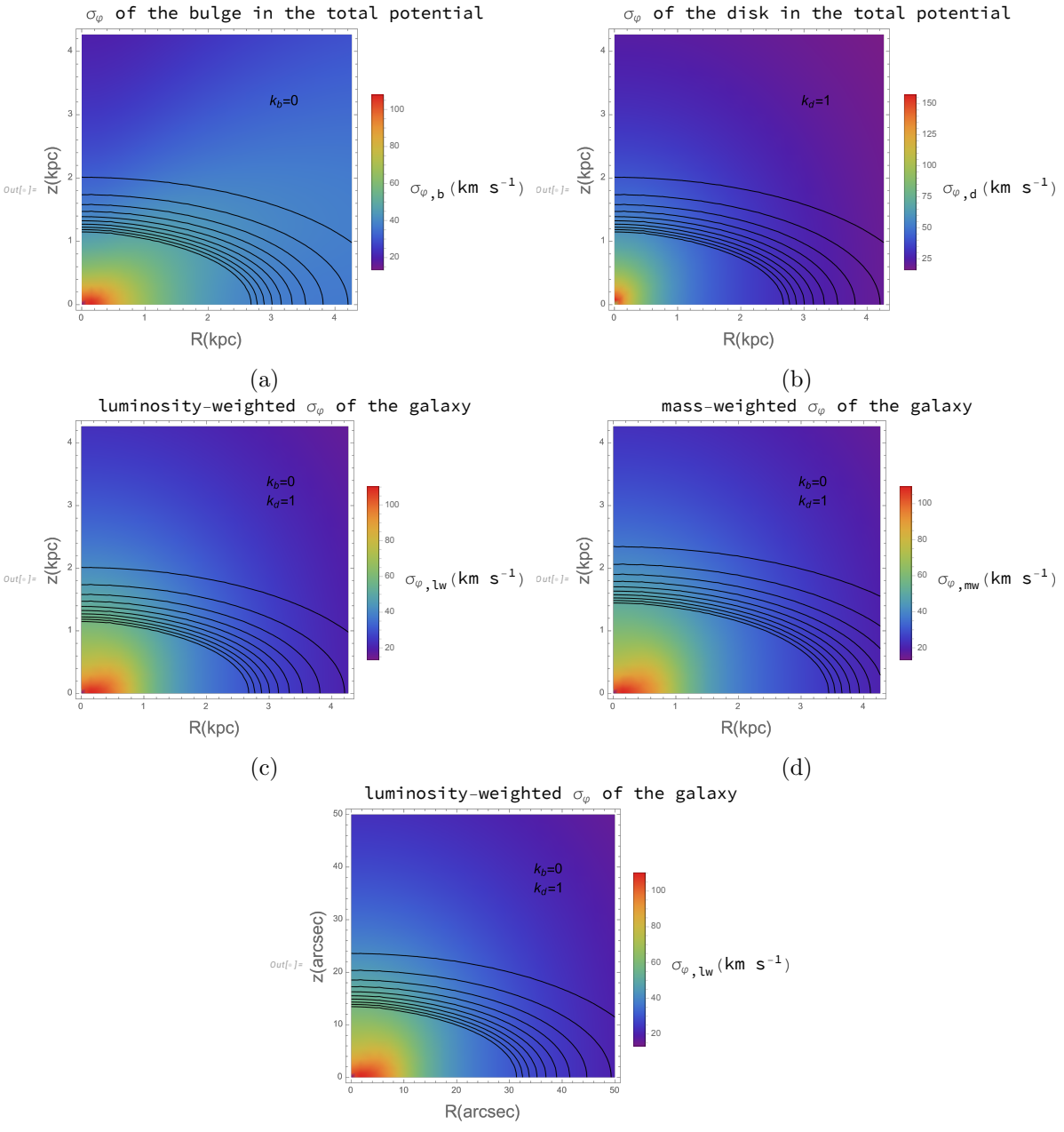

Figure 4.13: σ_φ map of NGC 1366 from the second JE for the non-rotating bulge model ($k_\mathrm{b} = 0$, $k_\mathrm{d} = 1$). Panel (a): σ_φ map of the bulge in the total potential. Panel (b): σ_φ map of the disk in the total potential. Panel (c): map of σ_φ of the galaxy weighted by luminosity. Panel (d): map of σ_φ of the galaxy weighted by mass. Panel (e): map of σ_φ of the galaxy weighted by luminosity, where lengths are expressed in arcsec. Black solid lines [—] in Panels (a)-(b)-(d) and in Panels (c)-(e) mark the curve of mass and luminosity volume isodensity, respectively. They are spaced by $1.18 \cdot 10^6$ $\mathrm{L}_\odot$ (or $\mathrm{M}_\odot$) kpc^{-3} from 0 to $1.18 \cdot 10^7$ $\mathrm{L}_\odot$ (or $\mathrm{M}_\odot$) kpc^{-3}.

necessarily zero, and this implies that in general $\sigma_\varphi \neq \sigma_\mathrm{LOS}$. The comparison is yet useful to have an idea of the general behaviour of the galaxy.

Let us start with v_LOS. integral-field spectroscopic observations are shown in the upper left panel of Figure 2.6. We compare them with the maps of the non-rotating bulge model (Figure

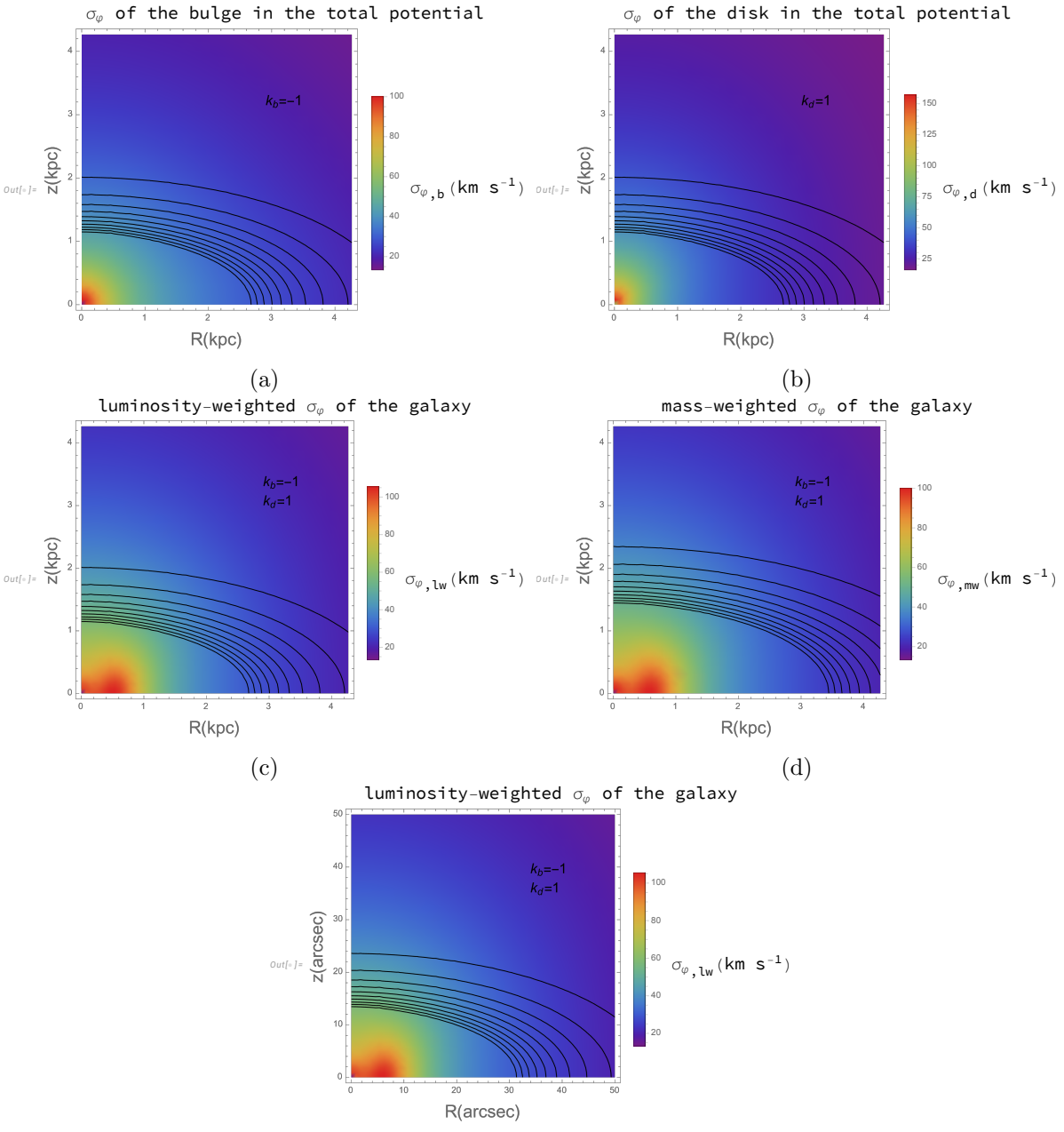

Figure 4.14: As in Figure 4.13 but for the maximally counter-rotating model ($k_{\rm b} = -1$, $k_{\rm d} = 1$).

4.8e), maximally counter-rotating model (Figure 4.9e), mildly counter-rotating model (Figure 4.10e), and moderately counter-rotating model (Figure 4.11e). The non-rotating bulge model is immediately ruled out, because it does not reproduce the inner peak of the $v_{\rm LOS}$. On the other hand, all the counter-rotating cases correctly reproduce the counter-rotation of the system at a certain radius, and the two positive/negative velocity peaks. However, all the counter-rotating models have critical issues. Specifically, the velocity values fail to match the observed data for all these cases. In fact, the maximum modeled range is that of the maximally counter-rotating model, for which -50 km s$^{-1} \lesssim \overline{v_\varphi}_{,\rm lw} \lesssim 75$ km s^{-1}. Moreover, the reduction of k leads to a reduction of the velocity range proportional to k itself. On the other hand, the observed velocity range is -75 km s$^{-1} \lesssim v_{\rm LOS} \lesssim 100$ km s^{-1}.

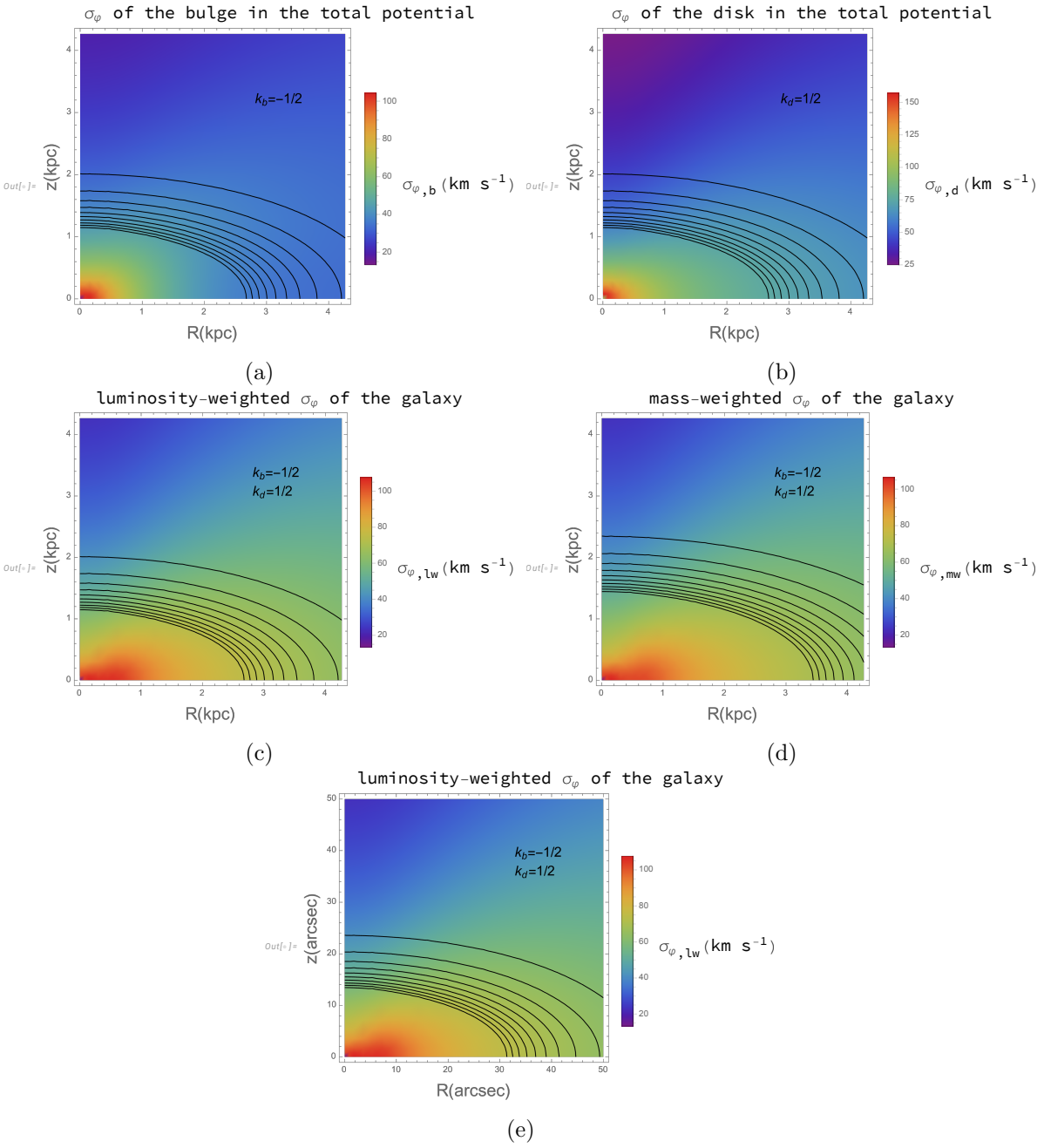

Figure 4.15: As in Figure 4.13 but for the mildly counter-rotating model ($k_{\rm b} = -1/2$, $k_{\rm d} = 1/2$).

Let us move to $\sigma_{\rm LOS}$. integral-field spectroscopic observations are shown in the lower left panel of Figure 2.6. We compare them with the maps of the non-rotating bulge model (Figure 4.13e), maximally counter-rotating model (Figure 4.14e), mildly counter-rotating model (Figure 4.15e), and moderately counter-rotating model (Figure 4.16e). The non-rotating bulge model is immediately ruled out, because it does not reproduce the double peak feature of the observed $\sigma_{\rm LOS}$. On the other hand, all the counter-rotating cases correctly reproduce the presence of the two peaks located at different radii. However, all the counter-rotating models show some problems. For example, the values of σ_φ are not consistent with those observed in any of these cases. Furthermore, varying the Satoh parameters does not significantly change the σ_φ values. Moreover, for the maximally counter-rotating model, the position of the two peaks in the model

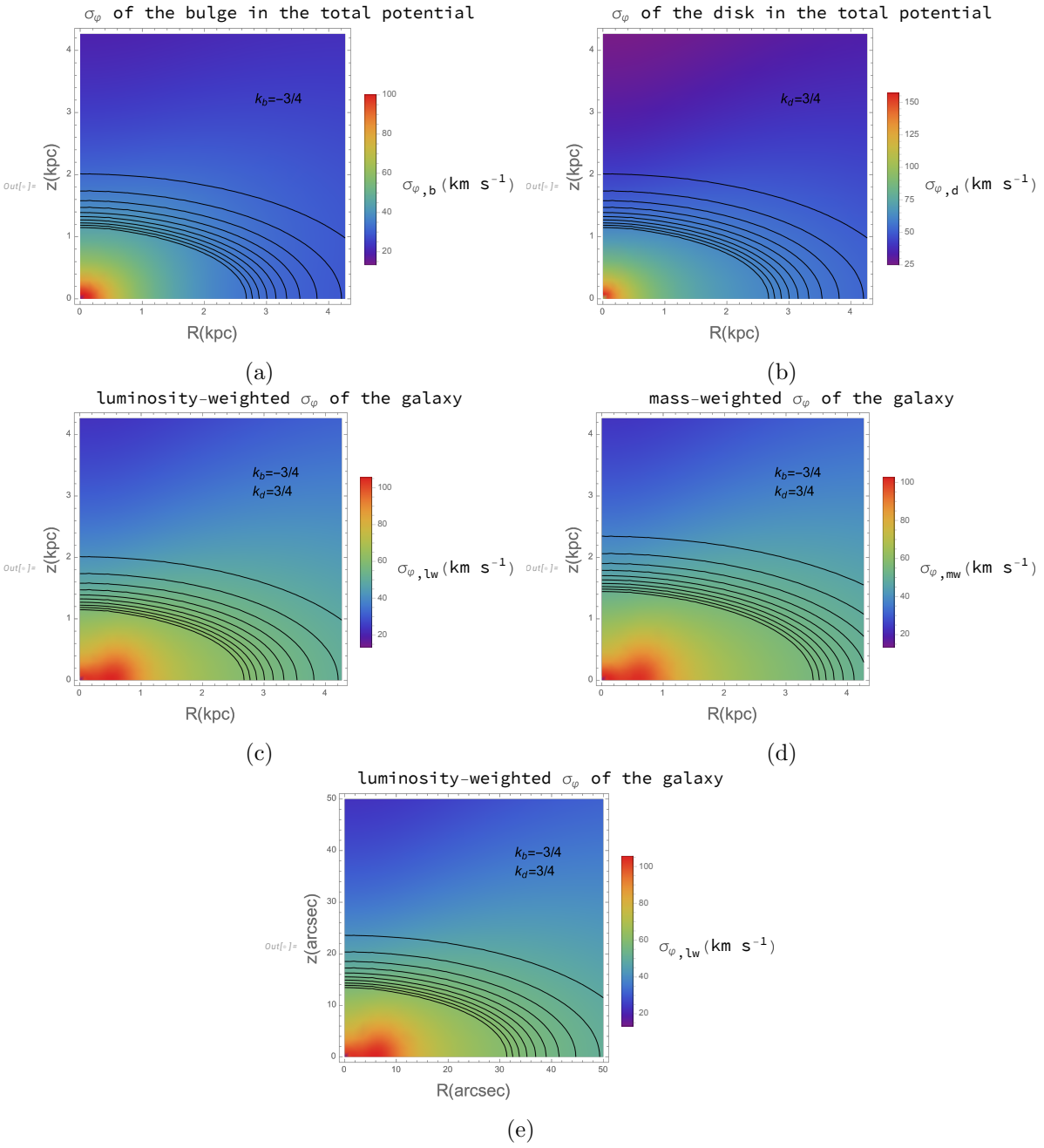

Figure 4.16: As in Figure 4.13 but for the moderately counter-rotating model ($k_{\rm b} = -3/4$, $k_{\rm d} = 3/4$).

is too close with respect to the observations. Adopting the mildly counter-rotating model both moves the σ_φ peak outward and expands it. However, the maximally counter-rotating model predicts the decrease of σ_φ in the outskirts that we observe in the integral-field spectroscopic images, while in the mildly counter-rotating case the σ_φ remains high even far from the center. Lastly, while the model exhibits a negative peak at the origin, this feature is absent in the observational data.

All this leads us to believe that:

- the larger values of both $\sigma_{\rm LOS}$ and $v_{\rm LOS}$ are due to the fact that we should account for a

DM halo, which is not yet included in our model;

- the discrepancy in the central σ_{LOS} values between observations and models could be partially due to the fact that we have not yet projected the fields along the LOS;
- the mismatch between the position of the peaks in the observations and models suggests that we likely need to consider a generalized Satoh parameter, which depends on both R and z.

4.6 Comparison between models and long-slit spectroscopic observations

Since long-slit spectroscopic observations are available, we extract the radial profiles of modelled $\overline{v_\varphi}$ and σ_φ along the major axis of the galaxy. Here, we restrict to counter-rotating models only. In the following, we consider the maximally, mildly, and moderately counter-rotating models.

Figure 4.17 shows the $\overline{v_\varphi}$ radial profiles extracted along the major axis ($z = 0$) of the galaxy. Each of the three columns is characterized by different values of the Satoh parameter. In particular, from left to right we encounter the maximally, mildly, and moderately counter-rotating model, respectively. The four rows show, from top to bottom, the $\overline{v_\varphi}$ radial profile of the bulge and disk in the total potential, the luminosity- and the mass-weighted radial profiles. Furthermore, the observational values taken from the bottom panel of Figure 2.4 are shown for better comparison. We analyze the left-hand side of the observed rotation curve, symmetrizing the point vector relative to the origin since our model is symmetric about the z-axis.

On the other hand, Figure 4.18 shows the σ_φ radial profiles extracted along the major axis of the galaxy. Each of the three columns is characterized by different values of the Satoh parameter. In particular, from left to right we consider the maximally, mildly, and moderately counter-rotating model, respectively. The four rows show, from top to bottom, the σ_φ radial profile of the bulge and disk in the total potential, the luminosity- and mass-weighted radial profiles. Furthermore, the observational values taken from the top panel of Figure 2.4 are shown for better comparison. We analyze the left-hand side of the observed velocity dispersion curve, symmetrizing the point vector relative to the origin since our model is symmetric about the z-axis.

Since we are observing the equatorial plane of an edge-on system, σ_φ is not the only component of σ that we see, unlike v. In fact, σ_R and σ_φ are mixed when we observe the equatorial plane. Therefore, the resulting σ will be a combination of the two. Therefore, we can introduce the square root of the sum of σ_φ^2 and σ_R^2. This can be done for both the luminosity- and mass-weighted fields. This combination is not really a projection or sum formula, but it can give an idea of how the fields combine. This new quantity can then be compared to the observed values, again remembering that for a proper comparison we should project the fields along the LOS. Figure 4.19 shows the $\sqrt{\sigma_\varphi^2 + \sigma_R^2}$ radial profiles extracted along the major axis of the galaxy. Each of the three rows is characterized by different values of the Satoh parameter. In particular, from top to bottom we consider the maximally, mildly, and moderately counter-rotating model, respectively. The two columns show, from left to right, the luminosity- and mass-weighted $\sqrt{\sigma_\varphi^2 + \sigma_R^2}$ radial profiles. Furthermore, the observational values taken from the top panel of Figure 2.4 are shown for better comparison. We analyze the left-hand side of the observed velocity dispersion curve, symmetrizing the point vector relative to the origin since our model is symmetric about the z-axis. The peaks in the σ profile show a sharp increase. This combination, with all its limitations, provides a better fit to the observed values.

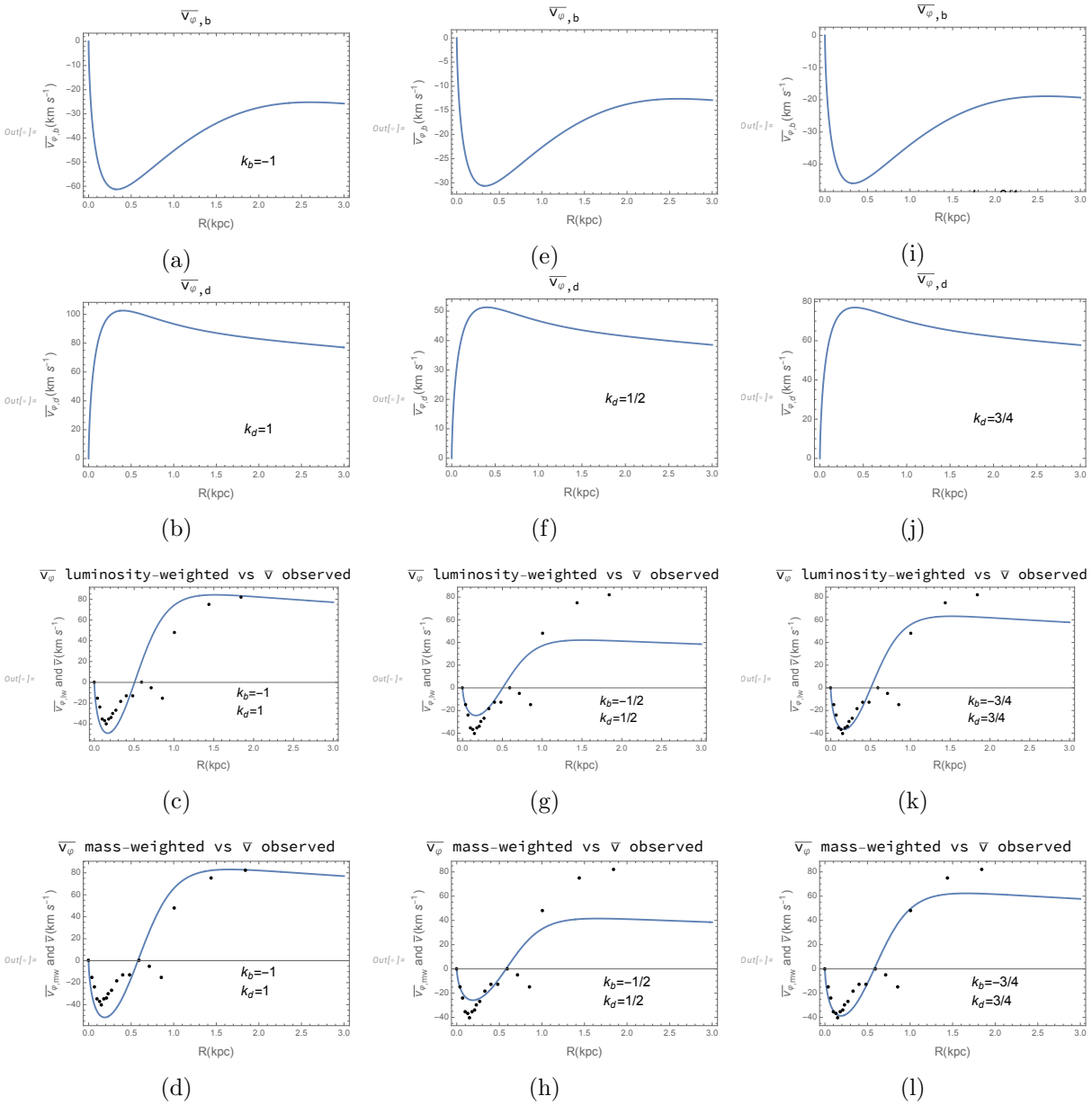

Figure 4.17: $\overline{v_\varphi}$ radial profiles along the major axis of NGC 1366 for the bulge (first row), disk (second row), galaxy weighted by luminosity (third row), and galaxy weighted by mass (fourth row) for the maximally ($k_\mathrm{b} = -1$, $k_\mathrm{d} = 1$, first column), mildly ($k_\mathrm{b} = -1/2$, $k_\mathrm{d} = 1/2$, second column), and moderately ($k_\mathrm{b} = -3/4$, $k_\mathrm{d} = 3/4$, third column) counter-rotating model. Black filled circles [●] and blue solid curves [—] correspond to data from Morelli et al. (2008) and models, respectively.

As stated in Section 4.5, while the observed profiles show v and σ along the LOS, our models predict $\overline{v_\varphi}$ and σ_φ, meaning the azimuthal components of the fields. This does not represent a limitation since $\overline{v_R} = \overline{v_z} = 0$ km s^{-1} in the velocity case; nevertheless, $\sigma_\varphi \neq \sigma_\mathrm{LOS}$ since in general $\sigma_R = \sigma_z \neq 0$ km s^{-1}. This is why we introduce $\sqrt{\sigma_\varphi^2 + \sigma_R^2}$. Although it does not really correspond to how the two fields actually combine, its comparison with observational data is still useful to get a general idea of the strengths and weaknesses of our models.

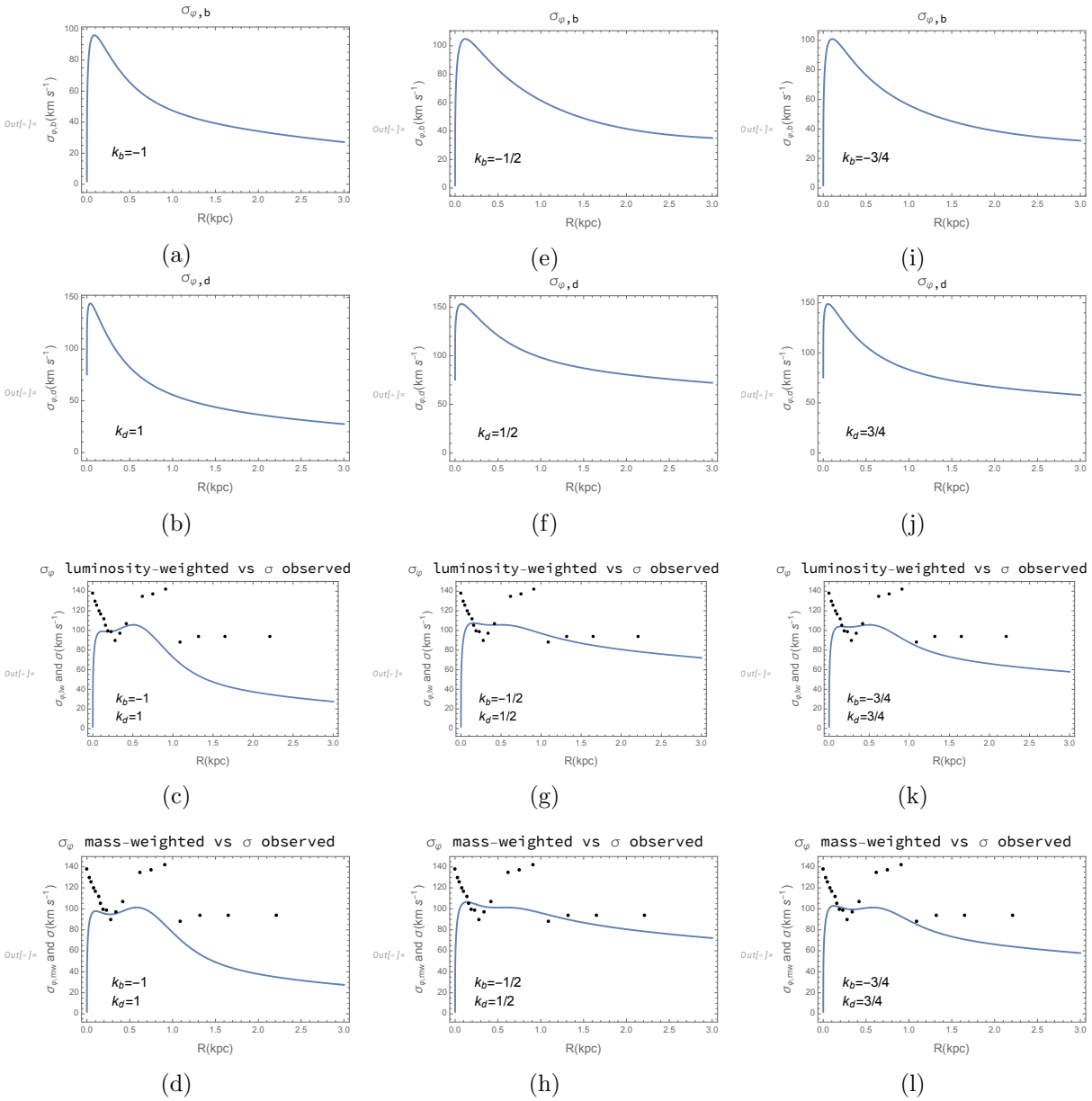

Figure 4.18: As in Figure 4.17 but for σ_φ.

The radial profile of $\overline{v_\varphi}$ clearly displays the presence of two peaks, which are the hallmark of counter-rotation as discussed in Section 1.2 and they are visible in the bottom panel of Figure 2.4. However, the two peaks in the models are not positioned at the observed distance. Moreover, the $v_{\rm LOS}$ radial profile is quite different from the modelled one. It decreases at small radii, and shows a minimum. Then it does not immediately become positive as in the model, but it makes a small negative oscillation at $R \simeq 0.7$ kpc, and outwards it steeply rises to reach positive values. The model does not show this central oscillation at all. Thus, the disk initially seems to corotate with the galaxy. Outwards, it undergoes a transition or settling phase into counter-rotation between 0.5 and 1 kpc, after which the counter-rotating component starts to dominate. Furthermore, considering Figures 4.17c, 4.17g, and 4.17k, the moderately counter-rotating model better reproduces the negative peak at $R \simeq 0.2$ kpc, but fails to fit the points at large R. On the other hand, the maximally counter-rotating model reproduces the

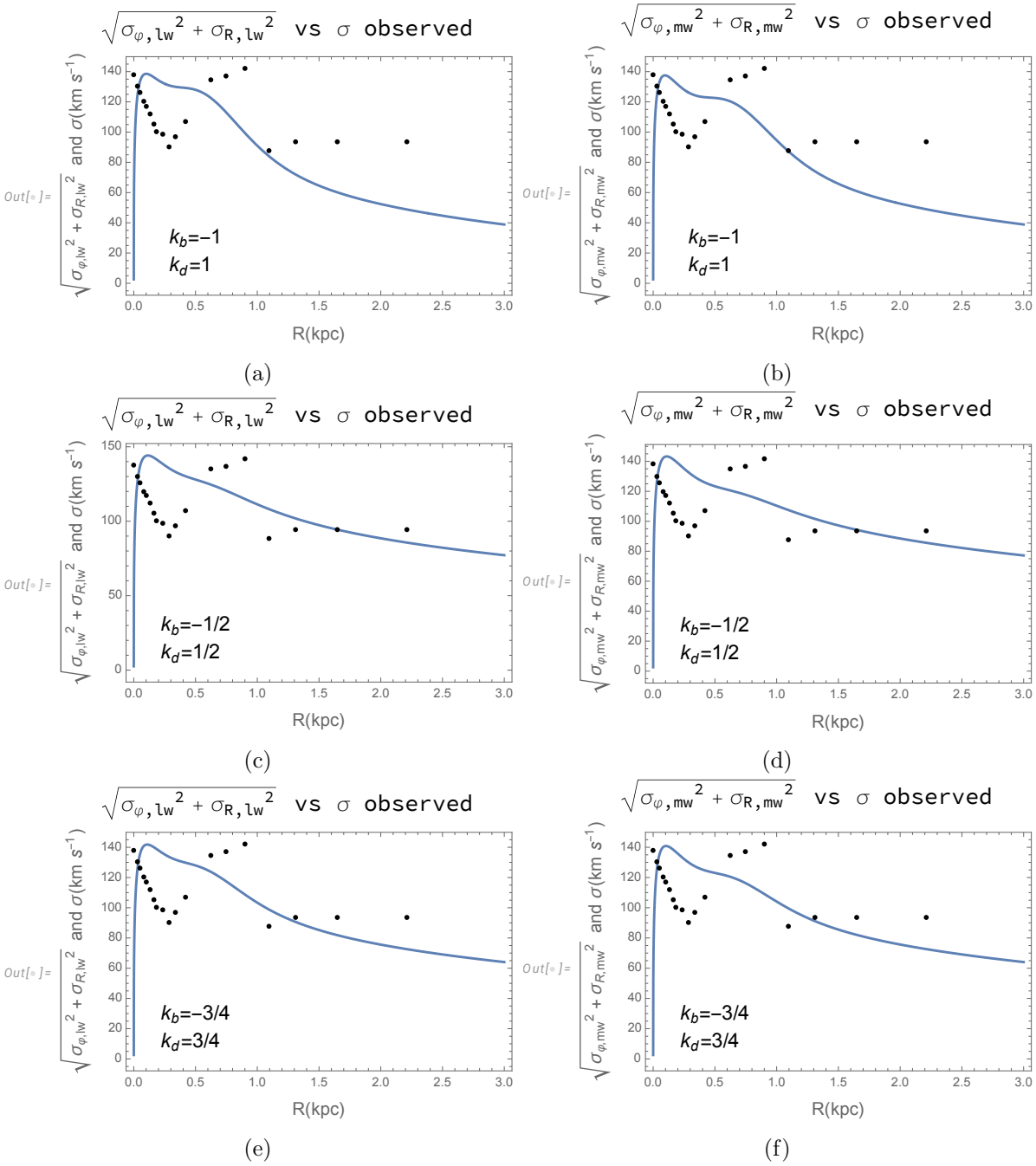

Figure 4.19: $\sqrt{\sigma_\varphi^2 + \sigma_R^2}$ radial profiles along the major axis of NGC 1366 for the galaxy weighted by luminosity (first column), and galaxy weighted by mass (second column) for the maximally ($k_\mathrm{b} = -1$, $k_\mathrm{d} = 1$, first row), mildly ($k_\mathrm{b} = -1/2$, $k_\mathrm{d} = 1/2$, second row), and moderately ($k_\mathrm{b} = -3/4$, $k_\mathrm{d} = 3/4$, third row) counter-rotating model. Black filled circles [●] and blue solid curves [—] correspond to data from Morelli et al. (2008) and models, respectively.

v_LOS increase at large R quite well, but fails to fit the observed data at small radii. This suggests that we should use a generalized Satoh parameter to reproduce this peculiar behaviour.

The interpretation of $\sqrt{\sigma_\varphi^2 + \sigma_R^2}$ is even more complicated than the previous one. Nevertheless, some interesting insights are deduced from the comparison of models and observations. In all

three models, the two peaks are present coherently with what shown by observations in the top panel of Figure 2.4, and their intensity is quite approximated by the model, especially for the first peak. However, the position of these maxima in the models does not coincide with the observed one. The decrease of $|k|$ spreads and moves the second peak outwards, but its intensity decreases despite what happens in the observed case. Therefore, the relative intensity of the two peaks is better reproduced by the moderately counter-rotating model, whereas the data at large R are better fitted by the mildly counter-rotating model. In fact, despite the absence of a DM halo, our model is able to reproduce quite well the observed value at large R. However, the region examined in the radial profiles is narrower than the area covered by the maps. Specifically, the radial profiles only account for the inner regions ($\lesssim 3$ kpc), whereas the maps extend up to $\simeq 4.5$ kpc. Furthermore, the central depression of $\sqrt{\sigma_\varphi^2 + \sigma_R^2}$ can be justified by the fact that we should project σ onto the sky plane in order to make a consistent comparison between the models and observations.

All this leads us to believe that:

- since both the v and σ values are reproduced at large R, as far as the inner regions of the galaxy (up to $\lesssim 3$ kpc) concern, the DM halo is irrelevant;
- the combination $\sqrt{\sigma_\varphi^2 + \sigma_R^2}$ is only a rough estimate of how σ_φ and σ_R combine. To provide a consistent comparison we should project the fields along the LOS;
- the fact that we are not able to reproduce the peaks and troughs of the observed σ is due to the fact that we are considering constant Satoh parameters. Therefore, to better improve our model we should consider a generalized Satoh parameter, which should depend on both R and z.

Chapter 5

Discussion and conclusions

In this chapter we summarize the results of our work, and discuss its possible future developments. In Section 5.1 we summarize the conclusions drawn from the comparison between observations and models, along with suggestions for possible improvements. In Section 5.2 we outline prospective directions for extending this work.

5.1 Discussion of the results

In this thesis we provide a tentative dynamical model to describe the stellar counter-rotation within the edge-on S0 galaxy NGC 1366. After presenting the photometric and kinematic data of NGC 1366, we source within the galactic dynamics and stellar hydrodynamics to build our model. We introduce the CBE and JEs, write them in cylindrical coordinates, and finally solve them for isotropic axisymmetric systems. We assume the galaxy to be made by a bulge and a disk with a spheroidal mass distribution and having surface brightness distribution parametrized with a Sérsic and a Type I Freeman law, respectively. To disentangle random and ordered motions we use the Satoh decomposition. The Satoh parameters are assumed to be constant. We then solve the JEs for the NGC 1366 structural parameters. We calculate the distribution maps of the vertical velocity dispersion σ_z, difference between the mean square azimuthal velocity and vertical velocity dispersion Δ_σ, and mean square azimuthal velocity $\overline{v_\varphi^2}$. We consider five different models, characterized by five different values of the Satoh parameters: the non-rotating galaxy model ($k_\mathrm{b} = 0$, $k_\mathrm{d} = 0$), non-rotating bulge model ($k_\mathrm{b} = 0$, $k_\mathrm{d} = 1$), maximally counter-rotating model ($k_\mathrm{b} = -1$, $k_\mathrm{d} = 1$), mildly counter-rotating model ($k_\mathrm{b} = -1/2$, $k_\mathrm{d} = 1/2$), and moderately counter-rotating model ($k_\mathrm{b} = -3/4$, $k_\mathrm{d} = 3/4$). We obtain the distribution maps of the mean azimuthal velocity $\overline{v_\varphi}$ and azimuthal velocity dispersion σ_φ of each model. We extract the radial profiles of $\overline{v_\varphi}$ and σ_φ along the major axis of each model. We introduce a combination of σ_φ and σ_R to simulate how the different velocity dispersion components combine. Finally, we compare observations with the results of our models.

The conclusions drawn from the comparison between observations and models can be summarized as follows:

1. while $\overline{v_\varphi} = v_\mathrm{LOS}$ for construction, comparing σ_LOS with σ_φ requires projecting the model kinematics field along the LOS. Despite this, analyzing σ_φ and $\sqrt{\sigma_\varphi^2 + \sigma_R^2}$ can still provide valuable insights into the overall strengths and limitations of our modelling method;

2. no model is able to fully fit the galaxy kinematics. In fact, different regions of the galaxy are fitted by different models characterized by different Satoh parameters. This is most obvious when looking at the field radial profiles of $\overline{v_\varphi}$ and σ_φ;

3. while the radial profiles of $v_{\rm LOS}$ and $\sigma_{\rm LOS}$ are well fitted at large radii, the distribution maps of $\overline{v_\varphi}$ and σ_φ show that the models struggle to reproduce the observed $v_{\rm LOS}$ and $\sigma_{\rm LOS}$ at these distances. Since the spatial extent of the maps is larger than that of the radial profiles, this suggests that the DM halo has little influence in the inner regions of the galaxy ($R \lesssim 3$ kpc) and becomes more significant in the outskirts.

Therefore, the following steps can be taken for further refinement of our model:

1. *projection of σ along the LOS.* In the edge-on configuration, we have for each component i:

$$\sigma^2_{{\rm LOS},i} = \underbrace{\sigma^2_{{\rm P},i} + V^2_{{\rm P},i}}_{V^2_{{\rm rms},i}} - v^2_{{\rm LOS},i} = V^2_{{\rm rms},i} - v^2_{{\rm LOS},i} \quad , \tag{5.1}$$

   from Caravita et al. (2021), where $V_{{\rm rms},i} = \sigma^2_{{\rm P},i} + V_{{\rm P},i}$ and:

$$\Sigma_{\star,i} = 2\int_y^\infty \frac{\rho_{\star,i} R}{\sqrt{R^2-y^2}} dR \quad , \tag{5.2}$$

$$\Sigma_{\star,i}\sigma^2_{{\rm P},i} = 2\int_y^\infty \frac{(R^2-y^2)\sigma_i^2 + y^2\sigma^2_{\varphi,i}}{R\sqrt{R^2-y^2}} dR \quad , \tag{5.3}$$

$$\Sigma_{\star,i}V^2_{{\rm P},i} = 2y^2\int_y^\infty \frac{\rho_{\star,i}\,\overline{v_{\varphi,i}}^2}{R\sqrt{R^2-y^2}} dR \quad , \tag{5.4}$$

   following Cappellari (2008), with:

$$\Sigma_\star = \sum_i \Sigma_{\star,i} \quad , \quad v_{\rm LOS} = \frac{\sum_i \Sigma_{\star,i}\, v_{{\rm LOS},i}}{\Sigma_\star} \quad , \quad V^2_{\rm rms} = \frac{\sum_i \Sigma_{\star,i}\, V^2_{{\rm rms},i}}{\Sigma_\star} \quad . \tag{5.5}$$

   This approach significantly increases the computational cost of the code, but it allows for a more robust comparison between the model and observations;

2. *adopting a generalized Satoh parameter.* As shown by Ciotti & Pellegrini (1996), the original Satoh decomposition (Satoh 1980) can be generalized to assume $k(R,z)$. We can start by defining an upper limit $k^2_{\rm max}(R,z)$, corresponding to maximally rotating models with no net velocity dispersion in the azimuthal direction. This is obtained from Equation (3.37) by imposing $\sigma_\varphi = 0$ everywhere:

$$k^2_{\rm max}(R,z) = \frac{\Delta_\sigma + \sigma_z}{\Delta_\sigma} \overset{\Delta_\sigma = \overline{v^2_\varphi} - \sigma^2_z}{=} \frac{\overline{v^2_\varphi}}{\Delta_\sigma} \quad . \tag{5.6}$$

   In this case, the density flattening is fully supported by the azimuthal velocity $\overline{v_\varphi}$. Thus, the following relation must hold:

$$k^2(R,z) \leq k^2_{\rm max}(R,z) \quad . \tag{5.7}$$

   Furthermore, for a given multicomponent system it is also possible to assume a Satoh decomposition for some components and a generalized decomposition for the others. This is likely to be the case for NGC 1366: the bulge can be modeled with a constant Satoh parameter, whereas the Satoh parameter for the disk would vary with distance from the galactic center. This setup allows the disk to corotate with the bulge up to a certain radius, beyond which the counter-rotation begins to dominate;

3. *addition of a DM halo.* A DM halo can be added without much difficulty. Both the total potential and total density should then be modified as follows:

$$\Phi_{\rm tot} = \Phi_{\rm b} + \Phi_{\rm d} + \Phi_{\rm halo} \quad , \quad \rho_{\rm tot} = \rho_{\rm b} + \rho_{\rm d} + \rho_{\rm halo} \quad . \tag{5.8}$$

The functional form of the DM halo can be chosen among the ones presented in Section 3.3.2. Furthermore, the DM halo parameters can be taken from Mazzei et al. (2019).

5.2 Future perspectives

In our exploratory work we present a simplified dynamical model of NGC 1366. In fact, we do not consider the stellar population properties of the galaxy. To take this into account, the numerical code Jeans AxiSymmetric Models of galaxies IN Equilibrium 2 (JASMINE2, Caravita et al. 2021) can be used. This code is dedicated to the solution of the Jeans equations in axisymmetric multicomponent systems. Each stellar component is implicitly described by a two- or three-integral distribution function, and stellar components can have different structural (density profile, flattening, mass, scale length), dynamical (rotation, velocity dispersion anisotropy) and population (age, metallicity, initial mass function, mass-to-light ratio) properties. In addition, this code can include the presence of multiple stellar components, a central black hole, and a DM halo. Since this code is very computationally expensive and time consuming, the two-integral dynamical model of NGC 1366 that we built can be used to calibrate JASMINE2.

Moreover, the case of NGC 1366 represents a pilot project to fine tune JASMINE2 modeling in order to dissect counter-rotating disk galaxies, derive the stellar population properties of their kinematically-decoupled components, and finally constrain their formation mechanism. The application of both kinematic decomposition and dynamical modeling can be very important for future applications in this direction. Once the dynamical model for NGC 1366 has been refined, a similar procedure can be carried out for other galaxies whose kinematic decoupling is known. From the fine-tuning of the model through the known counter-rotating galaxies we can build a powerful method able to predict and study the structure of a vaste number of cases.

Using the kinematic diagnostics by Rubino et al. (2021) we can identify the counter-rotating disk galaxies in the ATLAS3D (Cappellari et al. 2011), CALIFA (Sánchez et al. 2012), MANGA (Bundy et al. 2015), and MUSE-based (e.g. Sarzi et al. 2018; Gadotti et al. 2019) surveys. Then, JASMINE2 models of the selected galaxies can be built to constrain the structural, dynamical, and population parameters, and derive the formation epoch and timescale of the two counter-rotating components. Finally, the frequency of strong and weak stellar counter-rotation in S0 and spiral galaxies can be addressed, looking for relations with the properties of the host galaxies, and identifying the most common formation mechanism.

Appendix A

Luminosity of bulge and disk

We derive the total luminosity for the Sérsic and Freeman profiles, which are important in several parts of our code, especially when converting to astrophysical units.

Let us restrict ourselves to the case of circularized isophotes, taking into account the apparent flattening q. Being $d\Omega$ the infinitesimal solid angle and $\Omega_f = r_\mathrm{e}^2 l_f \theta_f$ and $\Omega_g = r_\mathrm{e}^2 l_g \theta_g$ two arbitrary solid angles, we define the integrated luminosity L as:

$$L = \int_{\Omega_f}^{\Omega_g} I \, d\Omega \quad \overset{d\Omega = r_\mathrm{e}^2 \, l \, dl \, d\theta}{=} \quad r_\mathrm{e}^2 \int_{l_f}^{l_g} \int_{\theta_f}^{\theta_g} I \, l \, dl \, d\theta \quad . \tag{A.1}$$

If we extend this integral to the whole space we get the total luminosity L_tot.

Starting with the bulge, substituting Equation (2.5) $I_\mathrm{b}(l) = I_0 e^{-b_n \, l^{\frac{1}{n}}}$, with $l = (\sqrt{R^2 + \frac{z^2}{q_\mathrm{b}^2}})/r_\mathrm{e}$, inside Equation (A.1), and extending the integral to the whole space, we get the total luminosity of the bulge:

$$\begin{aligned} L_\mathrm{b} &= \int_0^{4\pi} I_\mathrm{b} \, d\Omega = r_\mathrm{e}^2 \int_0^{\infty} \int_0^{2\pi} I \, l \, dl \, d\theta = 2\pi q_\mathrm{b} r_\mathrm{e}^2 \int_0^{\infty} I_\mathrm{b} \, l \; dl \overset{(2.5)}{=} \\ &= 2\pi q_\mathrm{b} r_\mathrm{e}^2 \int_0^{\infty} I_0 \, l \, e^{-b_n \, l^{\frac{1}{n}}} \, dl \overset{(a)}{=} 2\pi q_\mathrm{b} r_\mathrm{e}^2 I_0 \int_0^{\infty} \frac{s^n}{b_n^n} e^{-s} \frac{n}{b_n^n} s^{n-1} \, ds = \\ &= 2\pi q_\mathrm{b} r_\mathrm{e}^2 I_0 \frac{n}{b_n^{2n}} \underbrace{\int s^{2n-1} e^{-s} \, ds}_{\Gamma(2n)} \overset{I_0 = I_\mathrm{e} e^{b_n}}{=} 2\pi q_\mathrm{b} r_\mathrm{e}^2 I_\mathrm{e} e^{b_n} n \frac{\Gamma(2n)}{b_n^{2n}} \quad , \end{aligned} \tag{A.2}$$

where in (a) we used the change of variables:

$$s = b_n l^{\frac{1}{n}} \implies \frac{s^n}{b_n^n} = l \implies \frac{n}{b_n^n} s^{n-1} \, ds = dl \quad . \tag{A.3}$$

Γ is the Euler Gamma function $\Gamma(z) = \int_0^{\infty} t^{z-1} e^{-t} \, dt$.

For the disk the procedure is analogous. Substituting Equation (2.9) $I_\mathrm{d}(l) = I_0 e^{-l}$, with $l = (\sqrt{R^2 + \frac{z^2}{q_\mathrm{d}^2}})/h$, inside Equation (A.1), and extending the integral to the whole space, we get the total luminosity of the disk:

$$\begin{aligned} L_\mathrm{d} &= \int_0^{4\pi} I_\mathrm{d} \, d\Omega = h^2 \int_0^{\infty} \int_0^{2\pi} I \, l \, dl \, d\theta = 2\pi q_\mathrm{d} h^2 \int_0^{\infty} I_\mathrm{d} \, l \; dl \overset{(2.9)}{=} \\ &= 2\pi q_\mathrm{d} h^2 \int_0^{\infty} I_0 e^{-l} \, dl = 2\pi q_\mathrm{d} h^2 I_0 \left[-e^{-l} \right]_0^{\infty} = 2\pi q_\mathrm{d} h^2 I_0 \quad . \end{aligned} \tag{A.4}$$

Note that Equation (A.4) can be obtained from Equation (A.2) by substituting $h = \frac{h_e}{b_1}$ and $n = 1$, being aware that $\Gamma(2) = 1$ and $I_0 = I_e e^{b_n}$. Therefore, we will refer just to Equation (A.2), which we rewrite:

$$L = \frac{2\pi q_b n}{b_n^{2n}} \Gamma(2n) I_e r_e^2 \quad . \tag{A.5}$$

Appendix B

Abel integration for an edge-on spheroidal system

We derive the Abel integration for an edge-on spheroidal system.

Let us consider a spheroidal system of luminosity surface density I and luminosity volume density j seen edge on. Let us refer to Figure B.1 and define a Cartesian coordinate system with the origin in the center of the system, x being parallel to the LOS and pointing toward the observer, z being the symmetry axis of the system and pointing upward, and y being perpendicular to x and z so that (x, y, z) forms a right-handed system. Let q be the intrinsic flattening of the system. Let us consider a point P located at a distance $l = \sqrt{R^2 + \frac{z^2}{q^2}}$ from the center of the system, where we defined $R^2 = x^2 + y^2$. Then, P appears to be projected in a point P' onto the sky plane, which is located at a distance $l' = \sqrt{R'^2 + \frac{z^2}{q^2}}$ from the center of the system. Let us call s the distance $\overline{PP'}$, and ds the infinitesimal displacement along the LOS. Then, I and j are related by the infinitesimal equation:

$$dI = j ds \quad , \tag{B.1}$$

which, once integrated, writes:

$$I = \int_{-\infty}^{\infty} j ds \overset{(a)}{=} 2 \int_{0}^{\infty} j ds \quad , \tag{B.2}$$

where in (a) we used the fact that the system is symmetric with respect to the sky plane. Then, since z does not vary being the system seen edge on, we have:

$$s = \sqrt{l^2 - l'^2} = \sqrt{R^2 + \frac{\cancel{z^2}}{\cancel{q^2}} - R'^2 - \frac{\cancel{z^2}}{\cancel{q^2}}} = \sqrt{R^2 - R'^2} \implies ds = \frac{R}{\sqrt{R^2 - R'^2}} dR \quad , \tag{B.3}$$

with $s = 0 \implies R = R'$, and $s = \infty \implies R = \infty$. Then, doing the change of coordinates from s to R inside Equation (B.2), we get:

$$I = 2 \int_{R'}^{\infty} j \frac{R}{\sqrt{R^2 - R'^2}} dR \quad . \tag{B.4}$$

This equation can be inverted with an Abel integration to go from I to j. In particular, we have:

$$j = -\frac{1}{\pi} \int_{R}^{\infty} \frac{dI}{dR'} \frac{dR'}{\sqrt{R'^2 - R^2}} \quad . \tag{B.5}$$

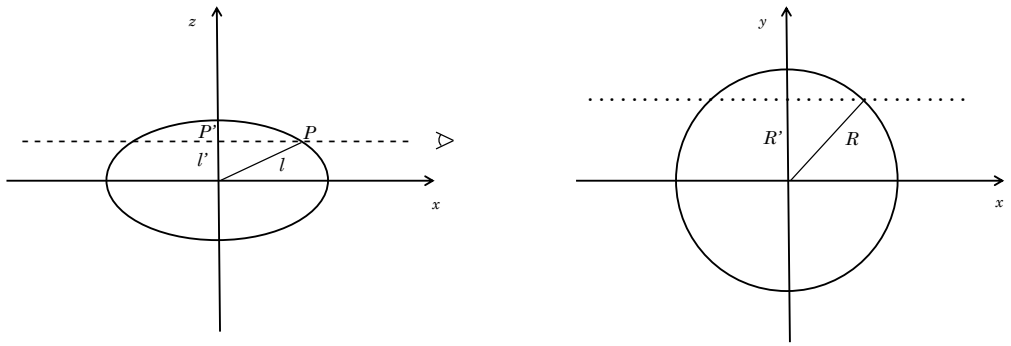

Figure B.1: Scheme of the Abel integration of an edge-on spheroidal system. Left panel: section of the $y = 0$ plane. The black dashed line [- -] represents the LOS. Right panel: section of the equatorial $z = 0$ plane. The black dotted line [· ·] represents the projection of the LOS onto the equatorial plane.

We now want to go back to spheroidal coordinates l and l'. To the first term in Equation (B.5) we can apply the chain rule:

$$\frac{dI}{dR} = \frac{dI}{dl}\frac{dl}{dR} \quad . \tag{B.6}$$

Moreover, substituting back l and l' with Equation (B.3), we finally obtain:

$$j = -\frac{1}{\pi}\int_l^\infty \frac{\partial I}{\partial l'}\frac{dl'}{\sqrt{l'^2 - l^2}} \quad . \tag{B.7}$$

Appendix C

Collisionless Boltzmann equation

We derive the *collisionless Boltzmann equation* (CBE). For a complete overview on the topic see the books by Binney & Tremaine (1987, 2008) and Ciotti (2021) among the others. We refer more closely to Binney & Tremaine (2008) for our discussion.

Let us consider a collisionless system. Then, we can define the distribution function (DF) f such that $f(\vec{x},\vec{v},t)d^3\vec{x}d^3\vec{v}$ is the probability of finding a randomly chosen star at time t with position in between $\vec{x}$ and $\vec{x}+d\vec{x}$ and velocity in between $\vec{v}$ and $\vec{v}+d\vec{v}$. This probability is the same for all stars in the system, since we assume that all stars are identical. Therefore, f is normalized such that:

$$\int_{\mathbb{R}^6} f(\vec{x},\vec{v},t)d^3\vec{x}d^3\vec{v} = 1 \quad , \tag{C.1}$$

where the integral is over the all phase space.

Let $\vec{w} = (\vec{x},\vec{v})$ an arbitrary system of canonical coordinates. Any given star moves through phase space, so the probability of finding it at any given phase-space location evolves with time. As f evolves, probability must be conserved. We can use an analogy between the probability conservation and the mass conservation for a fluid, which is given by:

$$\frac{\partial\rho}{\partial t} + \frac{\partial}{\partial\vec{x}}(\rho\dot{\vec{x}}) = 0 \quad , \tag{C.2}$$

where ρ and $\dot{\vec{x}}$ are the density and velocity of the fluid, respectively. Analogously, the equation for the conservation of probability in phase space is:

$$\frac{\partial f}{\partial t} + \frac{\partial}{\partial\vec{w}}(f\dot{\vec{w}}) = 0 \quad . \tag{C.3}$$

We can now use Hamilton's equations (e.g., Goldstein et al. 2002 among the others):

$$\dot{\vec{q}} = \frac{\partial H}{\partial\vec{p}} \quad , \tag{C.4}$$

$$\dot{\vec{p}} = -\frac{\partial H}{\partial\vec{q}} \quad , \tag{C.5}$$

where H is the Hamiltonian of the system:

$$H(\vec{p},\vec{q},t) \coloneqq \vec{p}\,\dot{\vec{q}} - \mathcal{L}(\vec{q},\dot{\vec{q}},t) \quad , \tag{C.6}$$

and $\mathcal{L}$ is the Lagrangian of the system, defined as the difference between the kinetic and potential energy. Therefore, remembering that $\dot{\vec{w}} = (\dot{\vec{q}},\dot{\vec{p}})$, we can rewrite the second term in Equation

(C.3) as:

$$\begin{aligned}
\frac{\partial}{\partial \vec{w}}(f\dot{\vec{w}}) &= \frac{\partial}{\partial \vec{q}}(f\dot{\vec{q}}) + \frac{\partial}{\partial \vec{p}}(f\dot{\vec{p}}) \overset{\text{Eqs.}(C.4) \text{ and } (C.5)}{=} \\
&= \frac{\partial}{\partial \vec{q}}\left(f\frac{\partial H}{\partial \vec{p}}\right) - \frac{\partial}{\partial \vec{p}}\left(f\frac{\partial H}{\partial \vec{q}}\right) = \\
&= \frac{\partial f}{\partial \vec{q}}\frac{\partial H}{\partial \vec{p}} + \cancel{f\frac{\partial^2 H}{\partial \vec{q}\partial \vec{p}}} - \frac{\partial f}{\partial \vec{p}}\frac{\partial H}{\partial \vec{q}} - \cancel{f\frac{\partial^2 H}{\partial \vec{p}\partial \vec{q}}} \overset{\text{Eqs.}(C.4) \text{ and } (C.5)}{=} \\
&= \dot{\vec{q}}\frac{\partial f}{\partial \vec{q}} + \dot{\vec{p}}\frac{\partial f}{\partial \vec{p}} \quad . \qquad \text{(C.7)}
\end{aligned}$$

Substituting Equation (C.7) inside Equation (C.3) we get the CBE:

$$\frac{\partial f}{\partial t} + \dot{\vec{q}}\frac{\partial f}{\partial \vec{q}} + \dot{\vec{p}}\frac{\partial f}{\partial \vec{p}} = 0 \quad . \qquad \text{(C.8)}$$

In terms of inertial Cartesian coordinates, H can be expressed in terms of the velocity v and the gravitational potential Φ_{tot} as $H = \frac{1}{2}v^2 + \Phi_{\text{tot}}(\vec{x}, t)$. Therefore, using Equation (C.8), the CBE becomes:

$$\frac{D\,f}{Dt} = \frac{\partial f}{\partial t} + \vec{v}\frac{\partial f}{\partial \vec{x}} - \frac{\partial \Phi_{\text{tot}}}{\partial \vec{x}}\frac{\partial f}{\partial \vec{v}} = \frac{\partial f}{\partial t} + \langle \vec{v}, \nabla_{\vec{x}} f\rangle - \langle \nabla_{\vec{x}}\Phi_{\text{tot}}, \nabla_{\vec{v}} f\rangle = 0 \quad , \qquad \text{(C.9)}$$

where $\frac{D}{Dt} = \frac{\partial}{\partial t} + \vec{v}\frac{\partial}{\partial \vec{x}}$ is the material derivative, $\nabla_{\vec{x}}$ and $\nabla_{\vec{v}}$ are the gradient operators over space and velocity, respectively, and $\langle \vec{a}, \vec{b}\rangle$ represents the inner product of the two vectors $\vec{a}$ and $\vec{b}$.

Appendix D

Jeans theorem

We derive the *Jeans Theorem*. For a complete overview on the topic see the books by Binney & Tremaine (1987, 2008) and Ciotti (2021) among the others. We refer more closely to Binney & Tremaine (1987) for our discussion.

Let us star with the definition of integral of motion. An integral of motion I is any function of the phase-space coordinates $\vec{x}$ and $\vec{v}$ alone that is constant along any stellar orbit for any time t:

$$I\left[\vec{x}(t_1), \vec{v}(t_1)\right] = I\left[\vec{x}(t_2), \vec{v}(t_2)\right] = const \quad \forall\, t_1, t_2 \implies \frac{dI\left[\vec{x}(t), \vec{v}(t)\right]}{dt} = 0 \quad . \tag{D.1}$$

For example in a static spherical potential the angular momentum $\vec{J}$ and energy E are integrals of motion.

Let now f be a steady state solution of the CBE (Equation 3.12). Then from Equation (C.9):

$$0 = \underbrace{\frac{\partial \cancel{f}}{\cancel{\partial t}}}_{\text{steady state}} + \vec{v}\frac{\partial f}{\partial \vec{x}} - \frac{\partial f}{\partial \vec{v}}\frac{\partial \Phi_{\text{tot}}}{\partial \vec{x}} = \frac{\partial f}{\partial \vec{x}}\frac{d\vec{x}}{dt} + \frac{\partial f}{\partial \vec{v}}\frac{d\vec{v}}{dt} = \frac{d}{dt} f(\vec{v}, \vec{x}) = 0 \quad , \tag{D.2}$$

which means that f is an integral of motion.

On the other hand, let f be a function of n integrals of motion. Let i be an index in between 1 and n. Then:

$$\frac{d}{dt} f(I_1, ..., I_n) = \frac{\partial f}{\partial I_i} \underbrace{\frac{d\cancel{I_i}}{\cancel{dt}}}_{=0} = 0 \quad , \tag{D.3}$$

where we used the definition of integral of motion. Therefore, f satisties the steady state CBE.

Therefore, putting together the results of Equations (D.2) and (D.3), we can state the *Jeans Theorem*: any steady state solution of the CBE depends on the phase-space coordinates only through integrals of motion in the given potential, and any function of the integrals yelds a steady-state solution of the CBE.

Appendix E

Jeans equations

We derive the *Jeans equations* (JEs). For a complete overview on the topic see the books by Binney & Tremaine (1987, 2008) and Ciotti (2021) among the others. We refer more closely to Ciotti (2021) for our discussion.

Being defined in the 6D phase-space, the CBE is not so useful to describe stellar system. In fact, we want an equation which depends on the observables of the system. Let us multiply the CBE, expressed by Equation (C.9), by a microscopic function $F = F(\vec{x}, \vec{v}, t)$. Then, let us integrate the product on velocities. Using vector components notation, we get:

$$\int_{\mathbb{R}^3} \frac{D\,f}{Dt} F d^3\vec{v} = \underbrace{\int_{\mathbb{R}^3} \frac{\partial f}{\partial t} F d^3\vec{v}}_{(A)} + \underbrace{\int_{\mathbb{R}^3} v_i \frac{\partial f}{\partial x_i} F d^3\vec{v}}_{(B)} - \underbrace{\int_{\mathbb{R}^3} \frac{\partial \Phi_{\text{tot}}}{\partial v_i} \frac{\partial f}{\partial v_i} F d^3\vec{v}}_{(C)} = 0 \quad . \tag{E.1}$$

Let us study independently each term. We have:

$$(A) = \int_{\mathbb{R}^3} \frac{\partial f}{\partial t} F d^3\vec{v} \overset{\text{by parts}}{=} \int_{\mathbb{R}^3} \left(\frac{\partial (fF)}{\partial t} - f \frac{\partial F}{\partial t} \right) d^3\vec{v} = \frac{\partial (\nu \overline{F})}{\partial t} - \nu \overline{\frac{\partial F}{\partial t}} \quad , \tag{E.2}$$

since time derivation and integration over $\vec{v}$ can be interchanged, being $\vec{v}$ independent on t. Moreover:

$$\begin{aligned} (B) = \int_{\mathbb{R}^3} v_i \frac{\partial f}{\partial x_i} F d^3\vec{v} = \int_{\mathbb{R}^3} \left(\frac{\partial}{\partial x_i}(v_i f F) - v_i f \frac{\partial F}{\partial x_i} - \cancel{f F \frac{\partial v_i}{\partial x_i}} \right) d^3\vec{v} = \\ = \frac{\partial}{\partial x_i}(\nu \overline{F v_i}) - \nu v_i \overline{\frac{\partial F}{\partial x_i}} \quad , \end{aligned} \tag{E.3}$$

since spacial derivation and integration over $\vec{v}$ can be interchanged, being $\vec{v}$ independent on $\vec{x}$. Finally:

$$\begin{aligned} (C) = \int_{\mathbb{R}^3} \frac{\partial \Phi_{\text{tot}}}{\partial x_i} \frac{\partial f}{\partial v_i} F d^3\vec{v} \overset{\text{by parts}}{=} \frac{\partial \Phi_{\text{tot}}}{\partial x_i} \int_{\mathbb{R}^3} \left(\cancel{\frac{\partial (fF)}{\partial v_i}} - f \frac{\partial F}{\partial v_i} \right) d^3\vec{v} = \\ = -\nu \frac{\partial \Phi_{\text{tot}}}{\partial x_i} \overline{\frac{\partial F}{\partial v_i}} \quad , \end{aligned} \tag{E.4}$$

since Φ_{tot} is independent of $\vec{v}$ and we assume $fF \to 0$ for $\|\vec{v}\| \to \infty$, which implies that the integration over the whole velocity space of the partial derivative with respect to v_i of that term evaluates to zero. Therefore, adding all together we get:

$$\frac{\partial (\nu \overline{F})}{\partial t} - \nu \overline{\frac{\partial F}{\partial t}} + \frac{\partial}{\partial x_i}(\nu \overline{F v_i}) - \nu v_i \overline{\frac{\partial F}{\partial x_i}} + \nu \frac{\partial \Phi_{\text{tot}}}{\partial x_i} \overline{\frac{\partial F}{\partial v_i}} = 0 \quad . \tag{E.5}$$

The first JE in Cartesian coordinates is obtained by choosing $F = 1$. In this case we get:

$$\frac{\partial \nu}{\partial t} + \frac{\partial}{\partial x_i}(\nu \overline{v_i}) = 0 \quad . \tag{E.6}$$

The second JE in Cartesian coordinates is obtained by choosing $F = v_j$. In this case we get:

$$\frac{\partial(\nu \overline{v_j})}{\partial t} + \frac{\partial}{\partial x_i}(\nu \overline{v_j v_i}) + \nu \frac{\partial \Phi_{\text{tot}}}{\partial x_j} = 0 \quad , \tag{E.7}$$

since $\vec{v}$ is independent of both t and $\vec{x}$, and since $\overline{\frac{\partial v_j}{\partial v_i}} = \delta_{ij}$.

The second JE can be rephrased as follows. If we subtract Equation (E.6) multiplied by $\overline{v_j}$ from Equation (E.7), we find:

$$\begin{aligned} &\frac{\partial(\nu \overline{v_j})}{\partial t} + \frac{\partial}{\partial x_i}(\nu \overline{v_j v_i}) + \nu \frac{\partial \Phi_{\text{tot}}}{\partial x_j} - \overline{v_j} \frac{\partial \nu}{\partial t} - \overline{v_j} \frac{\partial}{\partial x_i}(\nu \overline{v_i}) = 0 \\ &\implies \nu \frac{\partial \overline{v_j}}{\partial t} + \cancel{\overline{v_j} \frac{\partial \nu}{\partial t}} + \frac{\partial}{\partial x_i}(\nu \overline{v_j v_i}) + \nu \frac{\partial \Phi_{\text{tot}}}{\partial x_j} - \cancel{\overline{v_j} \frac{\partial \nu}{\partial t}} - \frac{\partial}{\partial x_i}(\nu \overline{v_j}\, \overline{v_i}) + \nu \overline{v_i} \frac{\partial \overline{v_j}}{\partial x_i} = 0 \quad . \end{aligned} \tag{E.8}$$

Using Equation (3.18) $\sigma_{ij} = \overline{v_i v_j} - \overline{v_i}\, \overline{v_j}$, dividing everything by ν, and redefining the indices, we get:

$$\frac{D\, \overline{v_i}}{Dt} = \frac{\partial\, \overline{v_i}}{\partial t} + \overline{v_j} \frac{\partial\, \overline{v_i}}{\partial x_j} = -\frac{\partial\, \Phi_{\text{tot}}}{\partial x_i} - \frac{1}{\nu} \frac{\partial}{\partial x_j}(\nu \sigma_{ij}^2) \quad , \tag{E.9}$$

where $\frac{D}{Dt}$ is the material derivative.

Appendix F

Jeans equations in cylindrical coordinates

We write the JEs in cylindrical coordinates. For a complete overview on the topic see the books by Binney & Tremaine (1987, 2008) and Ciotti (2021) among the others. We refer more closely to Binney & Tremaine (2008) for our discussion.

Let us rewrite Equation (C.9) in terms of the Hamiltonian H of the system for an arbitrary system of caninocal coordinates $\vec{w} = (\vec{q}, \vec{p})$:

$$0 = \frac{\partial f}{\partial t} + \frac{\partial f}{\partial \vec{q}}\frac{\partial H}{\partial \vec{p}} - \frac{\partial f}{\partial \vec{p}}\frac{\partial H}{\partial \vec{q}} \quad . \tag{F.1}$$

The Lagrangian $\mathcal{L}$ of the system in cylindrical coordinates (R, φ, z) takes the form:

$$\mathcal{L} = \frac{1}{2}[\dot{R}^2 + (R\dot{\varphi})^2 + \dot{z}^2] - \Phi_{\rm tot}(R, \varphi, z) \quad . \tag{F.2}$$

The momenta in cylindrical coordinates are $p_R = \dot{R}$, $p_\varphi = R^2\dot{\varphi}$, and $p_z = \dot{z}$. Therefore, from Equation (C.6) the Hamiltonian of the system takes the form:

$$\begin{aligned} H = \vec{p}\,\dot{\vec{q}} - \mathcal{L}(\vec{q}, \dot{\vec{q}}, t) &= \frac{1}{2}(\dot{R}^2 + R^2\dot{\varphi}^2 + \dot{z}^2) + \Phi_{\rm tot}(R, \varphi, z) = \\ &= \frac{1}{2}(p_R^2 + \frac{p_\varphi^2}{R^2} + p_z^2) + \Phi_{\rm tot}(R, \varphi, z) \quad , \end{aligned} \tag{F.3}$$

so that:

$$\frac{\partial H}{\partial \vec{q}} = \left(\frac{\partial \Phi_{\rm tot}}{\partial R} - \frac{p_\varphi}{R^3}, \frac{\partial \Phi_{\rm tot}}{\partial \varphi}, \frac{\partial \Phi_{\rm tot}}{\partial z}\right) \quad , \tag{F.4}$$

$$\frac{\partial H}{\partial \vec{p}} = \left(p_R, \frac{p_\varphi}{R^2}, p_z\right) \quad . \tag{F.5}$$

Therefore, Equation (F.1) becomes:

$$\frac{\partial f}{\partial t} + p_R\frac{\partial f}{\partial R} + \frac{p_\varphi}{R^2}\frac{\partial f}{\partial \varphi} + p_z\frac{\partial f}{\partial z} - \frac{\partial \Phi_{\rm tot}}{\partial R}\frac{\partial f}{\partial p_R} + \frac{p_\varphi^2}{R^3}\frac{\partial f}{\partial p_R} - \frac{\partial \Phi_{\rm tot}}{\partial \varphi}\frac{\partial f}{\partial p_\varphi} - \frac{\partial \Phi_{\rm tot}}{\partial z}\frac{\partial f}{\partial p_z} = 0 \quad . \tag{F.6}$$

Let us now assume that the system is in steady state and axisymmetric. This implies that $\frac{\partial}{\partial t}$ and $\frac{\partial}{\partial \varphi} = 0$, and that $\Phi_{\rm tot} = \Phi_{\rm tot}(R, z)$. Therefore, we get:

$$p_R\frac{\partial f}{\partial R} + p_z\frac{\partial f}{\partial z} - \frac{\partial \Phi_{\rm tot}}{\partial R}\frac{\partial f}{\partial p_R} + \frac{p_\varphi^2}{R^3}\frac{\partial f}{\partial p_R} - \frac{\partial \Phi_{\rm tot}}{\partial z}\frac{\partial f}{\partial p_z} = 0 \quad . \tag{F.7}$$

Let us now multiply Equation (F.7) by p_R and integrate it over the momenta $dp_R dp_\varphi dp_z$ knowing that $p_R = v_R$, $p_\varphi = R v_\varphi$, and $p_z = v_z$, and remembering that:

$$\int_{\mathbb{R}^3} f dv_R dv_\varphi dv_z = \nu \quad , \tag{F.8}$$

in analogy with the Cartesian case. Then we get:

$$\begin{aligned} 0 = &\int_{\mathbb{R}^3} p_R \frac{\partial f}{\partial R} p_R dp_R dp_\varphi dp_z + \int_{\mathbb{R}^3} p_z \frac{\partial f}{\partial z} p_R dp_R dp_\varphi dp_z - \int_{\mathbb{R}^3} \frac{\partial \Phi_{\text{tot}}}{\partial R} \frac{\partial f}{\partial p_R} p_R dp_R dp_\varphi dp_z + \\ &+ \int_{\mathbb{R}^3} \frac{p_\varphi^2}{R^3} \frac{\partial f}{\partial p_R} p_R dp_R dp_\varphi dp_z - \int_{\mathbb{R}^3} \frac{\partial \Phi_{\text{tot}}}{\partial z} \frac{\partial f}{\partial p_z} p_R dp_R dp_\varphi dp_z \\ \implies 0 = &\underbrace{\int_{\mathbb{R}^3} R v_R^2 \frac{\partial f}{\partial R} dv_R dv_\varphi dv_z}_{(A)} + \underbrace{\int_{\mathbb{R}^3} R v_z \frac{\partial f}{\partial z} v_R dv_R dv_\varphi dv_z}_{(B)} - \underbrace{\int_{\mathbb{R}^3} R \frac{\partial \Phi_{\text{tot}}}{\partial R} \frac{\partial f}{\partial v_R} v_R dv_R dv_\varphi dv_z}_{(C)} + \\ &+ \underbrace{\int_{\mathbb{R}^3} v_\varphi^2 \frac{\partial f}{\partial v_R} v_R dv_R dv_\varphi dv_z}_{(D)} - \underbrace{\int_{\mathbb{R}^3} R \frac{\partial \Phi_{\text{tot}}}{\partial z} \frac{\partial f}{\partial v_z} v_R dv_R dv_\varphi dv_z}_{(E)} \quad . \end{aligned} \tag{F.9}$$

Let us analyze each term separately, noting that each component of both $\vec{x}$ and $\vec{v}$ is independent. We have:

$$\begin{aligned} (A) \overset{\text{by parts}}{=} &\int_{\mathbb{R}^3} \frac{\partial}{\partial R}(f R v_R^2) dv_R dv_\varphi dv_z - \int_{\mathbb{R}^3} v_R^2 f \underbrace{\frac{\partial R}{\partial R}}_{=1} dv_R dv_\varphi dv_z - \\ &- \cancel{\int_{\mathbb{R}^3} f R \frac{\partial v_R^2}{\partial R} dv_R dv_\varphi dv_z} = R \frac{\partial}{\partial R}(\nu \overline{v_R^2}) - \nu \overline{v_R^2} \quad , \end{aligned} \tag{F.10}$$

and:

$$\begin{aligned} (B) \overset{\text{by parts}}{=} &R \int_{\mathbb{R}^3} \frac{\partial}{\partial z}(v_R v_z f) v_R dv_R dv_\varphi dv_z - \cancel{R \int_{\mathbb{R}^3} v_z f \frac{\partial v_R}{\partial z} v_R dv_R dv_\varphi dv_z} - \\ &- \cancel{\int_{\mathbb{R}^3} v_R f \frac{\partial v_z}{\partial z} v_R dv_R dv_\varphi dv_z} = R \frac{\partial}{\partial z}(\nu \overline{v_R v_z}) \quad , \end{aligned} \tag{F.11}$$

and:

$$\begin{aligned} (C) \overset{\text{by parts}}{=} &R \frac{\partial \Phi_{\text{tot}}}{\partial R} \int_{\mathbb{R}^3} \frac{\partial}{\partial v_R}(f v_R) dv_R dv_\varphi dv_z - R \frac{\partial \Phi_{\text{tot}}}{\partial R} \int_{\mathbb{R}^3} \underbrace{\frac{\partial v_R}{\partial v_R}}_{=1} f dv_R dv_\varphi dv_z = \\ &= \cancel{R \frac{\partial \Phi_{\text{tot}}}{\partial R} \frac{\partial}{\partial v_R}(\nu \overline{v_R})} - R \frac{\partial \Phi_{\text{tot}}}{\partial R} \nu \quad , \end{aligned} \tag{F.12}$$

since we assume $(f v_R) \to 0$ for $\|\vec{v}\| \to \infty$, which implies that the integration over the whole velocity space of the partial derivative with respect to v_R of that term evaluates to zero, and:

$$\begin{aligned} (D) \overset{\text{by parts}}{=} &\int_{\mathbb{R}^3} \frac{\partial}{\partial v_R}(f v_\varphi^2 v_R) dv_R dv_\varphi dv_z - \int_{\mathbb{R}^3} \underbrace{\frac{\partial v_R}{\partial v_R}}_{=1} (f v_\varphi^2) dv_R dv_\varphi dv_z - \\ &- \cancel{\int_{\mathbb{R}^3} \frac{\partial v_\varphi^2}{\partial v_R}(f v_R) dv_R dv_\varphi dv_z} = \cancel{\frac{\partial}{\partial v_R}(\nu \overline{v_\varphi^2 v_R})} - \nu \overline{v_\varphi^2} \quad , \end{aligned} \tag{F.13}$$

since we assume $(fv_\varphi^2 v_R) \to 0$ for $\|\vec{v}\| \to \infty$, which implies that the integration over the whole velocity space of the partial derivative with respect to v_R of that term evaluates to zero, and:

$$(E) \overset{\text{by parts}}{=} R\frac{\partial \Phi_{\text{tot}}}{\partial z}\int_{\mathbb{R}^3}\frac{\partial}{\partial v_z}(fv_R)dv_R dv_\varphi dv_z - \cancel{R\frac{\partial \Phi_{\text{tot}}}{\partial z}\int_{\mathbb{R}^3} f\frac{\partial v_R}{\partial v_z}dv_R dv_\varphi dv_z} = \\ = \cancel{R\frac{\partial \Phi_{\text{tot}}}{\partial z}\frac{\partial}{\partial v_z}(\nu\overline{v_R})} \quad , \tag{F.14}$$

since we assume $(fv_R) \to 0$ for $\|\vec{v}\| \to \infty$, which implies that the integration over the whole velocity space of the partial derivative with respect to v_z of that term evaluates to zero. Putting all back in Equation (F.9) and dividing everything by R, we get:

$$\frac{\partial}{\partial R}(\nu\overline{v_R^2}) - \nu\overline{v_R^2} + \frac{\partial}{\partial z}(\nu\overline{v_R v_z}) + \nu\left(\frac{\overline{v_R^2} - \overline{v_\varphi^2}}{R} + \frac{\partial \Phi_{\text{tot}}}{\partial R}\nu\right) = 0 \quad . \tag{F.15}$$

Analogously, when we multiply Equation (F.7) by p_z or p_φ rather than p_R, we obtain:

$$\frac{1}{R}\frac{\partial}{\partial R}(R\nu\overline{v_R v_z}) + \frac{\partial}{\partial z}(\nu\overline{v_z^2}) + \nu\frac{\partial \Phi_{\text{tot}}}{\partial z} = 0 \quad , \tag{F.16}$$

and:

$$\frac{1}{R^2}\frac{\partial}{\partial R}(R^2\nu\overline{v_R v_\varphi}) + \frac{\partial}{\partial z}(\nu\overline{v_z v_\varphi}) = 0 \quad , \tag{F.17}$$

respectively.

We can now simplify further our system with some other assumption:

- the principal axes of the velocity dispersion ellipsoid $(\sigma_R^2, \sigma_\varphi^2, \sigma_z^2)$ are aligned with the coordinate axes (R, φ, z). In this case:

$$\sigma_{Rz}^2 = \overline{v_R v_z} - \overline{v_R}\,\overline{v_z} = 0 \implies \overline{v_R v_z} = \overline{v_R}\,\overline{v_z} \quad ; \tag{F.18}$$

- $\sigma_R^2 = \sigma_z^2$, which implies that:

$$\sigma_R^2 = \overline{v_R^2} - \overline{v_R}^2 = \overline{v_z^2} - \overline{v_z}^2 = \sigma_z \quad ; \tag{F.19}$$

- the only non-zero velocity component is the tangential one, meaning that:

$$v_R = v_z = 0. \tag{F.20}$$

With these assumptions, Equations (F.16) and (F.15) become respectively:

$$\text{Eq. (F.16)} \to \frac{\partial}{\partial z}(\nu\sigma_z^2) = -\nu\frac{\partial \Phi_{\text{tot}}}{\partial z} \quad , \tag{F.21}$$

$$\text{Eq. (F.15)} \to \frac{\partial}{\partial R}(\nu\sigma_z^2) + \frac{\nu}{R}(\overline{\sigma_z^2} - \overline{v_\varphi^2}) = \frac{\partial}{\partial R}(\nu\sigma_z^2) - \nu\frac{\Delta_\sigma}{R} = -\nu\frac{\partial \Phi_{\text{tot}}}{\partial R} \quad , \tag{F.22}$$

where we defined $\Delta_\sigma = \overline{v_\varphi^2} - \overline{\sigma_z^2}$.

Bibliography

Algorry, D. G., Navarro, J. F., Abadi, M. G., et al. 2014, *MNRAS*, 437, 3596

Bacon, R. et al. 2010, in Society of Photo-Optical Instrumentation Engineers (SPIE) Conference Series, Vol. 7735, Ground-based and Airborne Instrumentation for Astronomy III, ed. I. S. McLean, S. K. Ramsay, & H. Takami, SPIE, New York, NY, 773508

Bao, M., Chen, Y., Yang, M., et al. 2024, *MNRAS*, 528, 2643

Bao, M., Chen, Y., Zhu, P., et al. 2022, *ApJ*, 926, L13

Bassett, R., Bekki, K., Cortese, L., & Couch, W. 2017, *MNRAS*, 471, 1892

Beom, M., Bizyaev, D., Walterbos, R. A. M., & Chen, Y. 2022, *MNRAS*, 516, 1365

Bertola, F. & Bettoni, D. 1988, *ApJ*, 329, 102

Bertola, F., Buson, L. M., & Zeilinger, W. W. 1992, *ApJ*, 401, L79

Bertola, F., Cinzano, P., Corsini, E. M., et al. 1996, *ApJ*, 458, L67

Bertola, F. & Corsini, E. M. 1999, in IAU Symposium, Vol. 186, Galaxy Interactions at Low and High Redshift, ed. J. E. Barnes & D. B. Sanders, Kluwer Academic Press, Dordrecht, NL, 149

Bettoni, D. 1989, *AJ*, 97, 79

Bettoni, D. & Galletta, G. 1997, *A&AS*, 124, 61

Bettoni, D., Galletta, G., & Oosterloo, T. 1991, *MNRAS*, 248, 544

Bettoni, D., Galletta, G., & Prada, F. 2001, *A&A*, 374, 83

Bevacqua, D., Cappellari, M., & Pellegrini, S. 2022, *MNRAS*, 511, 139

Binney, J. 1981, *MNRAS*, 196, 455

Binney, J. & Tremaine, S. 1987, Galactic Dynamics, Princeton Univ. Press, Princeton, NJ

Binney, J. & Tremaine, S. 2008, Galactic Dynamics: Second Edition, Princeton Univ. Press, Princeton, NJ

Braun, R., Walterbos, R. A. M., & Kennicutt, Robert C., J. 1992, *Nature*, 360, 442

Braun, R., Walterbos, R. A. M., Kennicutt, Robert C., J., & Tacconi, L. J. 1994, *ApJ*, 420, 558

Bruzual, G. & Charlot, S. 2003, *MNRAS*, 344, 1000

Bundy, K., Bershady, M. A., Law, D. R., et al. 2015, *ApJ*, 798, 7

Bureau, M. & Chung, A. 2006, *MNRAS*, 366, 182

Burki, G., Rufener, F., Burnet, M., et al. 1995, *A&AS*, 112, 383

Caon, N., Capaccioli, M., & D'Onofrio, M. 1993, *MNRAS*, 265, 1013

Cappellari, M. 2008, *MNRAS*, 390, 71

Cappellari, M. & Emsellem, E. 2004, *PASP*, 116, 138

Cappellari, M., Emsellem, E., Krajnović, D., et al. 2011, *MNRAS*, 413, 813

Caravita, C., Ciotti, L., & Pellegrini, S. 2021, *MNRAS*, 506, 1480

Ciotti, L. 1991, *A&A*, 249, 99

Ciotti, L. 2021, Introduction to Stellar Dynamics, Cambridge Univ. Press, Cambridge, UK

Ciotti, L. & Bertin, G. 1999, *A&A*, 352, 447

Ciotti, L. & Pellegrini, S. 1996, *MNRAS*, 279, 240

Ciri, R., Bettoni, D., & Galletta, G. 1995, *Nature*, 375, 661

Coccato, L., Morelli, L., Corsini, E. M., et al. 2011, *MNRAS*, 412, L113

Coccato, L., Morelli, L., Pizzella, A., et al. 2013, *A&A*, 549, A3

Comins, N. F., Lovelace, R. V. E., Zeltwanger, T., & Shorey, P. 1997, *ApJ*, 484, L33

Corsini, E. M. 2014, in Astronomical Society of the Pacific Conference Series, Vol. 486, Multi-Spin Galaxies, ed. E. Iodice & E. M. Corsini, Astronomical Society of the Pacific, San Francisco, CA, 51

Corsini, E. M., Morelli, L., Pastorello, N., et al. 2016, *MNRAS*, 457, 1198

Corsini, E. M., Pizzella, A., & Bertola, F. 2002, *A&A*, 382, 488

Corsini, E. M., Pizzella, A., Coccato, L., & Bertola, F. 2003, *A&A*, 408, 873

Corsini, E. M., Pizzella, A., Funes, J. G., Vega Beltran, J. C., & Bertola, F. 1998, *A&A*, 337, 80

Crocker, A. F., Jeong, H., Komugi, S., et al. 2009, *MNRAS*, 393, 1255

Cuomo, V., Corsini, E. M., Aguerri, J. A. L., et al. 2019, *MNRAS*, 488, 4972

Davis, T. A., Alatalo, K., Sarzi, M., et al. 2011, *MNRAS*, 417, 882

De Deo, L., Ciotti, L., & Pellegrini, S. 2024, *MNRAS*, 530, 1796

de Vaucouleurs, G., de Vaucouleurs, A., Corwin, Herold G., J., et al. 1991, Third Reference Catalogue of Bright Galaxies, Springer, New York, NY

D'Onghia, E., Vogelsberger, M., & Hernquist, L. 2013, *ApJ*, 766, 34

Duc, P.-A., Cuillandre, J.-C., Serra, P., et al. 2011, *MNRAS*, 417, 863

Evans, N. W. & Collett, J. L. 1994, *ApJ*, 420, L67

Faber, S. M., Friel, E. D., Burstein, D., & Gaskell, C. M. 1985, *ApJS*, 57, 711

Fabricius, M. H., Saglia, R. P., Fisher, D. B., et al. 2012, *ApJ*, 754, 67

Fisher, D., Illingworth, G., & Franx, M. 1994, *AJ*, 107, 160

Franx, M. & Illingworth, G. D. 1988, *ApJ*, 327, L55

Freeman, K. C. 1970, *ApJ*, 160, 811

Freudling, W., Romaniello, M., Bramich, D. M., et al. 2013, *A&A*, 559, A96

Friedli, D. 1996, *A&A*, 312, 761

Fukugita, M., Shimasaku, K., & Ichikawa, T. 1995, *PASP*, 107, 945

Gadotti, D. A., Sánchez-Blázquez, P., Falcón-Barroso, J., et al. 2019, *MNRAS*, 482, 506

Galletta, G. 1987, *ApJ*, 318, 531

Galletta, G. 1996, in Astronomical Society of the Pacific Conference Series, Vol. 91, IAU Colloq. 157: Barred Galaxies, ed. R. Buta, D. A. Crocker, & B. G. Elmegreen, Astronomical Society of the Pacific, San Francisco, CA, 429

Garcia, A. M. 1993, *A&AS*, 100, 47

García-Burillo, S., Sempere, M. J., & Bettoni, D. 1998, *ApJ*, 502, 235

Gasymov, D. F. O. & Katkov, I. 2022, in The Multifaceted Universe: Theory and Observations - 2022, ed. K. E. Atapin, Sissa Medialab, Trieste, IT, 17

Gerhard, O. E. 1993, *MNRAS*, 265, 213

Goldstein, H., Poole, C., & Safko, J. 2002, Classical Mechanics, Columbia Univ., New York, NY

Gorgas, J., Efstathiou, G., & Aragon Salamanca, A. 1990, *MNRAS*, 245, 217

Haynes, M. P., Jore, K. P., Barrett, E. A., Broeils, A. H., & Murray, B. M. 2000, *AJ*, 120, 703

Hernquist, L. & Barnes, J. E. 1991, *Nature*, 354, 210

Jin, Y., Chen, Y., Shi, Y., et al. 2016, *MNRAS*, 463, 913

Johnston, E. J., Merrifield, M. R., Aragón-Salamanca, A., & Cappellari, M. 2013, *MNRAS*, 428, 1296

Kannappan, S. J. & Fabricant, D. G. 2001, *AJ*, 121, 140

Katkov, I., Chilingarian, I., Sil'chenko, O., Zasov, A., & Afanasiev, V. 2011a, *Balt. Ast.*, 20, 453

Katkov, I., Chilingarian, I., Sil'chenko, O., Zasov, A., & Afanasiev, V. 2011b, *Balt. Ast.*, 20, 453

Katkov, I. Y., Sil'chenko, O. K., & Afanasiev, V. L. 2013, *ApJ*, 769, 105

Khoperskov, S., Zinchenko, I., Avramov, B., et al. 2021, *MNRAS*, 500, 3870

Kormendy, J. 1977, *ApJ*, 218, 333

Krajnović, D., Emsellem, E., Cappellari, M., et al. 2011, *MNRAS*, 414, 2923

Kuijken, K., Fisher, D., & Merrifield, M. R. 1996, *MNRAS*, 283, 543

Ledo, H. R., Sarzi, M., Dotti, M., Khochfar, S., & Morelli, L. 2010, *MNRAS*, 407, 969

Lima Neto, G. B., Gerbal, D., & Márquez, I. 1999, *MNRAS*, 309, 481

Lovelace, R. V. E. & Chou, T. 1996, *ApJ*, 468, L25

Lovelace, R. V. E., Jore, K. P., & Haynes, M. P. 1997, *ApJ*, 475, 83

Maraston, C. 2005, *MNRAS*, 362, 799

Mazzei, P., Marino, A., & Rampazzo, R. 2014a, *ApJ*, 782, 53

Mazzei, P., Marino, A., Rampazzo, R., Galletta, G., & Bettoni, D. 2014b, *Adv. Sp. Res.*, 53, 950

Mazzei, P., Marino, A., Rampazzo, R., et al. 2018, *A&A*, 610, A8

Mazzei, P., Rampazzo, R., Marino, A., et al. 2019, *ApJ*, 885, 165

Mehlert, D., Saglia, R. P., Bender, R., & Wegner, G. 2000, *A&AS*, 141, 449

Mellier, Y. & Mathez, G. 1987, *A&A*, 175, 1

Méndez-Abreu, J., Aguerri, J. A. L., Corsini, E. M., & Simonneau, E. 2008, *A&A*, 478, 353

Moré, J. J., Garbow, B. S., & Hillstrom, K. E. 1980, User guide for MINPACK-1, Technical Report ANL-80-74, Argonne National Laboratory, Argonne, IL

Morelli, L., Halliday, C., Corsini, E. M., et al. 2004, *MNRAS*, 354, 753

Morelli, L., Pizzella, A., Coccato, L., et al. 2017, *A&A*, 600, A76

Morelli, L., Pompei, E., Pizzella, A., et al. 2008, *MNRAS*, 389, 341

Navarro, J. F., Frenk, C. S., & White, S. D. M. 1996, *ApJ*, 462, 563

Negri, A., Ciotti, L., & Pellegrini, S. 2014, *MNRAS*, 439, 823

Osterbrock, D. E., Fulbright, J. P., Martel, A. R., et al. 1996, *PASP*, 108, 277

Pfenniger, D. & Friedli, D. 1991, *A&A*, 252, 75

Pizzella, A., Corsini, E. M., Bertola, F., Funes, J. G., & Beltrán, J. C. V. 1999, in Astronomical Society of the Pacific Conference Series, Vol. 163, Star Formation in Early Type Galaxies, ed. P. Carral & J. Cepa, Astronomical Society of the Pacific, San Francisco, CA, 292

Pizzella, A., Corsini, E. M., Morelli, L., et al. 2003, in The Mass of Galaxies at Low and High Redshift, ed. R. Bender & A. Renzini, Springer, Berlin, 219

Pizzella, A., Corsini, E. M., Vega Beltrán, J. C., & Bertola, F. 2004, *A&A*, 424, 447

Pizzella, A., Morelli, L., Corsini, E. M., et al. 2014, *A&A*, 570, A79

Portaluri, E., Debattista, V. P., Fabricius, M., et al. 2017, *MNRAS*, 467, 1008

Posacki, S., Pellegrini, S., & Ciotti, L. 2013, *MNRAS*, 433, 2259

Prugniel, P. & Simien, F. 1997, *A&A*, 321, 111

Prugniel, P. & Soubiran, C. 2001, *A&A*, 369, 1048

Puerari, I. & Pfenniger, D. 2001, *Ap&SS*, 276, 909

Rix, H.-W., Franx, M., Fisher, D., & Illingworth, G. 1992, *ApJ*, 400, L5

Rubin, V. C. 1994a, *AJ*, 107, 173

Rubin, V. C. 1994b, *AJ*, 108, 456

Rubin, V. C., Graham, J. A., & Kenney, J. D. P. 1992, *ApJ*, 394, L9

Rubino, M., Pizzella, A., Morelli, L., et al. 2021, *A&A*, 654, A30

Sage, L. J. & Galletta, G. 1994, *AJ*, 108, 1633

Salpeter, E. E. 1955, *ApJ*, 121, 161

Sánchez, S. F., Kennicutt, R. C., Gil de Paz, A., et al. 2012, *A&A*, 538, A8

Sandage, A. & Bedke, J. 1994, The Carnegie Atlas of Galaxies, Carnegie Institution of Washington, Washington, DC

Sarzi, M., Falcón-Barroso, J., Davies, R. L., et al. 2006, *MNRAS*, 366, 1151

Sarzi, M., Iodice, E., Coccato, L., et al. 2018, *A&A*, 616, A121

Satoh, C. 1980, *PASJ*, 32, 41

Sellwood, J. A. & Merritt, D. 1994, *ApJ*, 425, 530

Sérsic, J. L. 1963, *Bul. As. Ast. Ar.*, 6, 41

Shlosman, I., Frank, J., & Begelman, M. C. 1989, *Nature*, 338, 45

Sil'chenko, O. K., Moiseev, A. V., & Shulga, A. P. 2010, *AJ*, 140, 1462

Soto, K. T., Lilly, S. J., Bacon, R., Richard, J., & Conseil, S. 2016, *MNRAS*, 458, 3210

Starkenburg, T. K., Sales, L. V., Genel, S., et al. 2019, *ApJ*, 878, 143

Thakar, A. R. & Ryden, B. S. 1996, *ApJ*, 461, 55

Thakar, A. R. & Ryden, B. S. 1998, *ApJ*, 506, 93

Thakar, A. R., Ryden, B. S., Jore, K. P., & Broeils, A. H. 1997, *ApJ*, 479, 702

Thomas, D., Maraston, C., & Bender, R. 2003, *MNRAS*, 339, 897

Tremaine, S. & Yu, Q. 2000, *MNRAS*, 319, 1

Tremonti, C. A., Heckman, T. M., Kauffmann, G., et al. 2004, *ApJ*, 613, 898

van der Marel, R. P. & Franx, M. 1993, *ApJ*, 407, 525

Walterbos, R. A. M., Braun, R., & Kennicutt, R. C., J. 1994, *AJ*, 107, 184

Weilbacher, P. M., Palsa, R., Streicher, O., et al. 2020, *A&A*, 641, A28

Worthey, G., Faber, S. M., Gonzalez, J. J., & Burstein, D. 1994, *ApJS*, 94, 687

Wozniak, H. & Pfenniger, D. 1997, *A&A*, 317, 14

Zeng, G., Wang, L., & Gao, L. 2021, *MNRAS*, 507, 3301